RICE UNIVERSITY

Shot Noise Measurements in Strongly Correlated Materials

by

Panpan Zhou

A Thesis Submitted
in Partial Fulfillment of the
Requirements for the Degree

Doctor of Philosophy

Approved, Thesis Committee:

Douglas Natelson, Chair
Professor of Physics and Astronomy

Pengcheng Dai
Professor of Physics and Astronomy

Jun Lou, Associate Chair
Professor of Material Science and
NanoEnginnering

Houston, Texas

November, 2019

ABSTRACT

Shot Noise Measurements in Strongly Correlated Materials

by

Panpan Zhou

In conventional metals where the interaction between electrons is weak, the low energy excitations can be well explained by Landau Fermi liquid theory. However, in many metallic materials with bulk d or f-electrons, such as transition metal oxides, conventional theories fail to effectively describe the electronic or spin properties due to the presence of strong electron-electron interactions. A better understanding of electronic behavior in strongly correlated systems has been a great challenge in modern physics. In this dissertation, I mainly focused on the studying of quasiparticle's effective charge in strongly correlated material by probing the shot noise—a current fluctuation that originates from the discrete nature of charge carriers. We firstly explored methods for fabricating tunnel junctions and found that hexagonal boron nitride (hBN) is a very good candidate for a tunneling barrier. The tunneling device made by Au/hBN/Au has well-behaved shot noise properties that match with single-particle tunneling predictions quantitatively. Shot noise is also studied in high-quality LSCO/LCO/LSCO tunnel structures grown by the molecular beam epitaxy (MBE) technique at various doping levels from underdoped to nearly optimum doped. In those devices, the shot noise is found to be larger than single-electron tunneling prediction deep into the pseudogap region of temperature and bias, indicating pairing might exist in the pseudogap phase.

Acknowledgment

Foremost, I would like to express my sincere gratitude to my advisor Prof. Douglas Natelson for the continuous support of my Ph.D study and research, for his patience, motivation, enthusiasm, and immense knowledge. His guidance helped me in all the time of research and writing of this thesis. I could not imagine having a better advisor and mentor for my Ph.D study.

Besides my advisor, I would like to thank the rest of my thesis committee: Prof. Pengcheng Dai, Prof. Jun Lou, for their encouragement, insightful comments, and hard questions. Many thanks to my mentors at Rice, Prof. Frank Geurts and Prof. Ruirui Du for providing me great guidance in academic and in life.

I also want to express my gratitude to Prof. Yujie Xiong at University of Science and Technology of China, Prof. Hobun Chan at Hong Kong University of Science and Technology. They provided me great support and guidance in beginning my scientific research career.

None of my research could be done without the support from our collaborators. Here, I want to express my thanks to Prof. Kenji Watanabe, Prof. Takashi Taniguchi from NIMS for supplying us the high quality 2-D materials, to Prof. Ivan Bozǒvić, Dr. Anthony Bollinger, Dr. Xi He, Prof. Yimei Zhu, Dr. Myung-Geun Han, from Brookhaven National Lab for their help in fabricating/imaging the dedicate copper-oxide devices, and to Prof. Ilya Sochnikov from University of Connecticut for helping with some transport measurements.

My sincere thanks also goes to Dr. Joe Masters, for offering me the summer internship opportunities in Quantlab LLC and leading me working on diverse exciting projects.

I thank my fellow labmates in Natelson's Group: Dr. Heng Ji, Dr. Will Hardy, Dr. Pavlo Zolotavin, Dr. Ruoyu Chen, Dr. Loah Stevens, Xuanhan Zhao, Liyang Chen, Yue Liu and Chenyuan Li for the stimulating discussions, for the sleepless nights we were working together debugging experimental instruments, and for all the fun we have had in the last six years. Also I thank all my friends in Rice University, Hong Kong University of Science and Technology and University of Science and Technology in China. I cannot go this far without their support and accompany.

Last but not the least, I would like to thank my family: my parents Yijiao Zhou and Yifang Zhou, for giving birth to me at the first place and supporting me spiritually throughout my life.

Panpan Zhou, Oct, 2019

*****

Contents

Illustrations

Tables

Chapter 1

Introduction

The Fermi Liquid theory was developed by Landau to described the properties of liquid ^{3}He.[21] It can be used to explain the normal state of most metals at low temperatures. In the Fermi Liquid theory, the excited states of interacting systems are considered as having a one-to-one correspondence with excited states of non-interacting systems. As the excited states are not true eigenstates of the interacting system's Hamiltonian, they are called "quasiparticles" or "quasiexcitations". In normal metals, the quasiparticles are usually electron-like, with effective charge $-e$ and spin $\frac{1}{2}$. Those quasiparticles have long lifetime τ that satisfies $\frac{\hbar}{\tau} \ll \epsilon_p$, where ϵ_p is the quasiparticle energy relative to the Fermi energy. Also the quasiparticles have long inelastic mean free paths and they can travel long distances between scattering events. At low temperatures, the normal metal resistivity is often found to vary as $\rho(T) = \rho_0 + \beta T^2$. Such T^2 dependence mainly comes from electron-electron interactions and has become an empirical criterion for Fermi Liquid behavior.

In strongly correlated materials, the electrons are often more localized. The electron-electron interaction is strong enough that Landau liquid theory fails in explaining its properties. Such non-Fermi-liquid behaviors include heat capacity following $\frac{C}{T} \sim -logT$ [22], resistivity not following T^2 [23], Mott-insulator-transition (MIT) [24], colossal magnetoresistance [25], etc. The non-Fermi liquid metals are also known as "bad metals" or "strange metals". In those materials, the electron-like quasiparticles can no longer be good descriptions for low energy excited states. Understanding strongly correlated materials is one of the major problems in condensed matter physics.

1.1 Strongly correlated material

The strong electron-electron interaction leads to many dramatic properties and transitions between distinct phases with different electronic or magnetic orders, such as Mott-insulator transitions, high-temperature superconductivity, colossal magnetoresistance, large thermoelectric power, heavy Fermions, etc.

1.1.1 Mott insulator

Sommerfield Theory is the first theory to explain the electron behavior from a quantum point of view [26]. In this theory, the electrons are treated as free; the underlying ion field and the electron-electron interaction are not included. The band theory added the ion field into account and successfully explained metal and insulators. In this picture, a metal corresponds to a partially filled band and insulator corresponds to a fully filled band.

However, later it was found that many transition metal oxides like NiO, MnO, FeO, CoO [27, 28], VO_2 [29], which should be metallic according to band theory, turn out to be an insulators. Such insulators that result from electron-electron interaction are called "Mott Insulators" and the transition between metallic phase to insulator phase is the Mott insulator transition.

There have been many theoretical works trying to understand the Mott insulator. But once the effects of electron-electron interactions are included, the problem becomes a very complex many-body problem and very nasty to solve. Within them, the Hubbard model [30] has achieved some success in explaining Mott insulators; it simplifies the problem by maintaining the essential physics while ignoring the details of the system. The Hubbard model for Mott insulator is:

$$H_H = H_t + H_u - \mu N \tag{1.1}$$

$$H_t = -t \sum \left(c^\dagger_{i\sigma} c_{j\sigma} + h.c. \right) \tag{1.2}$$

$$H_u = U \sum \left(n_{i\uparrow} - \frac{1}{2} \right) \left(n_{i\downarrow} - \frac{1}{2} \right) \tag{1.3}$$

where $N = \sum n_{i\sigma}$, $n_{i\sigma} = c^\dagger_{i\sigma} c_{i\sigma}$, $c^\dagger_{i\sigma}$ is the electron creation operator. H_t is for the nearest-neighbor hopping Hamiltonian, and H_u is for the onsite Coulomb repulsion in the short range only.

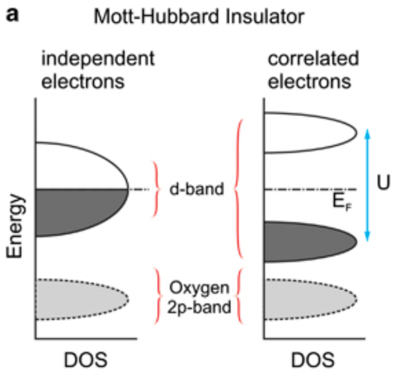

Figure 1.1 : Hubbard model for Mott-insulator, Adapted from a tutorial [1] on Mott insulator.

As Figure 1.1 shows, as the interaction term U turns on, the p band remains unchanged, but the d band splits into two sub-bands and opens up an energy gap.

This explains the Mott insulator behavior.

1.1.2 High-temperature Superconductor

The high-temperature superconductivity, upon its first discovery in 1986 [31], has been one of the most intensively studied fields due to its great potential technological applications. On the experimental side, researchers have great enthusiasm in the race of improving the critical temperature as well as probing the fundamental mechanism of high-temperature superconductivity. On the theoretical side, researchers are pursuing new models other than BCS model (Bardeen, Cooper, and Schrieffer, 1957) [32] to explain the behavior of the new superconductors.

The BCS theory and its extensions provide an elegant explanation to the properties of conventional superconductors. The success is based on the following points:

- The normal state can be accurately described by Fermi liquid theory. There are well-defined quasiparticles to form collective pairs.
- The phonons involved are in coherent collective modes that allow phonon-assisted pairing identification.
- The phonon energies are small compared to the Fermi energy. The weak retarded attraction induced by the phonons overcomes the strong electron-electron Coulomb repulsion.

However, in high-temperature superconductors, all those points are not valid anymore: there may not be well-defined quasiparticles in the normal state at $T > T_c$; other collective modes that could be possible candidate replacements for phonons (e.g. magnons) in the BCS case, are only coherent in the undoped parent state; the dynamic range is too little for retardation to form attraction.

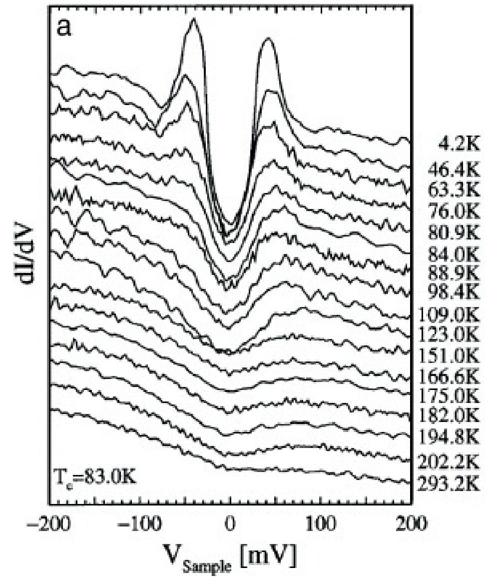

Figure 1.2 : Scan tunneling spectroscopy measurements of $Bi_2Sr_2CaCu_2O_{8+\delta}$. The transition temperature $T_c = 83$ K. The gap does not disappear until the temperature is much higher than T_c. The gap here at temperatures above T_c is referred as the pesudogap. Adapted from ref [2].

In conventional superconductors, there is an energy gap between the paired superconducting state and unpaired normal state. This energy gap is known as the superconducting gap, and will disappear at above the transition temperature T_c. For high-temperature superconductors, things become much more complicated. There exists a suppression density of states around E_F well above T_c at a wide region of compositions and temperatures, see Figure 1.2. This suppression density of state is called the pseudogap, as it is not directly related to superconducting transition. The corresponding phase that holds the pseudogap is called the pseudogap phase. The origin of this mystery phase and its relation to the superconducting phase are believed to be the key for understanding the mechanism of high-temperature superconductivity and this has become one of the hottest topics in condensed matter physics.

1.1.3 Colossal magnetoresistance

Colossal magnetoresistance is a property of some materials, such as manganese-based perovskite oxides $La_{1-x}Ca_xMnO_3$ [3], that have a dramatic change of their electrical resistance in the presence of an external magnetic field. These materials have the potential for applications in information storage, spintronics, drug delivery, spin cooling, etc.

The CMR effect originates from a unique type of metal-insulator transition in the low temperature limit near the Curie temperature and is driven by magnetic fields on the order of a few Tesla. In contrast to traditional ferromagnetic materials such as Fe, Co, and Ni where the spin is itinerant relatively weakly coupled to the lattice, in CMR materials, the charge, spin, and lattices are strongly coupled together, leading to the rise of a rich variety of physical phenomena.

The complexity of the mixed phasing is shown for $La_{1-x}Ca_xMnO_3$ in Figure 1.3. The drop in resistivity with decreasing temperature and the peak in MR originate from the ferromagnetic transition and there is a prominent metal/insulator phase transition across the Curie temperature T_C. The interpretation and understanding of the mechanism of such a complex system are quite important for progress in the field of correlated electrons.

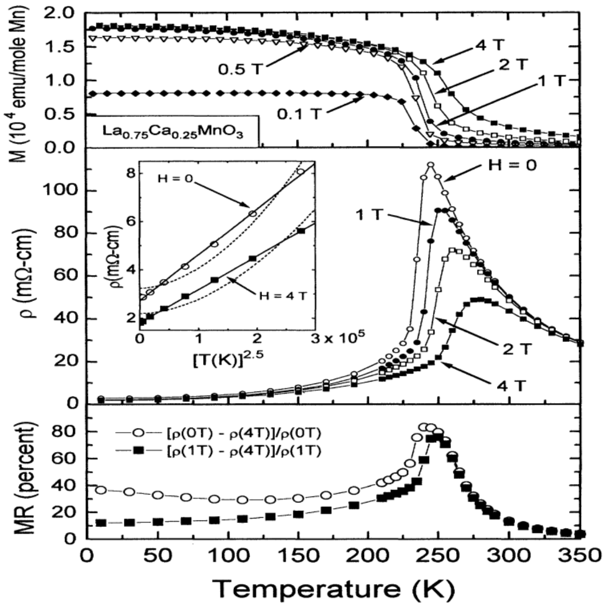

Figure 1.3 : The magnetization, resistivity, and magnetoresistance of $La_{0.75}Ca_{0.25}MnO_3$ as a function of temperature at various field. Figure is adapted from ref [3].

1.1.4 Heavy Fermions

The physics of heavy fermions was first discovered by Andres *et al* (1975) in the study of electronic excitations in $CeAl_3$ alloys [33], where the low-temperature specific heat's linear term is up to 1000 times larger than that of a normal material like copper. The name "heavy fermion" comes from the fact that the electronic excitations in this type of material have an effective mass much larger than conventional excitation's effective mass. The heavy fermion materials have become the focus of intense interest because the properties of such materials could be controlled through quantum phase transitions by pressure, magnetic field, or chemical doping [34]. The "quantum critical point" (QPC) separates the heavy fermion's ground state from antiferromagnetic (AFM) state, superconductivity state, and other novel states. Heavy fermion materials link the magnetic and electric degrees of freedom and provide an important playground for the development of our understanding of the interaction between magnetic and electronic quantum fluctuations.

One remarkable prospect of heavy-fermion materials is the "non-Fermi liquid behavior", which is observed over a wide range of temperatures and applied magnetic field above the QCP. For example in the phase diagram of $YbRh_2Si_2$ [4] shown in Figure 1.4, there are transitions between Fermi liquid and non-Fermi liquid. In the dark blue regions on both sides, the resistivity shows T^2 dependence that indicates Fermi-liquid behavior. In the middle orange region, though the resistivity follows a linear dependence versus the temperature. The tunable transition between Fermi-liquid and non-Fermi liquid allows a direct comparison of the well-defined Landau quasiparticles and ill-defined quasiparticles in strongly correlated systems.

1.2 Tunnel junction and shot noise

1.2.1 Quantum tunneling effect

The electron tunneling phenomenon is related to many important research fields, such as atomic scale imaging, tunnel junctions, atomic electronics, etc. We first introduce the tunneling effect by a simple 1D potential barrier example:

Consider a potential barrier with constant V_0 between $(-a, a)$ and zero outside this

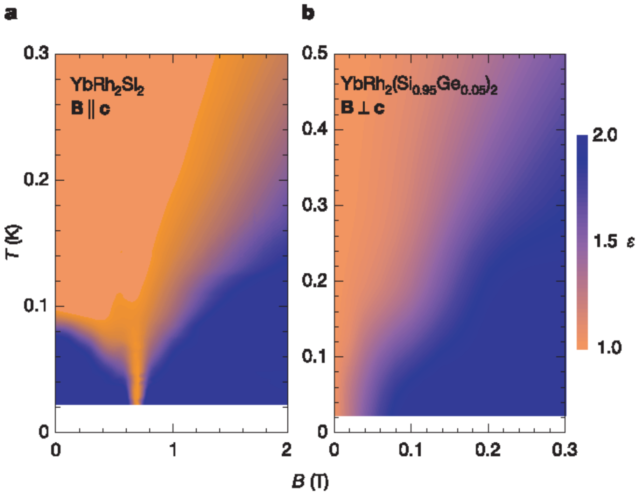

Figure 1.4 : The temperature-field phase diagram of $YbRh_2Si_2$ and $YbRh_2(Si_{0.95}Ge_{0.05})_2$ with field direction parallel to the c-axis and perpendicular to the a-axis correspondingly. Figure is adapted from ref [4].

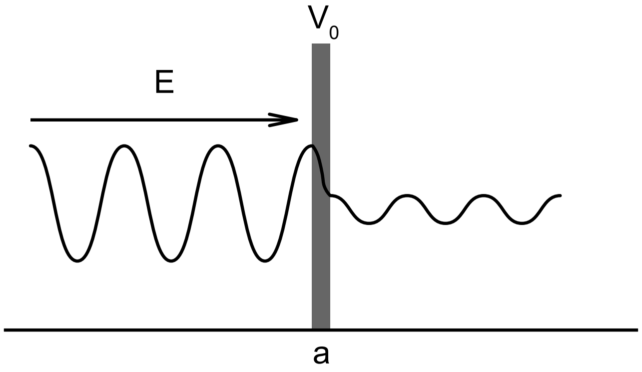

Figure 1.5 : Schematic figure of quantum tunneling effect

region, as Figure 1.5 shows. A particle with energy $E < V_0$ starts on one side of the barrier and travels in the direction toward the other side of the barrier. Classically, there is 0 possibility that the particle could travel through the barrier. However, due to the wave-particle duality, we can treat the particle as a wave, and then we can define the quantity τ as the transmission probability of the particle going through the barrier. The Schrodinger equation gives an analytical way to solve the problem:

$$H\Psi = E\Psi \tag{1.4}$$

$$-\frac{\hbar^2}{2m}\frac{d^2\Psi}{dx^2} + V(x)\Psi = E\Psi \tag{1.5}$$

The solution to this Schrodinger equation given the boundary conditions gives transmission coefficient τ as:

$$\tau \sim e^{-2a\sqrt{\frac{2m}{\hbar^2}(V_0-E)}} \tag{1.6}$$

The transmission coefficient τ decays exponentially with the barrier thickness a and $\sqrt{\frac{2m}{\hbar^2}(V_0 - E)}$. In the case when τ is extremely small and each tunneling event is independent, the tunneling process obeys Poissonian statistics.

1.2.2 Tunnel junction

The tunnel junction is an electrical barrier, such as a thin insulating layer or electric potential, between two electrically conducting materials. Due to the quantum tunneling effect, the electrons have a small probability of passing through the barrier, see Figure 1.6. Based on the materials, there are several different types of tunnel junctions: (a) normal metal tunnel junctions, such as tunneling between Au to Au through hexagonal boron nitride; (b) magnetic tunnel junctions (MTJ), where electrons tunnel between two ferromagnetic magnetic materials; (c) ferroelectric tunnel junctions (FTJ), where electrons tunnel between two metal electrodes through a thin ferroelectric layer. The spontaneous polarization of the ferroelectric layer can be switched by an applied electric field, and the electrical resistance of the FTJ depends on the orientation of the electric polarization direction; (d) Superconducting tunnel junction (STJ), which is also known as superconductor-insulator-superconductor (SIS) tunnel junction, where electrons tunnel between two superconductors separated by a very thin layer of insulating material. If the Cooper pairs phase is coherent in two superconductors, the tunneling properties can be described by the Josephson effect, and in this case, it becomes a Josephson junction.

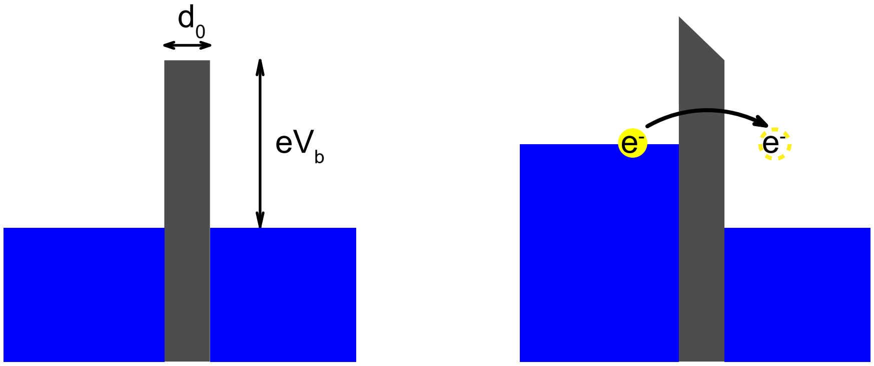

Figure 1.6 : Schematic figure of electron tunneling effect in a tunnel junction

The tunnel junctions have many applications, ranging from fundamental research to industrial products. Normal metal tunnel junctions can be used as a basic thermometer in extremely low temperatures due to their noise behavior [10]. MTJs have potential use as non-volatile memory storage cells in magnetic random access memory and as advanced read sensors in hard disk drives [35]. FTJs can also be used as information storage units due to their controllable on-off states [36]. Josephson junctions have been used to build electronic circuits, especially digital logic circuitry

[37]. Many researchers are working on building ultrafast quantum computers using Josephson logic [38]. Josephson junctions are also elemental components of SQUIDs, superconducting quantum interference devices. These devices are highly sensitive and are very useful in constructing sensitive magnetometers and voltmeters.

During the decades of development, many methods have been used to fabricate the tunnel junctions. Traditionally, the intrinsic oxides, such as AlO_x, FeO_x and SiO_2 have been used as the tunneling barrier. However, the quality of the barrier formed by the oxidization process can be hard to control—it may suffer from pinholes, inhomogenities and defects. Researchers have tried more controllable ways to grow the barrier and the atomic-layer deposition method [39] and the molecular beam epitaxy method [40] have successfully achieved high-quality tunnel junctions. With the development of 2D materials, many people tried to fabricate tunnel junctions from some insulating 2D materials, such as hexagonal boron nitride (hBN) [41] and molybdenum disulfide (MoS_2) [42]. More recently, Robert Dynes' group at UCSD explored the possibility of in-plane tunnel junction using focused-ion beam (FIB) technique [43]. The FIB disordered the crystal structure of YBCO film and created a very narrow barrier. Josephson effect is observed in those FIB-based high-temperature superconductor tunnel junctions.

1.2.3 Shot noise in tunneling limit

Because of the wave-particle duality, the electrical current, which is formed by moving electrons, will have fluctuations. Current fluctuations due to the discrete nature of the electronic charge are known as "shot noise". This type of noise was first observed in vacuum tubes back to the 1920's [44]. In a vacuum tube, electrons are emitted from the negative cathode to the positive anode randomly and independently. Such a Poisson process has the property that the mean squared fluctuation of the emission event count is equal to the mean event count. The corresponding current noise spectral density has the simple equation $S = 2e\bar{I}$. At finite temperature, the Fermi distribution of the electron energy modified the relation to $S = 2e\bar{I}coth(\frac{eV}{2k_BT})$ at driving bias V and temperature T. At zero bias, the noise spectral density S_I approaches $4k_BT/R$. This can be used to measure the temperature in the cryogenic environment where traditional thermometry is challenging.

In some systems where the granularity of the current is not the elementary charge, the shot noise can give information above the effective charge e^* by $S = 2e^*\bar{I}$. A first example is the shot noise between a normal metal and a superconductor [13]. In N-S junctions under the right condition, transport current is carried by pairs, so that $e^* = 2e$ and the shot noise spectral intensity will be doubled. Another example is shot noise in the fractional quantum Hall effect. Robert Laughlin's theory predicts that the quasiparticles tunneling from one edge of a Hall bar to the other edge carry a fractional electron charge $e^* = \frac{e}{2p+1}$, where the integer p is determined by the filling factor $\frac{p}{2p+1}$ of the lowest Landau level. Such fractionally charged quasiparticles have been confirmed experimentally in various fractional quantum Hall systems [12, 45]. By studying the shot noise in strongly correlated materials, we can know how much effective charge the quasiparticles carry and have a better understanding of the quasiparticles.

1.3 Thesis structure

The main target of this research is to study the quasiparticle's electronic properties in strongly correlated materials. Specifically, this dissertation is focused on the measurement of shot noise in $La_{2-x}Sr_xCuO_4$ tunnel junctions to study the effective charge in cuprates.

Chapter 2 gives an introduction to the background knowledge for mesoscopic transport physics. At scales where quantum mechanics play an important role, many interesting phenomena show up. Shot noise is one of the phenomena that arises from the quantum tunneling process. In Chapter 3 we introduce the high-temperature superconductivity and the cuprate superconductors. The conventional superconductors and unconventional superconductors are briefly reviewed. The origination of superconductivity and the mysterious pseudogap phase are also discussed in the high-temperature superconductors. In Chapter 4 we describe the experimental system used in this research, including the cryogenic system, sample fabrication/characterization systems, conductance measurement system and shot noise measurement systems. This provides a general idea about the tools for modern scientific experiments.

In chapter 5, hBN-based tunnel junction fabrication and shot noise detection is presented. From the result, it is confirmed that our noise measurement setup can reach a quantitative agreement with theoretical predictions for conventional tunnel junctions. Also, this points to a general method for making tunnel junctions based on strongly correlated material, which is meaningful for studying the quasiparticle properties in those materials.

Chapters 6 and 7 are the main text focusing on the conductance and shot noise measurement on LSCO/LCO/LSCO tunnel junctions. Chapter 6 talks about the sample fabrication, characterization and simple transport behavior of the cuprate tunnel junctions. It discusses the difference between those tunnel junctions and conventional Josephson junctions. Chapter 7 is focused on the shot noise measurement in the cuprate tunnel junctions, where we discovered some interesting quasiparticle behaviors in the pseudogap phase at temperature above critical temperature T_c and bias larger than the superconducting gap Δ.

Chapter 2

Mesoscopic transport physics

Electron transport properties are of major interests to condensed matter physics as tools to probe underlying physics. The transport measurement is crucial to the understanding of the electronic structure of materials and the interaction among carriers and between carriers and the lattice. There has been much theoretical progress and a wide variety of scientific instruments developed through the studying of electron transport. At the nanoscale, quantum effects lead to many emergent phenomena. In this dissertation, most of the content is focused on the electron transport properties in strongly correlated materials at the nanoscale. As the first step toward understanding the context, in this chapter, we will discuss the physics in electron transport in our experiments.

2.1 Introduction to mesoscopic electron transport

Transport is the phenomenon of flowing current in response to external fields. With the assumption that transport occurs near equilibrium, the currents and fields are linearly related and the coefficients represent the characteristics of the material and state.

“There's plenty of room at the bottom”, as physicist Richard Feynman's speech

[46] pointed out, there is plenty of physics to discover when we enter the quantum regime. In the mesoscopic scale, the device's dimension is comparable to the wavelength of the carriers and the variation of the density-of-states can produce dramatic changes in the transport properties compared to bulk materials. With the quantum confinement, the energy levels available for electrons are different from the traditional continuum of energy levels or bands. The conduction at the mesoscopic scale can be affected by small number of states and single-electron charging effects can be significant. Nanoscience offers a special opportunity to design modern materials from the bottom up via the assembly of nanoscale building blocks. The understanding of the mesoscopic transport properties of materials is the milestone in the design of new functional materials.

2.2 Mesoscopic conductance

The conductance of a sample with a size larger than the coherence length of electrons l_ϕ has been well studied. When the sample length scale is smaller than l_ϕ, the whole conductor has to be considered a single quantum system. To calculate the conductance, in 1957 Rolf Landauer suggested considering the leads as black body sources that incoherently emit carriers toward the coherent domain and perfectly absorb carriers which are elastically scattered by it [47]. The sample conductance is proportional to the sum of transmission probabilities τ_n, through all possible channels at the Fermi surface:

$$G = 2e^2/h \sum_n \tau_n \tag{2.1}$$

This relation is in good agreement with many experiments where the electron-

electron interaction can be neglected. It successfully explained many mesoscopic transport phenomena such as Universal Conductance Fluctuation (UCF), Aharonov-Bohm conductance oscillations, conductance quantization in Quantum Point Contacts (QPC) and Quantum Hall systems. The effects of strong interactions between electrons in strongly correlated materials on these phenomena deserve further exploration.

2.2.1 Universal conductance fluctuations

Universal conductance fluctuations (UCF) are signatures of phase-coherent transport in mesoscopic physics [48]. In the semiclassical picture, electrons travel along certain trajectories like particles but also carry their phase information like waves. For materials with inhomogeneous scattering sites, the electrons will experience several scattering events along their travel trajectories. For an electron propagation, there is a complex amplitude $A_k e^{i\phi_k}$ corresponding to each trajectory. In quantum mechanics, the total probability of various paths is not the simple summation of each probability. Instead, we have to take the phase of each component into consideration. Given each different path's amplitude, $A_k e^{i\phi_k}$, the total probability is $|\sum_k A_k e^{i\phi_k}|^2$, this is where the quantum interference effects take place.

The phase of each trajectory is affected by the position of impurity and disorder, so different samples will exhibit different conductance patterns. But for a given sample, the phase of each trajectory is almost fixed as long as the scattering sites do not change, which results in a speckle pattern in the conduction, and the typical scale of the speckle in a fully coherent system is on the order of the conductance quantum $G_0 = 2e^2/h$. The magnetic field can alter the relative phase of different trajectories.

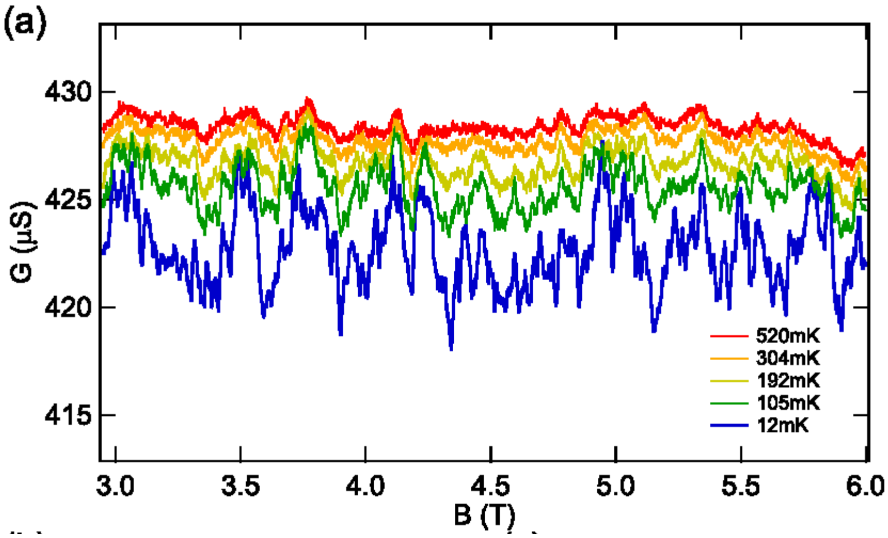

Figure 2.1 : Example of UCF in electrolyte-gated $SrTiO_3$ nanostructures. The reproducible universal conductance fluctuations in G maintain shape but decrease in amplitude with increasing temperature. Adapted from ref [5].

Thus the sample conductance has sample-specific, random-looking but reproducible field dependence, see Figure 2.1.

2.2.2 Aharonov-Bohm conductance oscillation

In a 1959 paper [49], David Bohm and his graduate student Yakir Aharonov predicted a quantum mechanical effect that arises when a particle passes through regions where the potential ϕ and $\mathbf{A}$ are nonzero, but the physical fields $\mathbf{E}$ and $\mathbf{B}$ are zero.

An experimental geometry close to Aharonov and Bohm's suggestion is shown in Figure 2.2. The incident beam has two trajectories, one passes above the cylinder and one passes below the cylinder. In the region outside the cylinder radius $r > a$, $\mathbf{A}$

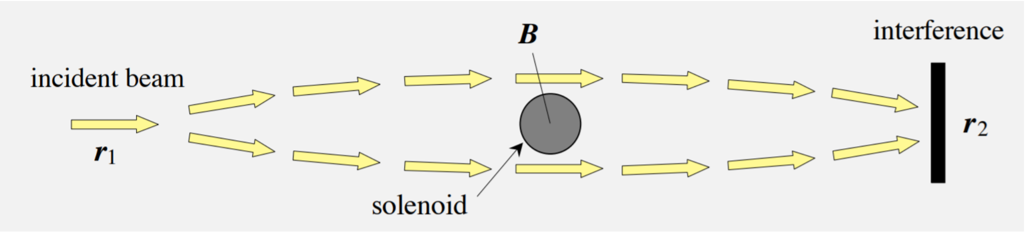

Figure 2.2 : An experimental geometry suggested by Aharonov and Bohm. The **B** field (out of the page) is fully contained within a cylinder, whereas **A** is nonzero outside the cylinder. Adapted from a tutorial on A-B effect [6].

is given by:

$$\boldsymbol{A} = \frac{\Phi}{2\pi r}\hat{\phi} \tag{2.2}$$

where Φ is the magnetic flux in the cylinder and $\hat{\phi}$ is the direction vector of the field **B**. The presence of **A** results in a phase difference β for waves that follows the two trajectories:

$$\beta = (q/\hbar c)\{\int_{r_1}^{r_2} d\boldsymbol{r}\cdot\boldsymbol{A}_{lower} - \int_{r_1}^{r_2} d\boldsymbol{r}\cdot\boldsymbol{A}_{upper}\} = (q/\hbar c)\oint d\boldsymbol{r}\cdot\boldsymbol{A} \tag{2.3}$$

Integration over the closed circuit yields:

$$\beta = (q/\hbar c)\Phi = 2\pi\Phi/\Phi_L \tag{2.4}$$

The phase difference is proportional to the magnetic flux Φ. Thus sweeping the field will cause oscillation to the interference.

This phenomenon is most directly illustrated by the occurrence of periodic oscillations in the conductance of ring-shaped devices, measured as a function of magnetic fields, see Figure 2.3. This effect has been extensively investigated in rings made with

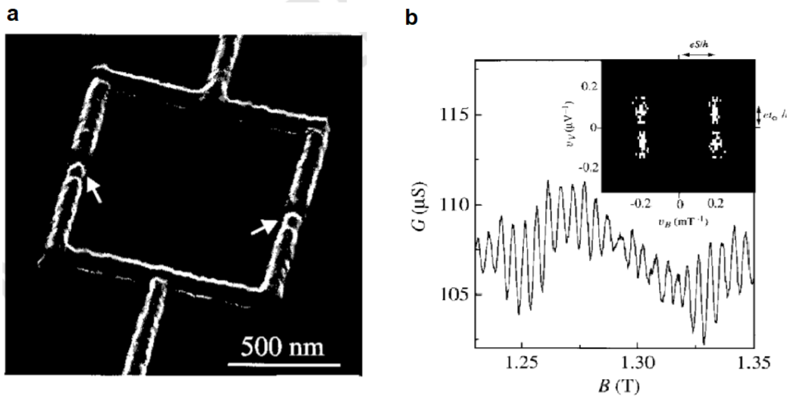

Figure 2.3 : Aharonov-Bohm (AB) ring and the conductance oscillation as a function of magnetic field. **a**, Scanning electron microscope image of the Aharonov-Bohm ring which is interupted by two small tunnel junctions. **b**, Conductance G versus magnetic field B. Adapted from ref [7].

metallic films or with semiconducting heterostructures, and its study contributes significantly to the understanding of mesoscopic physics.

2.2.3 Conductance Quantization in Quantum Point Contacts

This history of ballistic transport goes back to 1965 when researchers studied point contact made by single-crystal metal [50]. However, as the Fermi wavelength (λ_F ~0.5 nm) in the metal is much smaller than the gap size, quantum mechanics does not play an important role in the single-crystal system. With the fabrication of a two-dimensional electron system (2DES) in a GaAs-AlGaAs heterojunction [51], the Fermi wavelength in 2DES is found to be much longer than that in conventional metal. This enables the study of constrictions comparable to the wavelength and such constriction is called a quantum point contact (QPC).

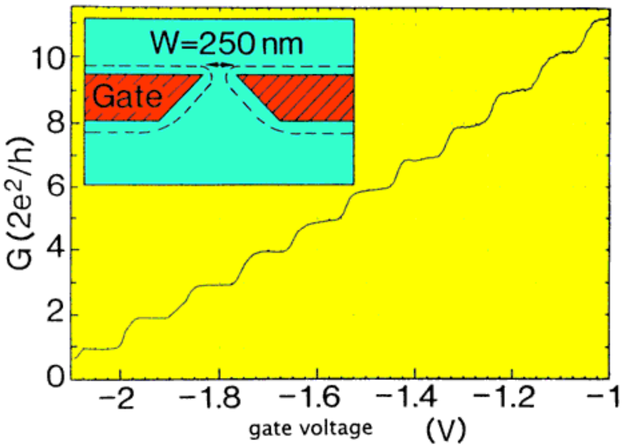

Figure 2.4 : Quantization of the conductance of a quantum point contact. Adapted from ref [8].

As shown in Figure 2.4, as the gate voltage varies, the conductance exhibits a sequence of steps, and the steps are near integer multiple of $2e^2/h = 1/13\ k\Omega$. The Landauer formula gives a semi-classical explanation of the conductance quantization—in Landauer's view, the constriction with width W acts as an electron waveguide, through which a smaller integer number $N \approx 2W/\lambda_F$ of transverse modes can propagate at the Fermi level. For a voltage difference V between two reservoirs, each mode carries the same current $I_n = Ve^2/h$. Summing over all the modes and accounting for the spin-up, spin-down degeneracy, one obtain the total conductance $G = N \cdot 2e^2/h$.

2.2.4 Conductance Quantization in Quantum Hall systems

The Quantum Hall Effect (QHE) was discovered by von Klitzing in 1980 [9], for which he was awarded the Nobel prize in 1985. In the QHE, the Hall resistance R_H measured on a 2DES at low temperatures and high magnetic fields applied perpendicularly to the 2DES, shows stepwise plateau values (Figure 2.5**a**). These plateau values can be well described by $R_H = h/ie^2$, where i is an integer value. Thus, the conductance takes the quantized form $G_H = ie^2/h$.

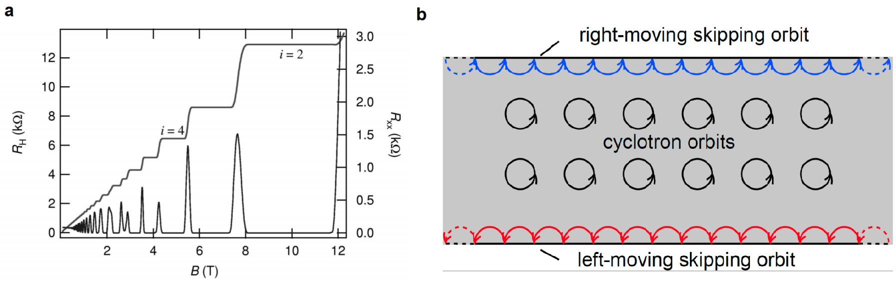

Figure 2.5 : Quantun Hall effect. **a**, Hall resistance R_H and of the longitudinal resistance R_{xx} for a GaAs/AlGaAs heterostructure at 0.1 K. **b**, Edge state in Quantum Hall system formed by cyclotrons. Adapted from ref [9].

The quantization of Hall conductance can be well explained by the Gauge transformation with the consideration of magnetic potential $\boldsymbol{A}$. The magnetic field split the energy levels into quantized Landau levels with each Landau level corresponding to an edge state. This can be more directly visualized in Laughlin's picture—with the external field, the electron's trajectory is a circular orbit with radius given by the cyclotron radius, see Figure 2.5**b**. The electrons at lower edge and upper edge move in opposite directions and these strange states obtained at the edges are often referred to as chiral edge states. Each of the edge states forms a conductance channel, thus the total conductance exhibits the quantized feature.

2.3 Shot noise in mesocopic system

The term “shot effect” (schroteffekt) was invented by Walter Schottky in 1918 during the study of electrical noise in a vacuum tube [44]. Shot noise originates from the discrete nature of charge carriers. Shot noise also exists in photon counting statistics in optical devices, where shot noise is associated with the particle nature of light. The fundamental physics determines that the electron transmission or photon emission process is random and approximately independent. Such processes can be modeled as a Poisson process with the count value in certain time interval fluctuating around its average.

2.3.1 Current fluctuations

According to the Third Law of thermodynamics, it is not possible to reach absolute zero temperature. This law determines that even under constant operation conditions if one closely observes the current signal $I(t)$ through a conductor, there will always be fluctuations in time. The noise is defined as the deviation to the average value, i.e. $\Delta I(t) \equiv I(t) - \bar{I}$. The fluctuation can be characterized by the power spectrum density $S(\omega)$ at frequency ω, which is defined as the Fourier transform of the autocorrelation function:

$$S(\omega) = 2\int_{-\infty}^{\infty} dte^{i\omega t}\langle \Delta I(t+t_0)\Delta I(t_0)\rangle \tag{2.5}$$

where $\langle \ldots \rangle$ denotes an ensemble average.

The thermal fluctuation of the charge carriers at equilibrium gives thermal or Johnson-Nyquist noise. The Johnson-Nyquist noise is white noise ($S(\omega)$ independent from ω) and its power spectral density is proportional to the temperature T and conductance G,

$$S(\omega) = 4k_BTG \tag{2.6}$$

At very high frequencies, as the zero-point fluctuation should be taken into consideration, equation 2.6 no longer works. For arbitrary frequency, the spectrum is given by [52]:

$$S(\omega) = 4G\left(\frac{1}{2}\hbar\omega + \frac{\hbar\omega}{exp(\hbar\omega/k_BT) - 1}\right) \tag{2.7}$$

There is an extrinsic type of noise named 1/f noise where the power spectral density takes the form:

$$S(\omega) \propto \frac{1}{\omega^\alpha}$$

where $0 < \alpha < 2$, with exponent α usually close to 1. The principal source of 1/f noise in electronic devices is the slow fluctuations of properties of the condensed matter materials. Such fluctuating properties include the configuration of defects, occupancies of traps, domain structure, etc. The typical frequency range over which the 1/f noise is active is within kHz range. At relatively high frequencies, the 1/f effect is weak, due to the noise power density decaying in such a frequency range.

Another type of current fluctuations at non-equilibrium is shot noise. Due to the discreteness of the charge carriers, the current is not a continuous flow, but a discrete sequence of charge pulses in time. Shot noise also has a white spectrum and is linearly proportional to the magnitude of the current. The shot noise S_I consists of two terms [53], $S_I = S_{I,part} + S_{I,thermal}$, the first term $S_{I,part}$ is due to partition and the second term $S_{I,thermal}$ is from the thermal noise of the reservoirs. The two noise contributions are:

$$S_{I,part} = 2G_0 \int \sum_n \tau_n(1-\tau_n)\left[f_l - f_r\right] d\epsilon \tag{2.8}$$

$$= 2G_0 coth(\nu) \sum_n \tau_n(1-\tau_n) \times eV \tag{2.9}$$

$$S_{I,thermal} = 2G_0 \int \sum_n \tau_n^2 \left[f_l(1-f_l) + f_r(1-f_r)\right] d\epsilon \tag{2.10}$$

$$= 2G_0 \sum_n \tau_n^2 \times 2k_BT \tag{2.11}$$

where $\nu = \frac{eV}{2k_BT}$ is the normalized bias and τ_n is the transmission probability and f is the Fermi distribution of the left and right reservoirs. The $coth(\cdot)$ term comes from the difference of Fermi distribution at two reservoirs. We define the excess noise $\Delta S_I(I) = S_I(I) - S_I(0)$, which is proportional to the Poissionan noise: $\Delta S_I = F \times S_{I,Poisson}$ with:

$$S_{I,Poisson} = 2eIcoth(\nu) - 4k_BTG(0) \tag{2.12}$$

$$F = \frac{\sum \tau_n(1-\tau_n)}{\sum \tau_n} \tag{2.13}$$

The Fano factor F depends on the detailed geometry of the device and the electronic properties of the material, which determine the transmission probabilities τ_n. Also, in some systems, where the effective charge carrier e^* is different from e, the shot noise power spectral density S_I will change accordingly.

2.3.2 Shot noise in a tunnel junction

A tunnel junction can be modeled as two ideal Fermi reserviors seperated by a thin and tall energy barrier. From Fermi's golden rule [54], the tunneling rates are given by:

$$\Gamma_{r\rightarrow l(l\rightarrow r)} = \frac{2\pi}{\hbar}\int \mid \langle l|M(E)|r\rangle \mid^2 D^2(E) f_{r(l)}(E)\left[1 - f_{l(r)}(E)\right] dE \tag{2.14}$$

where $\langle l|M(E)|r\rangle$ is the tunneling matrix from left to right reserviors, $D(E)$ is the density of states and f is the Fermi function. To evaluate the current noise spectral density, we just sum the transmission rates across the barrier and get the well-known form:

$$\begin{aligned} S_I(V) &= \frac{2}{R}\int \{f_r(E)[1 - f_l(E)] + f_l(E)[1 - f_r(E)]\}\, dE && (2.15)\\ &= \frac{2eV}{R} coth(\frac{eV}{2k_BT}) && (2.16)\\ &= 2eIcoth(\frac{eV}{2k_BT}) && (2.17)\end{aligned}$$

This equation corresponds to Fano factor $F = 1$ in Eq. 2.13. In tunnel junctions, each channel's transmission probability τ_n is small, thus one has $F = \frac{\sum\tau_n(1-\tau_n)}{\sum\tau_n} \approx \frac{\sum\tau_n}{\sum\tau_n} = 1$. According to Eq. 2.17, at zero bias voltage, the noise spectral density reaches the Johnson-Nyquist noise $4k_BT/R$, which agrees with the fluctuation-dissipation theorem. In the limit $eV \gg k_BT$, Eq. 2.17 becomes $S_I = 2eI$. In the finite temperature limit, Eq. 2.17 gives the analytic function with the shape shown in Figure 2.6.

2.3.3 Shot noise in quantum point contact

In the Landauer-Buttiker formalism, the shot noise power in the QPC at the zero temperature limit can be described in terms of the transmission probabilities of the quantum channel by [55]:

$$S_I = 2eVG_0\sum_n \tau_n(1 - \tau_n) \tag{2.18}$$

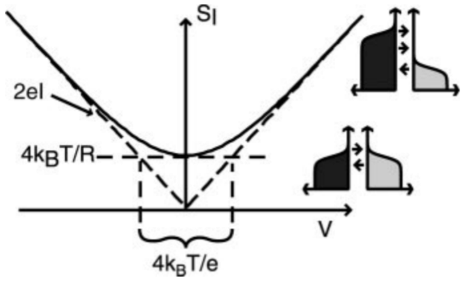

Figure 2.6 : Theoretical plot of current spectral density of a tunnel junction as a function a bias voltage. Adapted from ref [10].

As $G = 2e^2/h \sum_n \tau_n$, one can find the oscillatory behavior of the noise that closely related to the conductance value, see Figure 2.7. The noise is suppressed at positions where the conductance is quantized values, and the conducting quantum channels are fully transmitting with $\tau_n \sim 1$.

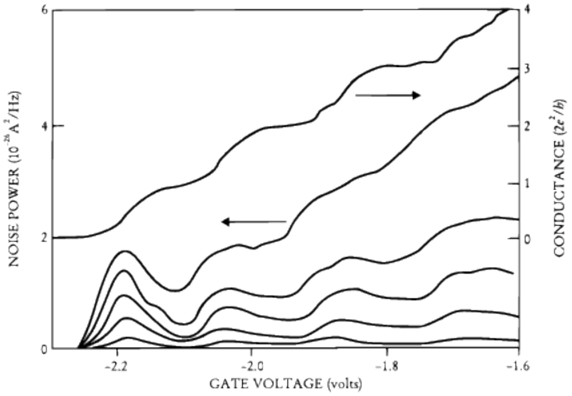

Figure 2.7 : Noise spectral density S and normalized linear conductance G vs gate voltage V_G. Adapted from ref [11].

The shot noise in a quantum point contact has been applied to measure the fractionally charged Laughlin Quasiparticle. In L. Saminadayar and D.C. Glattli's work in 1997 [12], the shot noise of the backscattering current I_B is measured in a quantum point contact for 2DES, see Figure 2.8. At Laughlin level filling factor $\nu = 1/3$, a quasiparticle tunneling through the $\nu = 1/3$ quantum Hall fluid is expected for weak coupling between opposite 1/3 edge channel. At temperature $T = 0$ and weak coupling $I_B \ll I$, the Schottky formula gives:

$$S_I = 2e^* I_B \tag{2.19}$$

where the Laughlin quasiparcle effective charge $e^* = e/3$.

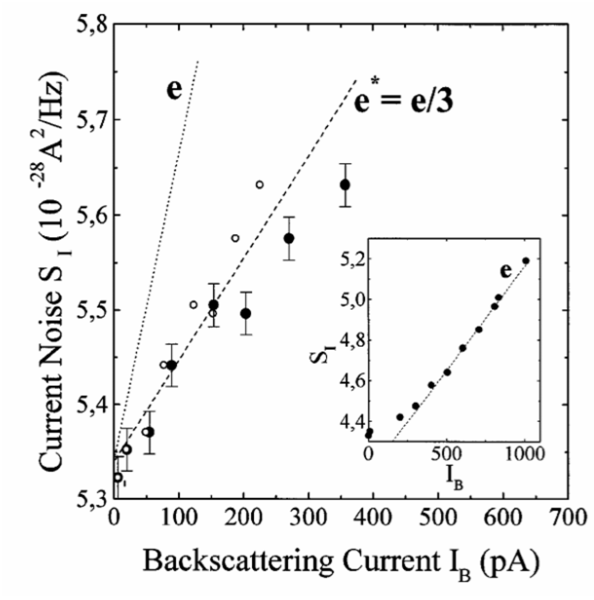

Figure 2.8 : Tunneling noise at $\nu = 1/3$ ($\nu_L = 2/3$) when following path A and plotted versus $I_B = (e^2/3h)V_{ds} - I$ (filled circles) and $I_B(1-R)$ (open circles). Adapted from ref [12].

2.3.4 Shot noise in diffusive conductor

Metallic resistors themselves can also display shot noise on several different length scales if the device is sufficiently small and cold in several different length scales [56]. To distinguish different regimes, we need to compare the following lengths: the metallic resistor length L, the electron mean free path length l, the phase breaking length L_{ϕ}, the electron inelastic collision length for thermalization L_{e-e}, and the length in which the electron temperature can relax to the phonon temperature, L_{e-ph}.

For $L_{e-ph} \ll L$, the resistor is in a macroscopic regime that it is large enough for the electrons and phonons reach global thermal equilibrium. The noise is $S_I = 4k_BT/R$ and there is no extra shot noise; For $L_{e-e} \ll L \ll L_{e-ph}$, the electron is in the interacting hot-electron regime. The electron temperature cannot be relaxed to the phonon temperature and can only be done via thermal conduction to the reservoirs. Calculation predicts $S_I = (\sqrt{3}/4)2eI$ for $eV \gg k_BT$ in this case; For $L_{\phi} \ll L \ll L_{e-e}$, the electrons do not interact during the transmission trajectory. The noise spectral density is given as $S_I = (1/3)2eI$ for $eV \gg k_BT$ then. For $l \ll L \ll L_{\phi}$, we are in the mesoscopic regime and the metal is called a diffusive metal. In this case, the noise spectral density is also found to fit with the equation $S_I = (1/3)2eI$.

Historically, the charge of Cooper pairs was first directly measured in a diffusive metal contact between Cu and Nb [13], see Figure 2.9a. The Fano factor in the diffusive wire is $F = 1/3$, and the shot noise data follows $S_I \approx 2/3 \times 2eI$ within the superconducting gap (Δ). At outside the superconducting gap, when transport should be dominated by single-electron-charged quasiparticles, the slope of S_I versus I decreases to about $1/3 \times 2eI$, see Figure 2.9b.

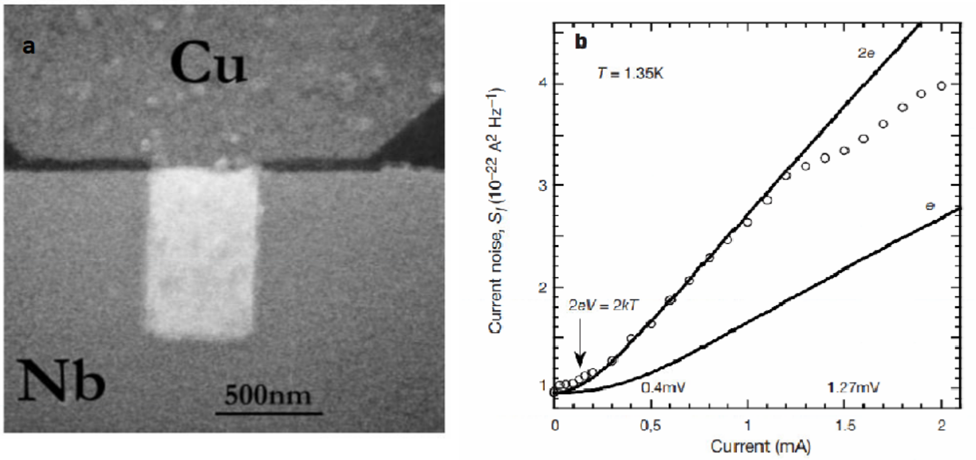

Figure 2.9 : Doubled shot noise in Cu-Nb junctions. **a**, SEM image of the device. **b**, shot noise power spectral density as a function of the d.c. bias current I. Adapted from ref [13].

2.4 Summary

In this chapter, we reviewed transport physics in the mesoscopic regime. In this regime, quantum mechanics plays an important role in transport. In the Landauer conductance channel picture, the conductance is the result of summation all possible transmission channels. With the introduction of the concept of electronic phase coherence, phenomena such as UCF, A-B conductance oscillation, and conductance quantization are well-explained. Shot noise is also a mesoscopic transport property. The shot noise Fano factor is directly related to the transmission probability of each conduction channel. In different systems, the Fano factor will have different values and leads to different shot noise spectral density. The shot noise has been successfully applied in the detection of quasiparticles with effective charges that deviate from e.

Chapter 3

High temperature superconductors

In 1911, Dutch Physicist Heike K. Onnes found that when Mercury (Hg) is cooled down to liquid Helium temperature, its resistance drops to zero [57]. This phenomenon is called "superconductivity" and the temperature where the resistance begins to drop to zero is called the superconducting transition temperature (T_c). This finding soon drew people's attention, and Onnes was awarded the Nobel prize for this in 1913. From then on, the pace of finding new superconducting materials and exploring the mechanism of superconductivity never slowed, and it has become one of the most important fields in modern condensed matter physics.

The history of superconductivity is briefly shown in Figure 3.1. With more than a century's research, people have found many different kinds of superconductors. Some are well explained by the BCS theory of superconductivity, and are called conventional superconductors; while for some species, like copper-oxide superconductors (cuprate) or iron-based superconductors (pnictide), there is still no complete understanding to their superconducting mechanism. Those are named unconventional superconductors or high temperature superconductors.

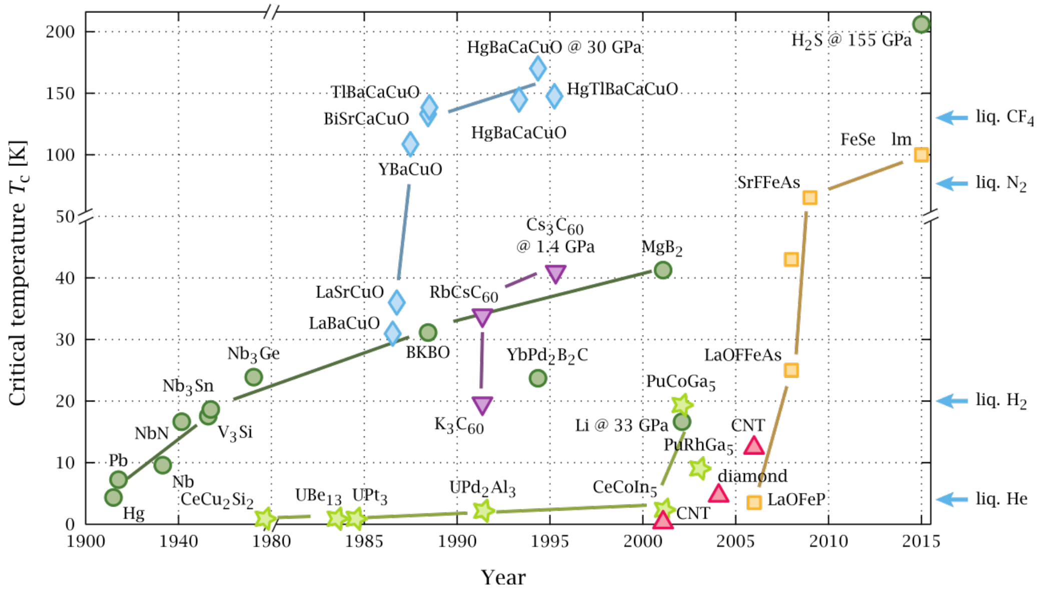

Figure 3.1 : Superconductor timeline. BCS superconductors are displayed as green circles, cuprates as blue diamonds, and iron-based superconductors as yellow squares. Adapted from wikipedia.

3.1 Conventional Superconductor

3.1.1 Properties of superconductor

In normal metallic conductors, the resistance decreases gradually toward a residual value as the material is cooled down toward absolute zero temperature. A superconductor's resistance drops abruptly to zero when the temperature is below its superconducting transition temperature. This superconducting phase is a distinct phase from the normal metallic phase and has a set of novel properties.

Besides zero resistance, there is another fundamental characteristic of superconductors. The superconductor expels magnetic flux, ie, $\mathbf{B} = 0$ within the bulk of superconductors, see Figure 3.2. For a small magnet near a superconductor, it will

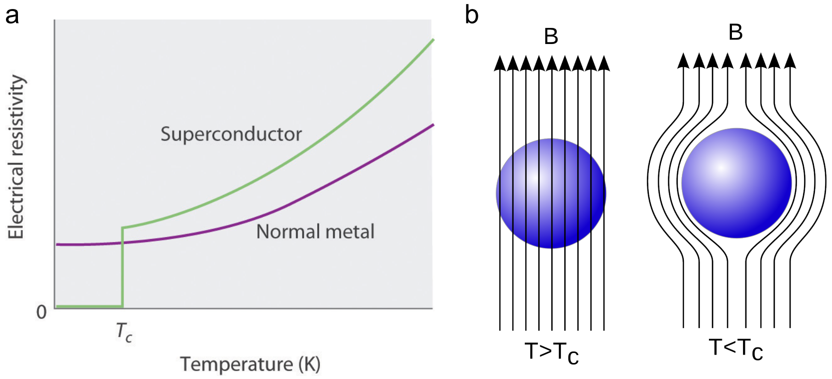

Figure 3.2 : Superconducting transition Meissner effect in superconductors.

be repelled because of the Meissner effect [58]. If a small magnet is placed above a superconductor, it can be levitated by this repulsive force. This effect has been applied to make maglev train, that can travel without the friction from a track.

3.1.2 London Equation

The first successful though non-complete explanation of the Meissner effect was achieved by Heinz and Fritz London in 1935 [59]. Based on Newton's second law, an electron inside the conductor obeys the equation $e\vec{E} = m\dot{\vec{v}}$, where $\dot{\vec{v}}$ is the time derivative of the velocity vector. We also have $\vec{J} = nev$ by definition of current, where n is the conduction electron density. Thus, we have:

$$\vec{E} = 4\pi\lambda^2\dot{\vec{J}}/c^2 \tag{3.1}$$

where $\lambda^2 = \frac{mc^2}{4\pi ne^2}$.

F. and H. London suggested that inside a superconductor, the current $\vec{J}$ and field $\vec{B}$

will have this relation:

$$\frac{4\pi\lambda}{c}\nabla \times \vec{J} = -\vec{B} \tag{3.2}$$

This is called the London equation. Combine with Eq. 3.1 and the Maxwell equation $\nabla \times \vec{E} = -\dot{\vec{B}}/c$, one obtains:

$$\vec{B} = \vec{B}_0 e^{-z/\lambda_L} \tag{3.3}$$

This implies that field $\vec{B}$ decays to zero for depths beyond the penetration depth λ_L, which is the Meissner effect.

3.1.3 Cooper pairs and BCS theory

The London equation still left many puzzles in superconductivity unsolved including its microscopic justification. A more fundamental microscopic theory of superconductivity was developed by John Bardeen, Leon Cooper and J. Robert Schrieffer in 1957, which is known as the BCS theory [32]. The key feature of the BCS theory for superconductivity is the formation of a bound state called a **Cooper pair**, which consists of two electrons with opposite momenta and opposite spins. The mechanism of the two electrons forming the Cooper pair is through a weak attractive interaction mediated by the phonon of the crystal lattice—a second electron is weakly attracted to the other due to the lattice deformation from the first electron, see Figure 3.3.

The Cooper pairs are composite bosons with net spin zero, which means all Cooper pairs can occupy the same quantum state at low temperature. This collective behavior and the resulting every gap required to disrupt pairs prevents collisions with the lattice and leads to zero resistivity. There needs to be extra energy to break all the

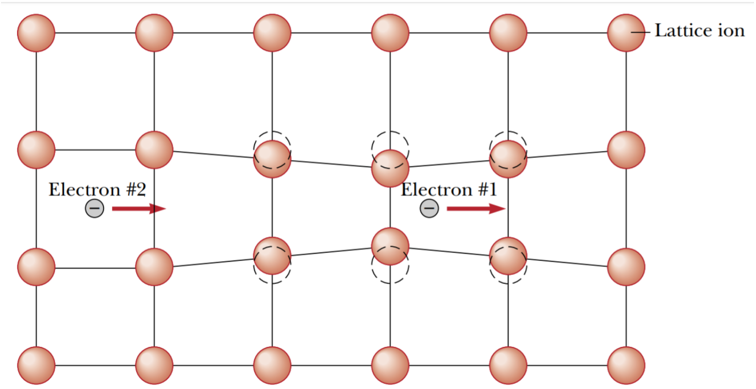

Figure 3.3 : Electrons form Cooper pairs mediated by the phonon. Adapted from Serway's textbook on superconductivity.

Cooper pairs and destroy the superconducting state. This energy Δ is called the superconducting gap. At temperatures above T_c, the superconductivity in clean conventional superconductors is quenched by the thermal break-up of the Cooper pairs.

3.1.4 Superconducting tunnel junctions

The energy gaps in superconductors can be clearly revealed by single-particle tunneling spectroscopy. The tunneling differential conductance measurement gives information about the density of states of the two tunneling electrodes. In 1960 Giaever discovered that if one side of the the tunnel junction becomes superconducting while the other side is normal conductor (SIN), the $I-V$ characteristic becomes very nonlinear [60]. As V increases, no current is observed until V reaches a threshold value $V_t = \Delta/e$, see Figure 3.4**a-c**. If both sides of the tunnel junction are superconductors (SIS), in the thermal equilibrium there is no current flowing. In this case, the voltage needs to reach $V_t = 2\Delta/e$ to let the quasiparticles below the gap on the left have access to empty states on the right, see Figure 3.4**d-e**.

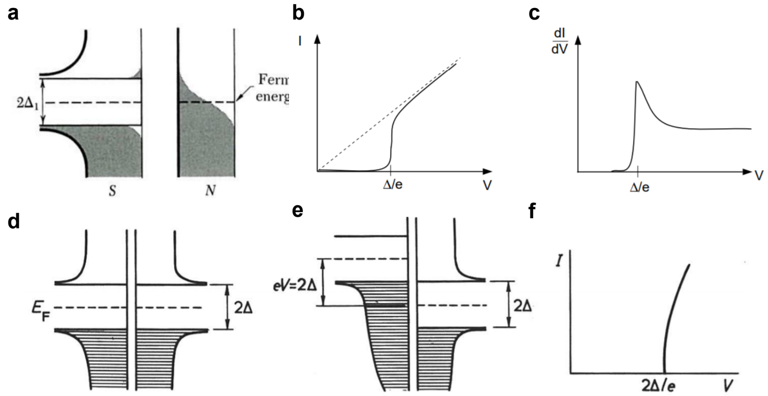

Figure 3.4 : Superconducting tunnel junction I-V and dI/dV curve. **a-c**, SIN tunnel junction Fermi level, I-V and dI/dV. **d-f**, SIS tunnel junction Fermi level and I-V curve. Adapted from Lecture notes [14].

According to BCS theory, in the superconducting states, all electrons form Cooper pairs. Single particles are not available for the tunneling process. As the voltage is raised beyond Δ, pairs break up into normal single particles, which exhibit normal tunneling properties.

However, Josephson discovered that Cooper pairs can also tunnel through the insulating barrier [61]. This occurs when the barrier is thin compared to the decay length of Cooper pair's wave functions in the barrier. In this scenario, the Cooper pair's phase at each superconductors δ_1 and δ_2 are correlated over the barrier and the two superconductors act as coupled oscillators. Feynman provides the most accessible description to the Josephson effect with the following equations:

$$J(t) = J_0 sin\delta(t) \tag{3.4}$$

$$\delta(t) = \delta_0 + \frac{2e}{h}\int V(t)dt \tag{3.5}$$

where J is the Josephson current density, $\delta(t)$ is the phase difference across the junction and V is the voltage across the junction. These equations provides the explanation to the DC and AC Josephson effect, which limited by the scope of the dissertation we will not go to the details here.

3.1.5 Quasiparticles in STJ

In the BCS theory, the Cooper pairs are all condensed into the same ground quantum state at low temperatures without excitation. The Bogoliugov quasiparticles are elementary excitations above the ground state, which are linear superpositions of the excitations of negatively charged electrons and positively charged holes. Therefore, they are neutrally charged fermions with spin $\frac{1}{2}$ [62]. The expectation value of the charge for a Bogoliugov quasiparticle is smaller than the charge of an electron [15].

The SIS Josephson junctions exhibit a unique signature in the shuttled charge quantum under various bias conditions. [15] At zeros bias limit, the Josephson current is carried by Cooper pairs, which have twice the electron change. At bias $eV_{SD}/\Delta < 2$, Andreev reflection process is involved at the interface between superconductor and normal state (insulator). In the Andreev reflection process, an electron incident on the interface between a normal conductor (insulator) and superconductor produces a

Cooper pair in the superconductor and a retroreflected hole in the normal conductor (insulator). In bias range $\frac{2\Delta}{n-1} > eV_{SD} > \frac{2\Delta}{n}$, multiple Andreev reflections (MAR) happen at the interface, and the leading charge contribution to the current is ne, see Figure 3.5. At above the superconducting gap 2Δ, the Andreev reflection is suppressed and the process becomes a single particle tunneling process and the charge $e^* = e$.

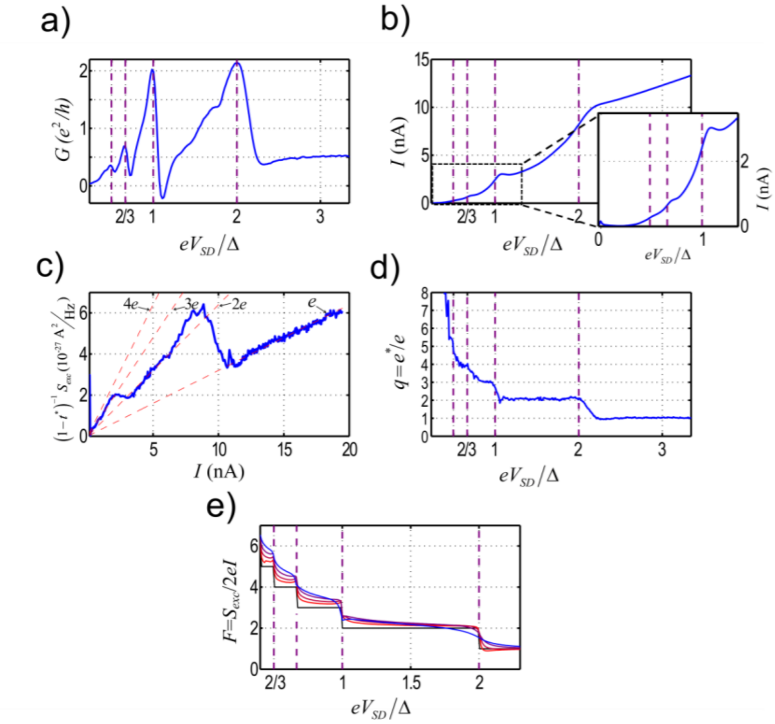

Figure 3.5 : Shuttled charges in the MAR process. **a**, Differential conductance as a function of applied bias. **b**, The I-V characteristics as obtained by integrating the differential conductance. **c**, The shuttled charge q determined as a function of eV_{SD}/Δ. The pronounced staircase demonstrates the quantization of charge involved in the MAR processes. (d) Numerical simulations of the Fano factor, $F = S_{exc}/2eI$, as function of eV_{SD}/Δ for different values of the normal-region transmission t=0.4, 0.2, 0.1, 0.05. **e**, The normalized excess noise (after dividing the excess noise by (1-t^*)), as a function of the current. Adapted from ref [15].

3.2 Unconventional Superconductor

The BCS theory has successfully explained many conventional superconductors like Hg, Al, Nb, etc. However, during the last four decades, many new types of superconductors have been found and their properties are quite different in some ways from traditional superconductors. There is still no clear consensus about the mechanism for the formation of Cooper pairs in these superconductors yet. Developing a more general theory for explaining the superconductivity in these materials is a challenging but important task for physicists nowadays.

3.2.1 Types of unconventional superconductors

- **Organic Superconductors** This discovery of superconductivity in pressurized organic compound $(\mathrm{TMTSF})_2\mathrm{PF}_6$ by Jérome et al. in 1979 [63] created great excitement in the field of superconductivity. The TMTSF is a Bachgaard salt, a representative material for a group of superconductors that contain organic compound. Other organic superconductors include two-dimensional $(\mathrm{BEDT\text{-}TTF})_2\mathrm{X}$, doped fullerenes, TTP-based SCs, etc [64]. These superconductors attracted interest because of a large range of new phenomena, such as the competition between various ground states, the quantization of Hall effect, the influence of a magnetic field on a quasi-one-dimensional conductor, etc. Furthermore, some theoretical proposal for high T_c superconductivity [65] was based on a organic polymer systems.

- **Heavy Fermion Superconductors** Heavy fermion materials are a class of compounds named for the large effective mass of their charge carriers. The superconductivity in heavy fermion was first discovered in $CeCu_2Si_2$ at 1979 [66]. In the heavy fermion materials the superconducting Cooper pairs are not formed from ordinary conduction electrons, but are rather composed of quasiparticles with enhanced effective masses. The energy scale associated with these quasiparticles is even smaller then the Debye energy, such that the retardation effect in the phonon-based BCS theory does not provide sufficient attraction to overcome the Coulomb interaction. These characteristics made it clear that heavy fermion superconductors are not conventional superconductors, and became a new area of research on unconventional superconductivity.

- **Copper-oxide Superconductors (Cuprate)** Cuprate superconductors are high temperature superconductors made of copper-oxide. The main component that hosts the superconductivity is the CuO_2 layer separated by spacer layers. In 1986, Bednorz and Müller from IBM Zurich discovered superconductivity near 40 K in the layered cuprate $La_{2-x}Ba_xCuO_4$ [31]. The superconductivity in cuprates was soon found in many other materials, and the superconducting transition temperature T_c was boosted up to 90 K soon in $YBa_2Cu_3O_7$ [67]. The implications of cuprate superconductivity are so profound that Bednorz and Müller were awarded the Nobel prize only one year after their discovery. The highest superconducting temperature in cuprate was found in $HgBa_2Ca_2Cu_3O_{8+x}$ at above 150K under applied pressure [68].

- **Iron-based Superconductors (Pnictide)** Iron-based superconductors started with the discovery of superconductivity in LaFePO at 4 K in 2006 [69]. At 2008 the T_c was increased to 26K in LaFeAsO$_{1-x}$F$_x$ [70], which brought more excitement to the superconductivity community. With recent years' development, the iron-based superconductors have been extended to a large variety of materials, such as 1111 (eg, LaFePO [71]), 122 (eg, Ba$_{0.6}$K$_{0.4}$Fe$_2$As$_2$ [72]), 111 (eg, LiFeP [73]) and 11 (eg, FeSe [74]) types of families. This new type of superconductors draw much of the interest because the new compounds are very different from cuprates and may help lead to the development of non-BCS-theory superconductivity.

- **Other New Types Superconductors** In 2018 Jarillo-Herrero's group at MIT announced that they had found superconductivity in a **twisted bilayer graphene**—two atomic-thick sheets twisted exactly 1.1° [16], see Figure 3.6. This discovery was a big surprise to the solid-state physics and it aroused an intensive race among condensed-matter physicists to explore and explain their results. The easy-accessibility of graphene offers researchers a much simpler platform for studying novel physics. Furthermore, this finding indicates that remarkable properties arise from strong correlation between electrons, which is thought to be the origin of bizarre states in more complex materials.

3.2.2 Puzzles in unconventional superconductors

Since the discovery of unconventional superconductors, their many strange behaviors are still unexplained. The following are some of the most intriguing problems:

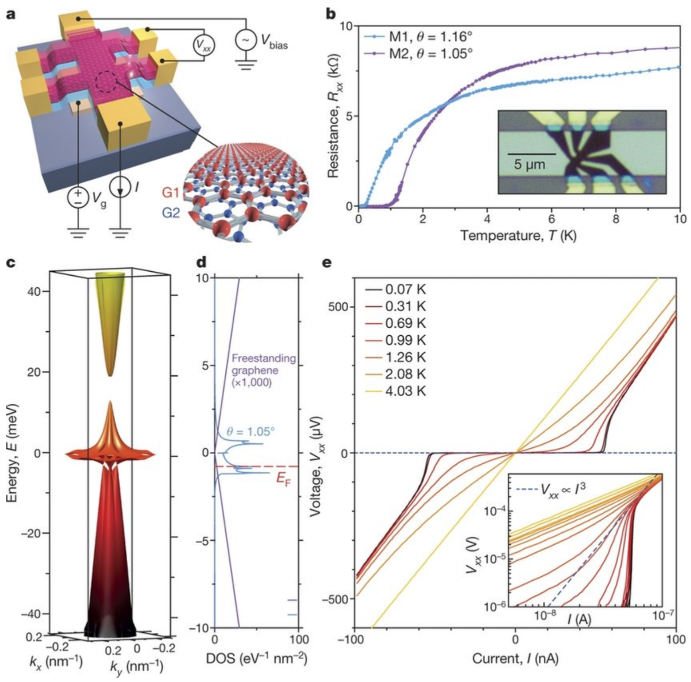

Figure 3.6 : Superconductivity in twisted bilayer graphene. Adapted from ref [16].

a Why is T_c so much higher than the conventional superconductors? This is probably one of the most important questions in the study of high temperature superconductors. Based on conventional phonon-based BCS theory, McMillan predicted that conventional superconductors' transition temperature cannot be higher than 40K, which is the McMillan limit [75]. But the high temperature superconductors broke this limit and reached T_c much higher than the McMillan limit. What kind of mechanism could provide the pairing glue at such high temperatures is one of the most fundamental questions that remain to be revealed.

b What is the relation between HTC and magnetism? For very long time it was believed that superconductivity and magnetism were mutually exclusive phenomena. But with the study of cuprate and pnictide superconductors, it was found magnetism and HTC can be closely correlated. Different from conventional superconductors, almost all high temperature superconductors are obtained from doping electrons or holes into anti-ferromagnetic parent compounds. With high mobility electrons or holes doped into the anti-ferromagnetic compound, the long range magnetic order is destroyed. But neutron diffraction results showed that all doped samples host short range anti-ferromagnetic spin fluctuation (magnon) [76]. Analogous to phonons, magnons are also hypothesised to work as a mechanism for electrons to form Cooper pairs.

c What gives rise to the complex phase diagrams of unconventional SCs? Different from conventional superconductors, the high temperature superconductors have very complicated phase diagrams, see Figure 3.7. In Landau's theory of phase transition with several order parameters, usually only one order is strongest and the others are suppressed. Regimes in which orders have similar T_c's are exceptional and require fine tuning. The complex phase diagram suggests that all the observed orders may have a common physical origin and are interwined. This is supported by the evidence that stripe and nematic local order in exquisite detail in BSCCO on a broad range of temperatures, voltage and field by STM measurement [77].

d How do we understand the "bad metal" or "strange metal" behavior in many highly correlated materials at temperatures above T_c? The "normal" phase of

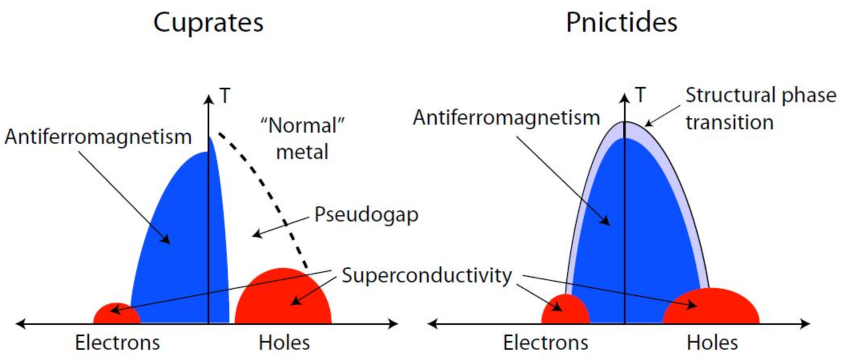

Figure 3.7 : Phase diagram of cuprate and pnictide. Adapted from Lanzara Research Group.

high temperature superconductors is not a good metal—it has abnormal T-dependent of $\rho(T)$, high resistivity value, apparently implying mean free path shorter than inter atomic distance. The electronic quasiparticles seem not well defined in this phase. Recently, research found "stripes" of electronic charge in the bad metal phase [78], which may play a key role in superconductivity.

3.3 Cuprate superconductor

In this dissertation, we measured shot noise in a cuprate superconductor $La_{2-x}Sr_xCuO_4$. Here we examine the properties of cuprates for a better understanding of this material.

The cuprate superconductors are closely related to the perovskite structure. These copper-oxides have a layered crystal structure consisting of CuO_2 planes, which may be doped with electrons or holes, see Figure 3.8. As Figure 3.7 shows, the undoped parent compound or weakly doped cuprate is an anti-ferromagnetic Mott insulator.

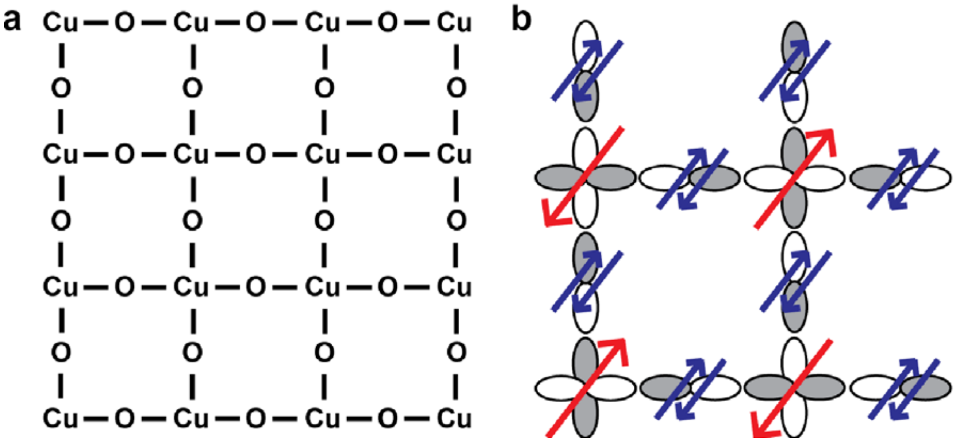

Figure 3.8 : The CuO_2 plane characteristic and localized spin configuration of cuprate superconductors. Adapted from ref [17].

For example, La_2CuO_4 shows three-dimensional long range anti-ferromagnetic order at $T_N \sim 300$K. The electronic configuration of Cu^{2+} is d^9 and each copper ion in the CuO_2 plane contributes one unpaired d orbital electron. Thus, based on the band theory, the undoped cuprate should be metallic. However, because of the strong Coulomb repulsion between *d* orbital electrons, the d electrons are confined around each Cu lattice site and cannot move freely.

On doping holes, the anti-ferromagnetic Mott insulating phase disappears and superconductivity emerges. T_c follows a dome-like shape as a function of doping, with an optimum T_c around 15% doped. In LSCO a similar phase diagram is seen on doping electrons, albeit with a more robust anti-ferromagnetic phase and a lower T_c.

On the hole-doped side, there exists an mysterious state above T_c called the pseudogap, where the electron density of states within a certain momentum region is suppressed, see Figure 3.9. There is another temperature T^* in the phase diagram

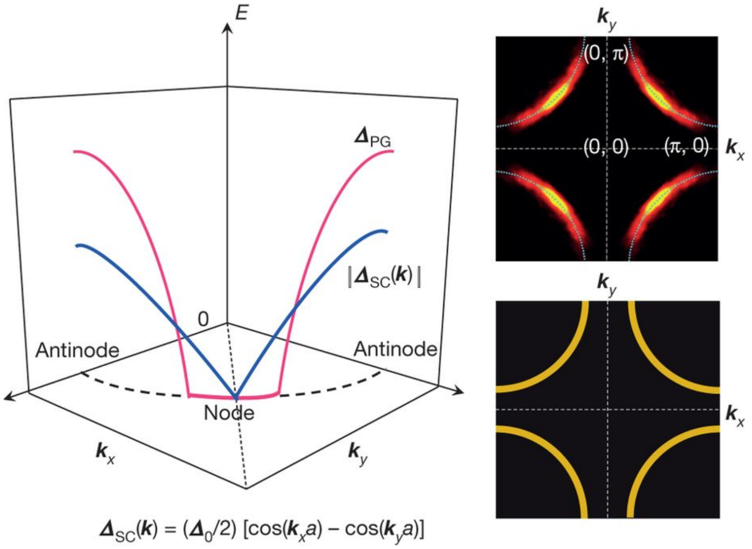

Figure 3.9 : Evidence of pseudogap observed by ARPES and STS for overdoped cuprate. Once the pseudogap sets in, the antinodal regions of the Fermi surface near the Brillouin zone edge are gapped out, giving rise to Fermi arcs (top right). This is reflected (left) in the angle dependence of the energy E of the superconducting gap Δ_{SC} (blue line) and pseudogap Δ_{PG} (red line) as functions of the momenta $\mathbf{k}_x$ and $\mathbf{k}_y$ in one quadrant of the Brillioun zone around the underlying large Fermi surface (dashed curve), as revealed by ARPES and STS. Adapted from [18].

corresponding to the onset of pseudogap. Back in 1989, NMR result [79] showed that in underdoped $YBa_2Cu_3O_{7-\delta}$, the spin-lattice relaxation time is suppressed at temperatures much higher than T_c, which suggests that there exists an energy gap in the spin-polarized excitation spectrum. Later on in many different hole-doped cuprate and under various different probe methods scientists confirmed that an energy gap is already open at above T_c, not only in spin excitation but also in electron excitation. That is what we called the "**pesudogap**". There have been many studies on the pseudogap phase, the NMR spectroscopy [79], ARPES [80, 18], optical THz conductance [19], onset of diamagnetism [81], temperature-dependent resistivity, and Nernst effect [82] all give characteristic temperatures T^* above T_c, see Figure 3.10.

As the pseudogap phase is right above the superconducting transition in the phase diagram, the relation between the pseudogap and superconductivity has been a focus of interest for a long time.

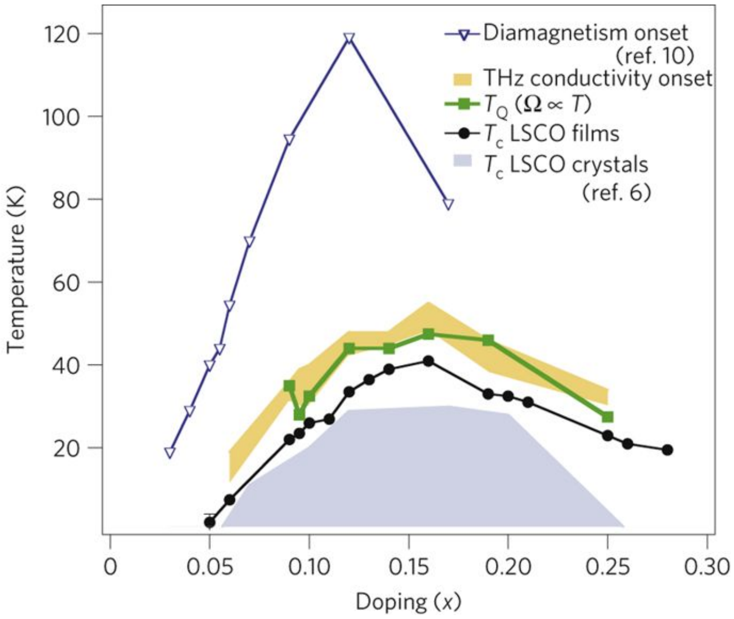

Figure 3.10 : Phase diagram of the onset of superconducting correlations in LSCO. Adapted from ref [19].

So far there are many theories trying to explain the relation between the pesudogap and superconductivity. Those can be categorized into two main groups [83]:

a The pseudogap is the precursor of superconductivity

In this concept, superconductivity is deeply based on the basis of the pseudogap [2, 84, 85]. This concept that pseudogap is intrinsic to superconductivity leads to the phase fluctuation scenario [86], stripe-based theories [87, 88] as well as pair fluctuation approaches [85]. In those theories, the Cooper pairs are already formed at a temperature way above T_c, but that long-range phase coherence is not established until the temperature drops below T_c. Below T_c, there is global phases coherence, leading to Meissner effect and zero resistivity. Such phase fluctuations usually play an important role in lower-dimensional systems, e.g., in a magnetic materials the local moments form far above the temperature at which they become ordered.

b The pseudogap is not directly related to superconductivity

In this class of theories, the pseudogap comes from the fluctuations of other competing orders, such as magnetic order fluctuation [89], hidden broken symmetry [90, 91], or band-structure effect [92]. In this picture, there exists a quantum critic point (QCP) at absolute zero temperature and certain doping level p_c. The extrinsic pseudogap approach is mainly formulated at a mean-field level, which can be reasonably justified on the fact that experiments seem to indicate only a narrow critical regime. [93]

3.4 Summary

In this chapter we briefly introduced the conventional superconductivity and unconventional superconductivity. The phonon-based BCS theory succeed in explaining the conventional superconductivity while the mechanism of unconventional superconductivity is still not well understood. The pseudogap may be the key to solve the puzzles of unconventional superconductivity as it is right above the transition temperature in the phase diagram. Various types of theories have different interpretations to the pseudogap phase and it is important to distinguish which one has more experimental evidence.

Chapter 4

Experimental Methodology

Good tools are a prerequisite to success. Measurement instruments are critically important in experimental physics. Good and reliable experimental setups and scientific experimental designs are necessary to reach any solid conclusion. Modern experimental condensed matter physics is built on many cryogenic systems to reach ultra-low temperatures, strong magnetic solenoids to apply high fields, and precise electronic instruments to detect small signals. In this chapter, I will introduce some commonly used experimental techniques and instruments that are used in this research.

4.1 Cryogenic systems

Scientists began experimenting with very cold temperatures in the 19th century. The major methods to achieve cold temperature is through liquefied gasses. Throughout the years, many pioneers have developed more sophisticated methods to create increasingly colder temperatures. During this process, scientists liquefied all the known permanent gasses and also discovered much new physics at low temperatures, such as the discovery of superconductivity in ^{4}He [57] and super-fluidity in ^{3}He [94].

In this work, most of the measurements were performed in a PPMS, a commercial automated low-temperature, and magnet system for measurement of material properties made by Quantum Design. The sample is mounted on a PPMS puck, and then the puck can be loaded into the sample chamber. By pumping on liquid helium, the system can reach temperatures below the atmospheric pressure boiling point of ^{4}He, 4.2 K. External magnetic field could be applied to the sample by a superconducting solenoid immersed in the liquid Helium. The temperature of the system can be varied continuously between 1.9 K and 400 K, while the magnetic field can be tuned between ±9 T.

In some extreme cases, where we need to cool the system to the mK range, a dilution refrigerator is needed. A ^{3}He/^{4}He dilution refrigerator can provide continuous cooling to temperature as low as 2 mK. The cooling power is provided by the entropy increase of mixing ^{3}He and ^{4}He isotopes. Inside the mixing chamber, the process of moving the ^{3}He through the concentrated phase to the dilute phase is endothermic and removes heat from the chamber environment.

4.2 Device fabrication techniques

Nanoscience and nanotechnology open many possibilities in fundamental research and the industrial revolution. All these rely on nano-scaled fabrication techniques. In this dissertation, many nano-fabrication techniques are utilized for the research. Here is a brief walkthrough of those techniques that are mentioned in the future chapters.

4.2.1 Photo/E-beam Lithography techniques

Lithography is the process of transferring some geometric shapes on a mask to a smooth surface. It is one of the most intensively used techniques for making integrated circuits. The general idea of lithography is using some sensitive chemical resist and by degrading certain areas of the resist to create some uncovered regions on substrate. Through the degrade process used to the chemical resist, lithography can be categorized as photolithography, e-beam lithography or focused-ion-beam lithography, etc. The basic photolithography and e-beam lithography process are shown in Figure 4.1.

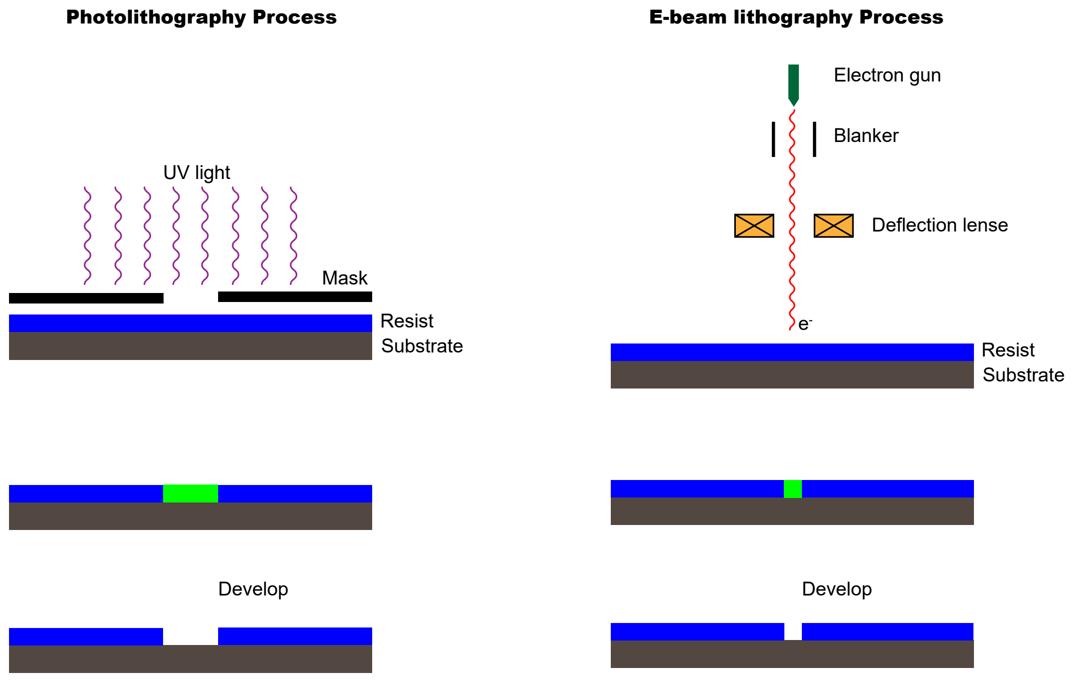

Figure 4.1 : Schematic illustration of positive-tone photolithography and e-beam lithography processes.

For photolithography, we first create a photomask, which is usually made from glass and with one side coated with opaque metal like chromium. The coating leaves out some designated space where UV light can transmit through. Then, we spin-coat the target substrate with photoresist. Usually, we use a positive-tone Shipley S1813 as the resist. The coated substrate is covered and tightly contacted by the photomask, and UV light is radiated onto the resist through the mask. The development process removes the photoresist in radiated areas, and the pattern is transferred from the mask to the substrate.

E-beam lithography shares similar processes. In e-beam lithography, we use e-beam resist polymethyl methacrylate (PMMA) instead of photoresist. PMMA 450 (number stands for the typical length of the polymer chain) is thin and good for fabricating fine structures; PMMA 450/PMMA 950 bilayer resist is good for smooth lift-off. E-beam lithography is mask free. We can define arbitrary patterns and use a focused electron beam to sweep across the pattern. The area radiated by the e-beam will degrade and be washed away in developer. As the resolution is limited by the wavelength, the e-beam lithography has much higher (∼1 nm) compared to photolithography (∼100 nm).

4.2.2 Material evaporation/deposition

Evaporation is a common method for thin-film deposition. In the evaporation process, the target material is heated up by a high energy electron beam (e-beam evaporator) or heat source (thermal evaporator). For any material, there exists a finite vapor pressure, thus after heating, the material either sublimes or evaporates. As the chamber pressure is extremely low, the material vapor can travel to the substrate without too much scattering. A quartz resonator is installed closed to the target to monitor the thickness of evaporated material. With material deposited onto the quartz resonator, the oscillation frequency of the resonator will shift.

The evaporation method has the advantage of high purity due to ultra-high vacuum. Also, if we can precisely control each crucible's temperature, we can realize more complex applications include the co-deposition of several components. However, the evaporation method has poor step coverage, and it is difficult to form alloys. Also the process is relatively slow compared to other deposition techniques like sputtering or electroplating.

4.2.3 Reactive-ion etching

Reactive-ion etching (RIE) is a dry etching technique that widely used in microfabrication processes. Different from wet chemical etching that uses corrosive chemical solutions to etch the material, RIE uses chemically reactive plasma to remove material grown on wafers. The plasma is generated under low pressure and electromagnetic field excitations. High-energy ions from the plasma attack the surface of the material both physically and chemically to etch away the material layer by layer.

In this dissertation, RIE is mainly used for several purposes. The first is to clean up photoresist/e-beam resist residue after development to improve the contact between substrate and evaporated material. Secondly, we used RIE to etch the deposited film material into certain defined shapes, and fabricate the device based on the remaining material. At last, occasionally, we used RIE to activate the surface of polydimethylsiloxane (PDMS) to increase its adhesion to use it to pick up some 2-D materials.

4.3 Conductance measurement

4.3.1 Conductance and I-V measurement

Transport measurement is one of the basic tools in the study of materials. The linear resistance of the sample can be calculated using Ohm's law:

$$R = \frac{V}{I}$$

where V is the voltage across the sample and I is the current. Conductance (G) is defined as the reciprocal of the resistance by $G = 1/R$.

The most direct and simple way to measure the resistance/conductance is the two-terminal measurement method, where current I is applied to two leads of the sample, and the voltage V is also measured at the same leads, see Figure 4.2 a. However, the two-terminal measurement result may not be accurate when contact resistance is taken into consideration. Usually, the contact between our interesting material and metal lead is not perfect. The work function mismatch and scattering between different materials causes the contact resistance R_C. In this case, four-terminal sensing, which is also known as Kelvin sensing, is necessary to remove the contact resistance contribution, see Figure 4.2 b. To avoid Joule heating and remain in the linear response regime, small a.c. excitation is preferred. With the lock-in amplifier, both current and voltage can be measured with very high accuracy. Also, we can sweep the d.c. current or voltage and measure the corresponding response to obtain the *I*-*V* curve.

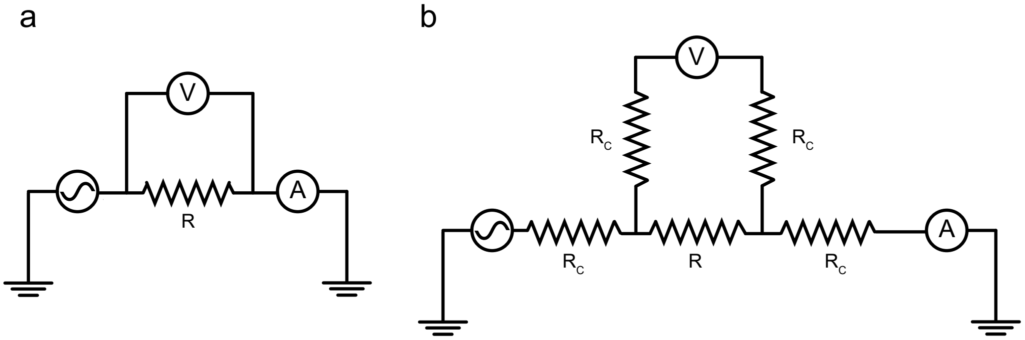

Figure 4.2 : Two terminal and four terminal sensing for resistance measurement.

4.3.2 Differential conductance measurement

The differential conductance dI/dV is a measure of how much change in I when the bias V is changed by a small amount. The device conductance reaches a maximum value at voltages where the electrons are most active. In tunneling device, dI/dV is directly related to the density of states and is widely used to study the DOS property. dI/dV can be obtained by numerically differentiating the *I*-*V* curve. However, high quality numerical differentiation requires highly accurate and smooth *I*-*V* measurements. We can also directly measure dI/dV by superimposing a low amplitude a.c. excitation on a stepped d.c. bias; then using a lock-in amplifier to measure the resulting a.c. voltage across the device and the a.c. current through the device.

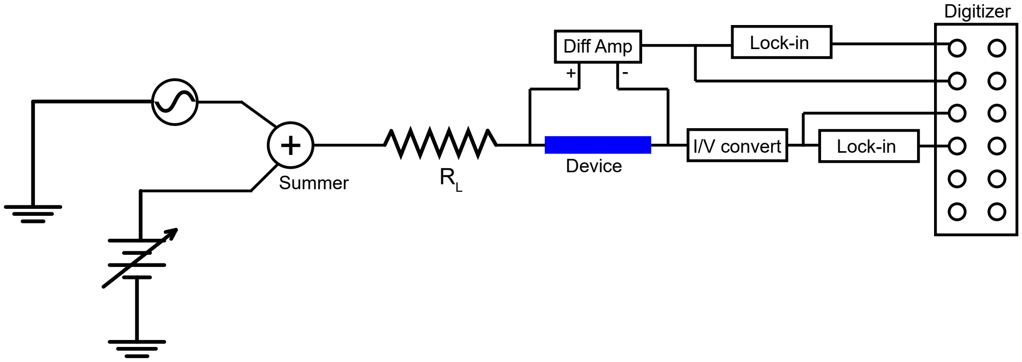

Figure 4.3 : Schematic figure of differential conductance measurement setup.

The schematic figure of the differential conductance measurement is shown in Figure 4.3. In our experiment, we use a home-made voltage summer to sum a variable d.c. voltage source and a fixed a.c. voltage source from a lock-in amplifier. Then, a large limiting resistor R_L is used is to limit the current through the device. The current is converted to voltage by a current amplifier. The d.c. component and a.c. component of the converted voltage is measured by a high-speed digitizer and a lock-in amplifier separately. Similarly, the voltage across the device is amplified by a differential voltage amplifier and measured by the digitizer and lock-in amplifier. This measurement gives all I, V, dI, and dV information, thus we can map the V-dI/dV relationship.

4.3.3 Inelastic features—d^{2}I/dV^2 measurement

Inelastic electron tunneling spectroscopy (IETS) is an experimental tool developed to study the vibrational modes of a device supporting quasiparticles transport. It can be revealed by the d^2I/dV^2 signal. As shown in Figure 4.4, in addition to direct tunneling, electrons with sufficient energy may excite the lattice vibrations or other modes, and the result is a change of slope in the $I - V$ curve. The change of slope will lead to a step function in the dI/dV vs V curve and then to a peak/dip in the second derivative of the current with respect to the voltage.

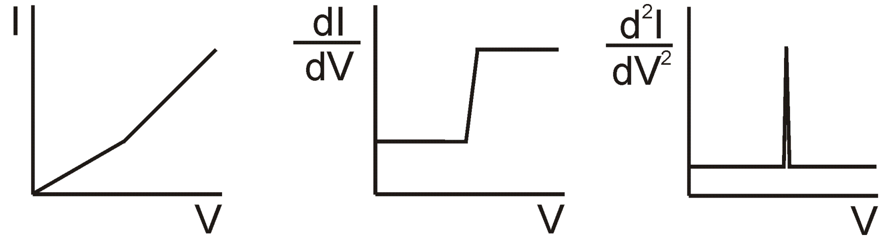

Figure 4.4 : The slope change in the I-V leads to a step in the dI/dV-V curve, thus to a peak in the second derivative of the current to the voltage.

Similar to the idea of obtaining dI/dV via measurement, the second derivative of current can also be numerically calculated from the I-V or dI/dV-V curve. Repeated measurement and smoothing can improve data quality after differentiation. Also, we can directly read the second harmonic of the current signal using a lock-in amplifier referenced at the second harmonic of the driving a.c. frequency. The driving voltage is a small a.c. wiggle $V_{ac}sin\omega t$ superimposed on a stepped d.c. voltage V_{dc}, the corresponding current is:

$$I(V_{dc} + V_{ac}sin\omega t) = I|_{V_{dc}} + \frac{dI}{dV}|_{V_{dc}}V_{ac}sin\omega t + \frac{1}{2}\cdot\frac{d^2I}{dV^2}|_{V_{dc}}V_{ac}^2sin^2\omega t \tag{4.1}$$

$$= I|_{V_{dc}} + \frac{dI}{dV}|_{V_{dc}}V_{ac}sin\omega t + \frac{1}{4}\cdot\frac{d^2I}{dV^2}|_{V_{dc}}V_{ac}^2(1 - cos2\omega t) \tag{4.2}$$

Referenced at 2ω, the lock-in amplifier's reading represents the value of $I_{lock-in} = -\frac{1}{4}\cdot\frac{d^2I}{dV^2}|_{V_{dc}}V_{ac}$. Thus, the second differential of current $\frac{d^2I}{dV^2}|_{V_{dc}} = -\frac{4I_{lock-in}}{V_{ac}^2}$.

4.4 Shot noise detection

Shot noise provides rich information about the quantum transport properties of the underlying quasiparticles and the inelastic scattering events during the transport. As the key point of this research is to detect shot noise in some complicated systems, developing the right method and accurately measuring the shot noise are the most important tasks. Several techniques have been developed over the years in our lab to reach both qualitative and quantitative accuracy for shot noise detection [95, 96].

4.4.1 Radio frequency noise measurement

The radiofrequency (RF) measurement technique is adapted from previous pioneers' work described in ref [95]. By using RF measurements, we only focus on a high-frequency range (250MHz-600MHz); hence the technique is less sensitive to some low-frequency background noise sources, such as 1/f noise. Instead of using the cross-correlation method to suppress the noise background, we adapted a combination of modulated bias and a lock-in detection scheme to reach high sensitivity by measuring the excess noise $S(V) - S(0)$.

Our measurement mainly focuses on the excess noise of $S_I(V) - S_I(V = 0)$. The schematic of the circuit is shown in Figure 4.5. A function generator (Stanford Research DS-345) is used to apply a square wave bias switching between zero voltage and a finite voltage at ∼5 kHz across the junction sample. At the zero-voltage state, the sample is in equilibrium, and only thermal noise exists in system, whereas in the finite-voltage state, the tunneling current will contribute to extra shot noise. The excess shot noise is the noise difference between the finite-voltage state and zero-voltage

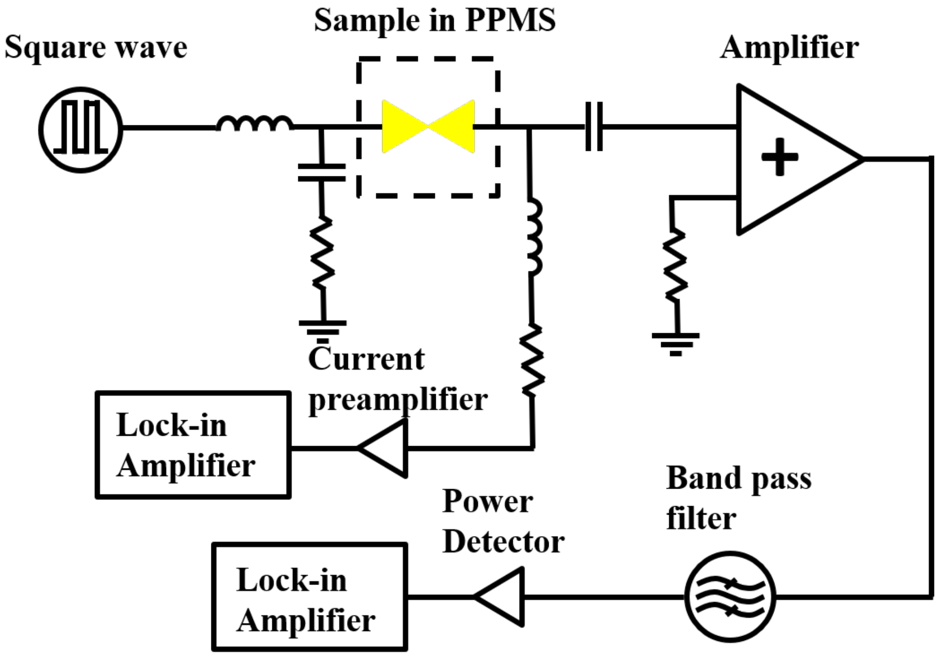

Figure 4.5 : Schematic figure of RF shot noise measurement setup.

state. A bias-tee separates the d.c. and RF signals collected from the junction. The d.c. component is amplified by a current pre-amplifier (SR570) and measured by a lock-in amplifier (model SR 7265). The RF component, which contains the fluctuation information, is first filtered by a 250 MHz-600 MHz bandpass filter (mini-circuits), then amplified (3 mini-circuits power amplifiers, model ZX60-33LN+, 5V bias) and measured by a logarithmic power detector (mini-circuits, model ZX47-60LN+) to converted into a voltage output. A second lock-in amplifier (SR 7270) also synchronized to the square wave detects the difference between the power detector's output corresponding to finite-voltage and zero-voltage. This difference combined with the detector's average output can finally be translated to the noise power at finite-voltage and zero-voltage, and hence give the excess shot noise.

The sensitivity of the RF shot noise measurement is mostly limited by the first amplifier's input noise, which is a typical ~1 dB in the noise figure. If the extra shot noise intensity is smaller than the background noise level, the on and off states' power detector reading will not have a detectable change; thus, this measurement method fails. Recently, some SiGe based bipolar transistor amplifiers are verified to work in cryogenic temperatures and have very small input noise at low temperatures [97]. More studies have been done now trying to replace the first power amplifier with such cryogenic amplifiers.

As the RF signal is notorious for suffering from impedance mismatch and decaying when passing through cables and connectors, the RF signal measured by the detector is only part of the total shot noise generated at the junction. The present RF shot noise apparatus has been upgraded to be more RF compatible, and the detection efficiency is increased by order of magnitude and reaches more than 10% at low temperatures. More details of the calibration will be discussed in the later sections. The background of this measurement setup can be as small as 10^{-27} A^2/Hz, which corresponds to a current around 100 nA in a Poissonian system ($S_I = 2eI$), and could be considered as small excitations of the measuring system.

It is worth noting that this measurement has an important assumption that the sample's resistance does not vary (or does not vary too much) in the whole bias range. If the resistance/conductance varies a lot, the current thermal noise $4k_BTG$ at finite bias would be greatly different from the zero-bias value. Thus $S_I(V) - S_I(V = 0)$ could not be simply interpreted as excess shot noise anymore.

4.4.2 Low frequency noise measurement

The cross-correlation technique can be used to find similarities between different signal channels and has been successfully applied in shot noise detection from some previous work [98]. Here we also developed a low-frequency cross-correlation setup to measure the shot noise. Figure 4.6a shows a schematic electrical circuit diagram of the experimental setup. A tunable voltage source (NI-DAQ6521) is heavily filtered with LC filters (>60 dB attenuation at frequency beyond 100 Hz) to provide a clean bias. Two larger resistors (∼200 kΩ each) are used to limit the input current. The sample is loaded inside a cryostat (PPMS from Quantum Design) using a home-built shot noise probe with careful shielding and isolation from the PPMS ground and environment. The voltage noise across the sample is amplified by two low-noise voltage pre-amplifier chains independently, each with the total gain 10,000 (LI-75 followed by SR-560), and recorded by a high-speed digitizer (NI-PCI5122) at a sampling rate of 5 MHz within 10 ms for each time series. The noise signal is very sensitive to the environment, and a Faraday cage (dash line in Figure 4.6a) is crucial to minimize interference from background electromagnetic signals. The voltage fluctuations in the two amplifier chains are cross-correlated to suppress contributions from amplifier noise (nominally uncorrelated between the two chains). The cross-correlation analysis finds the in-phase components between the two time series signals and gives the power spectral density of the correlated components. Each measurement of the power density spectrum of noise is an average of 4,000 of these cross-correlations, and it takes about 1.5 min.

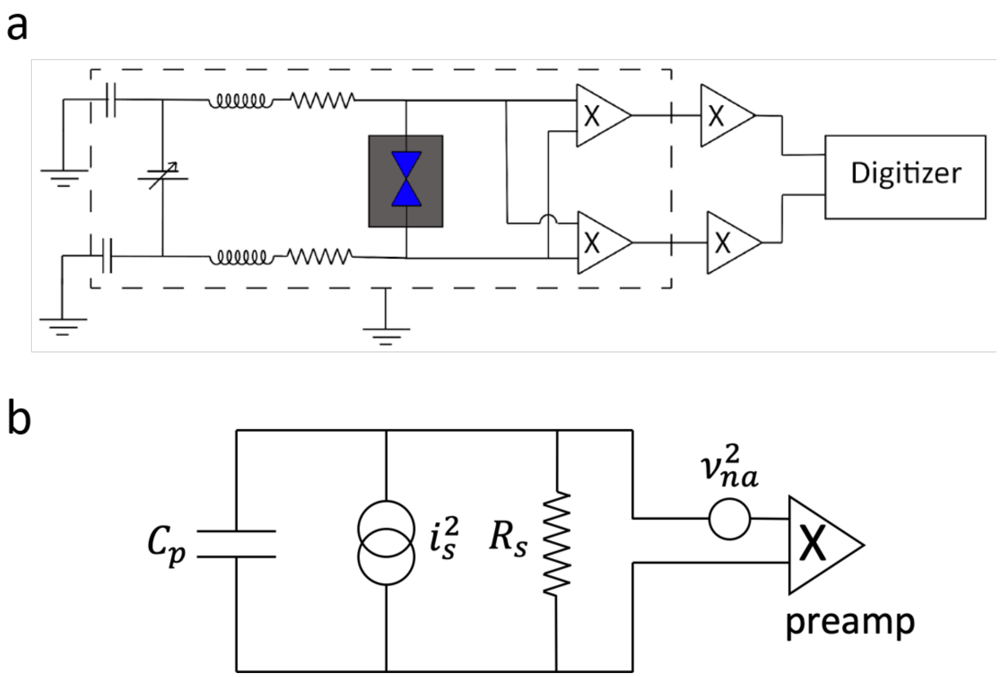

Figure 4.6 : Schematic figure of low frequency cross-correlation shot noise measurement setup.

Resistive and capacitive parasitic contributions are unavoidable in this measurement approach. While the parasitic series resistance (on the order of Ω) is negligible compared with the typical sample differential resistance (on the order of kΩ), the parasitic capacitance to the ground may affect the measured noise spectrum. For a standard treatment of capacitive attenuation of the voltage noise at high frequencies, the equivalent circuit diagram is shown as Figure 4.6b. The voltage noise at the input end of the pre-amplifier is:

$$\tilde{v}^2 = v_{na}^2 + \frac{i_s^2 R_s^2}{1 + (RC_p\omega)^2} \tag{4.3}$$

where i_s is the noise of the source current, R_s is the (possibly bias-dependent) differential resistance of the sample, C_p is the parasitic capacitance to the ground in the system, and v_{na} is the input voltage noise of the pre-amplifier. After the amplification gain A, the voltage noise becomes $A(v_{na}^2 + \frac{i_s^2 R_s^2}{1+(RC_p\omega)^2})$. An ideal cross-correlation would eliminate the input voltage noise from the pre-amplifiers and the final expression for the measured power spectral density is:

$$\tilde{S}_V(\omega) = \frac{AS_V}{1 + (RC_p\omega)^2} \tag{4.4}$$

where $S_V = i_s^2 R_s^2$ is the intensity of the intrinsic voltage noise.

4.5 Shot noise calibration

The true current noise is very small in our measurements, usually on the order of 10^{-25} A^2/Hz. The signal after the amplifier chain is linearly proportional to the intrinsic noise with some extra background from the amplifier or system. With proper calibration, we can restore the true value of the noise from the magnitude of our measured signal.

4.5.1 RF noise setup calibration

The RF shot noise calibration is based on the shot noise measurement in a vacuum tube. The current noise from a vacuum tube is a classic shot noise with $S_I = 2eI$. By measuring the noise signal from a vacuum tube, we can effectively know the calibration coefficient of the band-pass amplifier chain's total gain and apply the calibration coefficient to other shot noise measurement results. Figure 4.7 shows the measured shot noise reading vs the average current from the vacuum tube that generated from LED illumination.

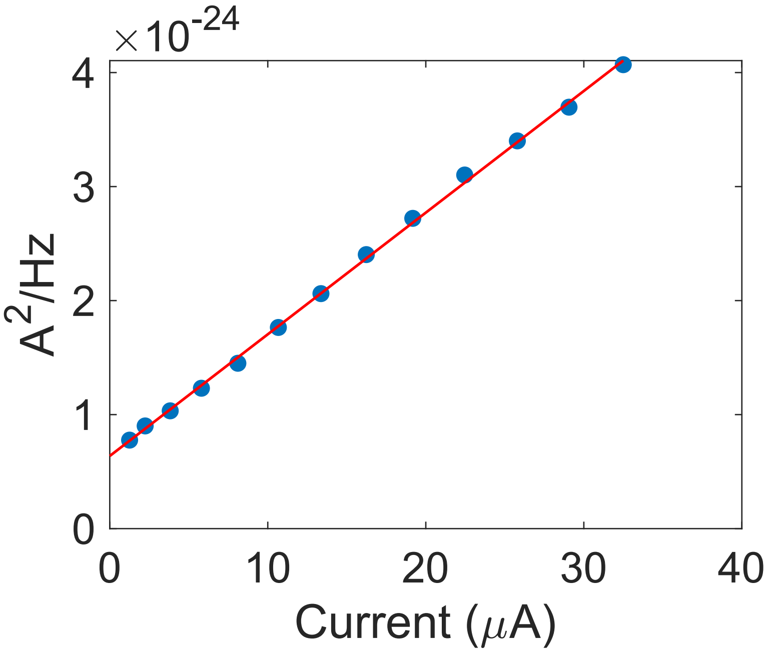

Figure 4.7 : Shot noise measurement in a vacuum tube.

To examine the calibration, we then measured the shot noise in a commercial diode MRD 500. The photocurrent of a photodiode is also Poissonian, and the power spectral density is $\sim 2eI$ as well. As shown in Figure 4.8, we measured the current noise of the diode at various reverse bias. The Fano Factor increase gradually as the reverse bias increases and saturates at above 0.95. This result indicates the calibration coefficient from the vacuum tube is very accurate.

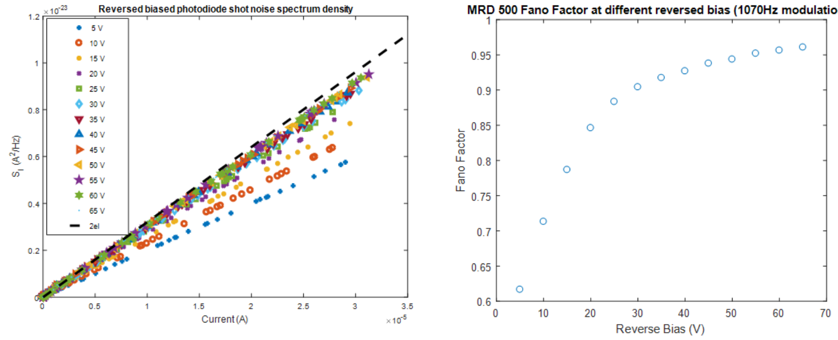

Figure 4.8 : Shot noise measurement in a photodiode after calibration.

4.5.2 Low frequency noise setup calibration

Similar to shot noise, J-N voltage noise is white noise, with PSD $S_V = 4k_BTR$, where R is the Ohmic resistance. Thus the J-N noise can be applied to calibrate the actual noise value. Eq. 4.4 gives an explicit expression for the spectral density of voltage noise power and can be used to fit the measured spectrum. Figure 4.9 shows an example spectrum of J-N noise from a fixed 2.17 kΩ resistor at T = 300 K. The decay of the measured S_V with increasing frequency is caused by the parasitic capacitance, C_p. The S_V data could be well fitted by the Eq. 4.4; see Figure 4.9a, in which the blue dots are the measured spectrum, and the red dashed line is the fit. There are a few spikes in the spectrum, which come from instrument pickup of extrinsic environmental signals that difficult to avoid. A robust fitting algorithm [99] is used to minimize the contributions of those outliers and fit the underlying spectrum. With the same device at fixed temperature, the fitted C_p is almost constant at different biases. The parasitic capacitance extracted from the overall fitting measurements of all devices is 300±100 pF, which is reasonable considering the input capacitance of the pre-amplifier and the parasitic capacitance in the transmission line. The variance comes primarily from variation amongst devices in wiring or bonding.

The linear dependences of the PSD of J-N noise on the resistance R and temperature T are verified in our experiments. Figure 4.9b shows the PSD of J-N voltage noise versus the resistance at 300 K. The linear relationship holds within a large resistance range, from 10 Ω to 30 kΩ. Smaller resistors would make the J-N signal-to-noise ratio too small to be accurately resolved, and larger resistances affect the voltage amplifier's gain and amplifier noise properties. This simple J-N linear dependence provides a calibration reference to our system. Similarly, the J-N linear dependence on temperature is also observed from 300 K down to 5 K (see Figure 4.9c). A small deviation is observed at the lowest temperatures, for which the sample's real temperature might be slightly different from the set temperature of the cryo-station.

For a macroscopic diffusive conductor at a constant temperature, the J-N noise should not depend on the applied d.c. voltage or current; this is also verified in our system. We applied current up to ±20 μA to a fixed metal film resistor and found that the noise spectral densities are always consistent with theoretical expectations. This verifies that the current and voltage sources are clean and show that any bias dependence of the noise originates from the samples, and not from the measurement system.

4.6 Summary

In this chapter, we overview the main experimental techniques used in the research topics. The cryogenic systems provide the nobs of temperature and field for the study of unconventional materials' response at different conditions. To fabricate the device

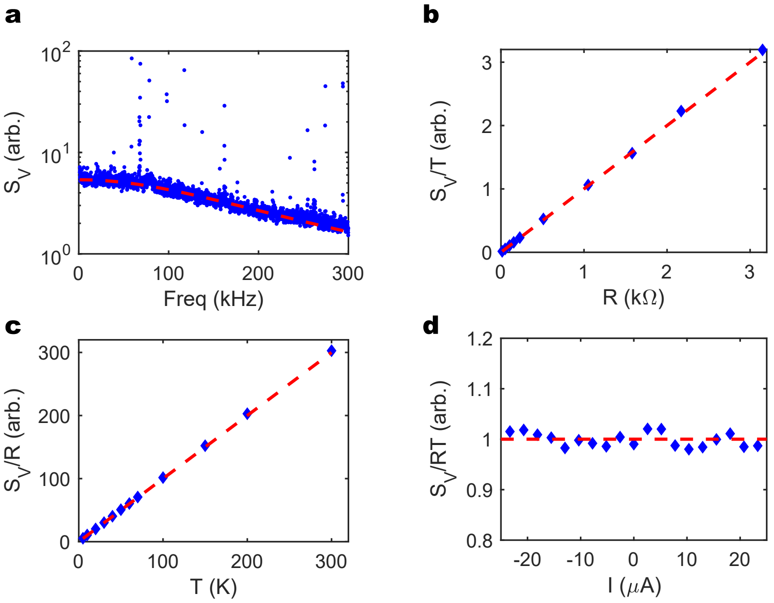

Figure 4.9 : Low frequency noise calibration. **a**, The PSD of the JN voltage noise in a 2.17 kΩ resistor at T = 300 K, measured by the cross-correlation method. The red line is a fit based on the $R_S C_P$ model. **b**, The J-N voltage noise of various resistors at 300 K. The voltage noise S_V has a simple linear dependence on the resistance of the resistor that is used as a calibration reference. **c**, The J-N noise is also linearly dependent on temperature for a fixed resistor (2.17 kΩ). **d**, For a fixed resistor (2.17 kΩ), the J-N noise is independent of the bias current, as expected for a macroscopic diffusive conductor.

for our study, we used lithography, evaporation, dry etching techniques, etc to obtain micro/nanoscaled materials and attach electric contacts to the materials. Then, with the device, we performed many measurements to study the electronic behavior of the material, such as the conductance dependence versus temperature, field and bias. At last, we introduced the two commonly used shot noise measurement techniques in our lab and explained the details about the setup and our calibration procedures. All those experimental setups and techniques are the key steps in the path to our final target, the measurement of shot noise in strongly correlated materials.

Chapter 5

hBN-based tunnel junctions

High-quality Au/hBN/Au tunnel devices are fabricated using transferred atomically thin hexagonal boron nitride as the tunneling barrier. All tunnel junctions show tunneling resistance on the order of several $k\Omega/\mu m^2$. Ohmic I-V curves at small bias with no signs of resonances indicate the sparsity of defects. Tunneling current shot noise is measured in these devices, and the excess shot noise shows consistency with theoretical expectations. These results show that atomically thin hBN is an excellent tunnel barrier, especially for the study of shot noise properties, and this can enable the study of the tunneling density of states and shot noise spectroscopy in more complex systems. This chapter is adapted partially from Panpan Zhou *et al*, “Electron pairing in the pseudogap state revealed by shot noise in copper oxide junctions” [100]) and Panpan Zhou *et al*, “Shot noise detection in hBN-based tunnel junctions” [101].

5.1 Hexagonal Boron Nitride

Hexagonal boron nitride (hBN) is a chemical compound that has a layered structure similar to the graphene lattice. As Fig 5.1 shows, the lattice is alternately arranged by B atoms and N atoms in a 2-dimensional plane forming a honeycomb structure. Within the plane, the N atom and B atom are combined by a strong σ bond, whereas the interlayer coupling is through weak van der Waals forces. The interlayer spacing of hBN is about 0.33 nm, which is very similar to graphene. In the c-axis direction of the hBN crystal, the small van der Waals force and large interlayer spacing make the interlayers slide easily.

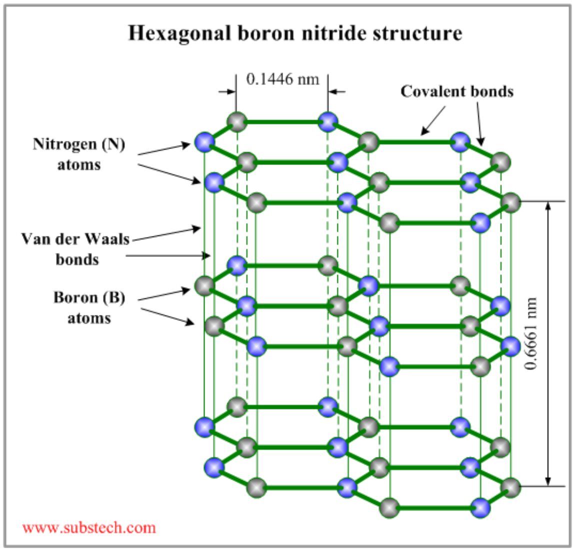

Figure 5.1 : The atomic structure of hexagonal Boron Nitride

Although hBN is very similar to graphene in structure, their electrical properties are dramatically different. It has a wide bandgap about 5.9 eV with a dielectric constant $\epsilon = 5.06$ [102] and a breakdown electric field strength of about 0.7 Vnm^{-1}. It also has very high-temperature stability as well as high thermal conductivity. All those properties make hBN a great insulating material for tunnel barrier or gating.

5.2 2D material transfer technique

The 2D materials have drawn a great amount of attention soon after the discovery of graphene and the appreciation of its unique electronic properties [103]. Many studies focused on the 2D materials, and recently more and more 2D materials have been found such as transition metal dichalcogenides (TMD) [104], black phosphorous [105], iron-based superconductors [106], etc. These new materials open opportunities for next generation of flexible and transparent electronic and optoelectronic devices.

5.2.1 Mechanical exfoliation

Usually, the 2D materials are in bulk crystal form. Obtaining these materials in atomic thickness and stacking the layers without introducing contamination and defects was a difficult task that impeded the development of the research on 2D materials. Mechanical exfoliation method and chemical vapor deposition (CVD) method are widely used to achieve very thin layered 2D materials.

The mechanical exfoliation process is described as the following steps:

- Gently place a few 2D material flakes in the middle of a 2-inch piece of Scotch tape.
- Repeat folding and unfolding the tape, and every time stick the tape on top of the 2D material flakes. It is better to fold over the remaining exposed take to prevent the samples from contacting with each other.
- Adhere the sticky side of the tape that has 2D material to some clean and cleaved 300 nm Si/ SiO_2 wafer. Press the tape to ensure that there are no

bubbles between the tape and wafer.

- Slowly separate the tape and the wafer with an angle around 180°.
- Examine the exfoliated 2D material on a silicon wafer under an optical microscope with polarized light to identify thin flakes.

5.2.2 Wet Transfer

Transferring and stacking 2D materials are the key techniques for assembling electronic devices. The wet transfer method is one of the earliest methods for transfer 2D flakes from Si/SiO_2 substrate to other substrates such as SiO_2, quartz, sapphire or other surfaces [107].

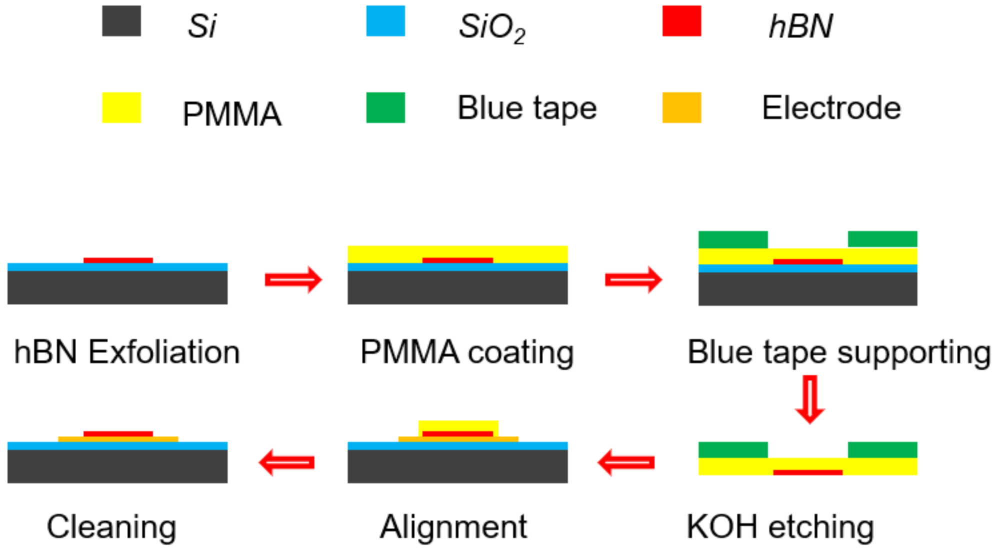

Figure 5.2 : Wet transfer process of an exfoliated hBN flake to another substrate with some pre-made patterns.

To begin with, PMMA 950C4 (4% in Chloroform) is spin-coated at 3000 rpm for 1 min on the substrate that already has target flakes to be transferred. Then the chip is baked at 180° for 30min. After that, a blue tape (NITTO tape) with a window hole about 2×2 mm aimed at the target flake is placed on top of PMMA. Then the whole assembled substrate is soaked in 1M KOH solution for 2 hours at 50° to etch the SiO_2 layer. After etching, the whole substrate-PMMA-tape unit would be cleaned in fresh deionized water (DI water) and the PMMA-tape pairs would float on the surface of the DI water. We can pick up the PMMA-tape pairs and align the target flake attached to the PMMA to the other substrate to finish the transfer using a micromanipulator stage and microscope.

5.2.3 Dry Transfer

The dry transfer method was first invented by Wang *et al* [108]. First, a Polypropylene carbonate (PPC) solution is made by dissolving PPC into anisole with a ratio of 15% PPC: 85% anisole. The PPC solution is spin-coated onto a 300-nm-thick SiO_2 to obtain a PPC film. Some graphene (or hBN) flakes are exfoliated onto the PPC film. Then, the Gr/PPC sheet is transferred onto a PDMS, and the prepared Gr/PPC/PDMS structure is attached to a glass slide. The whole unit forms a pick-up tool for the 2D flakes.

Under a microscope, the pick-up unit is aligned to the candidate 2D flake on SiO_2/Si substrate by adjusting the Gr flake position and the candidate 2D flake position to make gentle contact at room temperature. Warming up the state to 70° while the flakes are kept in contact. After that, we gently separate the pick-up unit from the SiO_2/Si substrate, and the target 2D material is picked up.

To transfer the target 2D material flake, the target/Gr/PPC/PDMS structure is aligned to the position where the target flake should land. Then, gently contact the target to the substrate and heat the stage to above 90°. The PPC film is melted during the heating, and the target/Gr flake is transferred to the right position. After cleaning the surface with Acetone/IPA, the dry transfer is done. During this process, the top and bottom surface of the target 2D material flake are always protected and never touch any wet chemicals, so this method is in general cleaner than the wet transfer method and has become the mainstream of 2D material transferring.

5.3 Au/hBN/Au tunnel junction fabrication

To fabricate the device, 10 μm by 100 μm Ti/Au electrodes were pre-patterned every 50 μm on a SiO_2/Si wafer. Then, hBN crystals (provided by our collaborators K. Watanabe and T. Taniguchi's group at NIMS, Tsukuba, Japan) were mechanically exfoliated on a clean 300 nm SiO_2/Si wafer. Thin hBN flakes have very low optical contrast, which makes them very difficult to identify. However, with the differential interference contrast microscopy, the thin hBN flakes can be found (Fig. 5.3a). The hBN flake is then transferred to the pre-patterned Au electrodes using the previously described wet transfer method (Fig. 5.3b). As the bottom Au electrodes are dense enough and cover a relatively large area, the thin hBN flakes could land on several electrodes without too much alignment difficulty.

After the hBN transferring, the chip is annealed in forming gas (25% H_2 75% Ar)

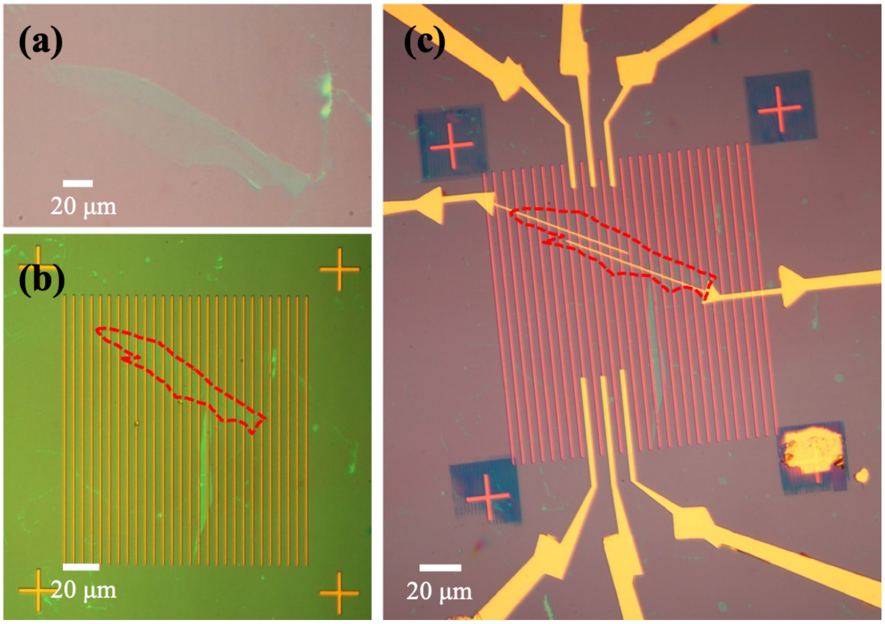

Figure 5.3 : hBN tunnel junction fabrication process. **a**, Monolayer hBN flake on 300 nm silicon oxide wafer. The image is taken using Olympus BX60M microscope. **b**, Transferred hBN flake on bottom Au electrodes. The image is taken with a green filter to improve the contrast. **c**, Finished junction device with both top and bottom Au electrodes.

at 250° for 2.5h to clean polymer residues involved in the transfer procedures. The top Ti/Au electrodes are then patterned by e-beam lithography. All junctions are about $1 \times 1 \mu m$ in dimension, as shown in Figure 5.3c.

5.4 Conductance measurement

The zero-bias resistance and differential conductance measurements were taken using a two-terminal wiring scheme in the PPMS. From room temperature down to cryogenic temperature 2 K, those tunnel devices exhibit a very weak insulating temperature dependence, which comes from the Fermi-Dirac distribution the free electrons in Au electrodes. At lower temperatures, there are fewer free electrons with high energies.

The tunneling current I and differential conductance dI/dV were measured simultaneously by applying a voltage excitation ($V_{dc} + V_{ac}$, where $V_{ac} = 1mV$ at frequency 300-500 Hz). For all the monolayer hBN tunnel junctions, the tunnel resistance ranges from 1 $k\Omega$ to 7 $k\Omega$, which agrees with the resistivity from previous studies on hBN based tunnel devices. The corresponding I-V curves in Figure 5.4a show an ohmic dependence at DC bias within 100 mV and the slope of the I-V curves almost does not change with temperature, which indicates the high quality and low defects of these tunnel junctions. The detailed features of the I-V curve slope can be revealed by the dI/dV measurement in Figure 5.4b. The dI/dV features vary from device to device, which might be caused by different defect types or residues at different spots of the hBN layer. The conductance variation of these tunnel junctions is less than 10% in the measurement bias range.

5.5 Inelastic features

The inelastic tunneling features have been reported in hBN-based tunnel junctions [109, 110]. Previous studies have been limited by the defects in the hBN tunneling layer. Here we measured the d^2I/dV^2 in Au/hBN/Au tunnel junction, where we did not observe the defects mediated tunneling effects. As there is no graphene involved, the inelastic features are limited to the hBN phonon-assisted tunneling process. As Figure 5.5 shows, clear inelastic tunneling features are found at temperatures below 10K. Different from previous results, features from defects mediated tunneling are not

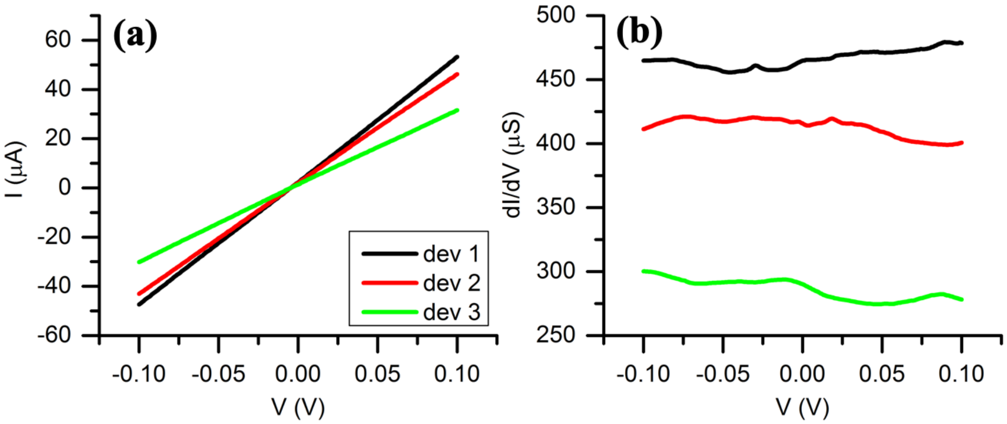

Figure 5.4 : Conductance properties of hBN devices. **a**, I-V curve of three different devices. **b**, dI/dV curve of the corresponding junction devices.

observed in our Au/hBN/Au device. This suggests the low defect rates of the hBN barrier in our devices.

Table 5.1 : Experimental and calculated phonon energies (in meV) at the Γ point. Adapted from ref [20].

Symmetry	Experiment	Theory
E_{2g}	6.5	6.5
B_{1g}(ZA)	silent	15.0
A_{2u}	97.1	92.6
B_{1g}(ZO)	silent	100.4
E_{2g}	169.4, 169.9, 169.1	171.0
E_{1u}(TO)	169.5	170.9
E_{1u}(LO)	199.6	199.7

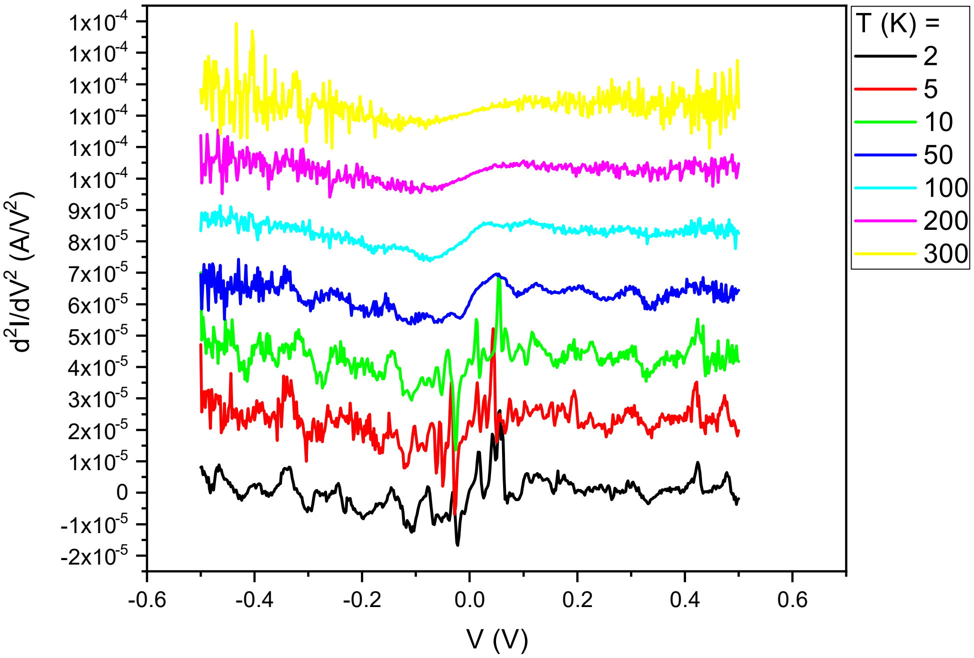

Figure 5.5 : Inelastic features in the Au/hBN/Au tunnel junction.

Although there is no rich experimental data on monolayer or bilayer hBN phonon modes, the phonon dispersion relations of bulk hexagonal boron nitride have been reported from inelastic x-ray scattering measurements and analyzed by *abinitio* calculations [20]. The experimental and calculated phonon energies are listed in Table 5.1. In our tunneling d^2I/dV^2 measurement, we observed repeatable features in 0-100 meV range, which are possible evidence of E_{2g}, B_{1g} and A_{2u} phonon modes of thin hBN.

5.6 Shot noise measurement

Tunneling shot noise was detected using the RF shot noise measurement method described in Chapter 3. Evolution of shot noise with temperature has a well-known form:

$$\frac{S_I}{4k_BTG} = \frac{eV}{2k_BT} coth(\frac{eV}{2k_BT}) \tag{5.1}$$

In the limit $\frac{eV}{2k_BT} \gg 1$, there will be a simple relation $\frac{S_I}{4k_BTG} \sim \frac{eV}{2k_BT}$. At zero bias, only thermal fluctuation term $4k_BTG$ should exist in the system. Here, the excess shot noise $S_{ext} = S_I(V) - S_I(V = 0) = 2eVGcoth(\frac{eV}{2k_BT}) - 4k_BTG$ is measured as a function of applied voltage V.

First, the temperature dependence was studied by measuring the shot noise from room temperature down to 5 K at various temperatures. It is found that the shape of the excess shot agrees very well with the above theory prediction, see Figure 5.6a. However, the noise magnitude is smaller than the expected value, which is a result of attenuation effect from cables and connectors. By fitting a linear factor A to the equation $S_{exc} = A(2eVGcoth(\frac{eV}{2k_BT}) - 4k_BTG)$, the RF system's transmission efficiency A can be resolved. As figure 5.6b shows, from room temperature down to 5 K, the transmission efficiency A increases from 11.0% to 14.4%. The efficiency difference may come from the capacitive coupling with the substrate. At higher temperatures, the heavily doped Si substrate has more free carriers, thus the capacitive coupling with the system is stronger and contributes to more RF signal loss during the transmission.

As the efficiency difference is small throughout the temperature range, without compensation for the different losses at different temperatures, we can still plot all

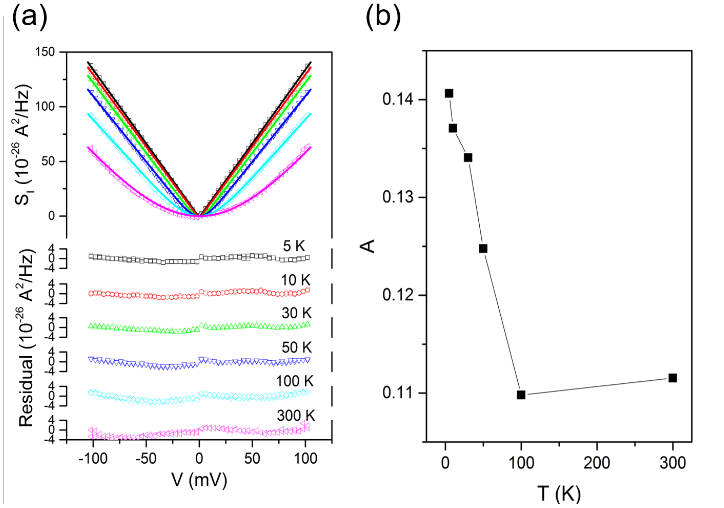

Figure 5.6 : Shot noise and the corresponding fitting in hBN tunnel junctions. **a**, The fitting to the shot noise intensity and the residual at different temperatures. **b**, Extracted transmission efficiencies at different temperatures.

the scaled dimensionless excess shot noise versus scaled dimensionless voltage bias together, which should all obey the relationship $\frac{S_I}{4k_BTG} \sim \frac{eV}{2k_BT}coth(\frac{eV}{2k_BT}) - 1$. This relationship is verified in several different devices and it is found that all devices have similar excess shot noise and voltage bias dependence, see figure 5.7. But the transmission efficiency varies between different devices and some of the devices have slightly asymmetrical behavior. The efficiency differences might come from detailed connection differences in the connectors and wires. The slight asymmetry is probably due to the thin Ti adhesion layer on the top electrode, which makes the real junction structure to be Au/hBN/TiAu. As the work function of Ti and Au are different, it is not surprising to see that asymmetry results.

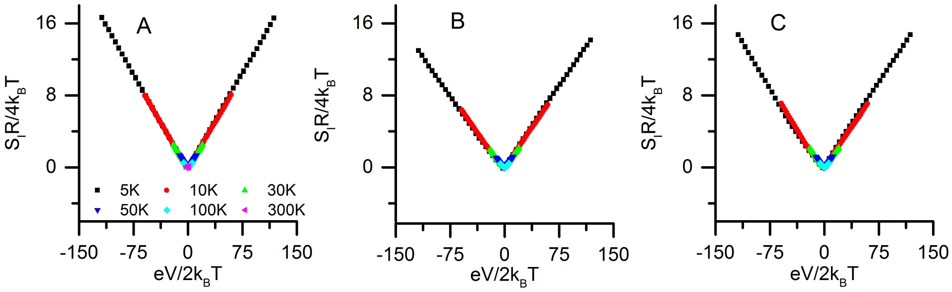

Figure 5.7 : Scaled shot noise of three different hBN tunneling devices.

5.7 Summary

In conclusion, we fabricated Au/hBN/Au tunnel junctions and studied the excess shot noise of the current. The measured shot noise has a good agreement with theory over a large temperature range, which indicates a great potential to be used for thermometry or noise calibration. Also, the clean shot noise results in Au/hBN/Au indicates that atomically thin hBN could be an ideal tunnel barrier for shot noise detection in other complicated systems, such as studying the quasi-particles in strongly correlated systems, or spin accumulation in spin Hall systems. The effective carrier charge or spin polarization could be identified by calibration from this result.

Chapter 6

LSCO/LCO/LSCO tunnel junctions

Tunnel junctions are valuable tools for electronic spectroscopy, with epitaxially grown structures minimizing the extrinsic effects of disorder. With controllable growth process, we can fabricate tunnel junctions with various unconventional materials, such as heavy fermions, high-temperature superconductors or Mott-insulator-transition materials. In this chapter, we report the fabrication and tunneling spectroscopy measurements in $La_{2-x}Sr_xCuO_4/La_2CuO_4/La_{2-x}Sr_xCuO_4$ structures grown along the c-axis via atomic layer-by-layer epitaxy and with various doping levels from underdoped to optimum doped. Above the superconducting transition T_c, these structures show the pseudogap, while below T_c of the LSCO layers the devices show superconductor/insulator/superconductor (SIS) response. Many trials were attempted to fit the differential conductance in those samples but only partial success was obtained in optimum doped devices. We also observed an inelastic tunneling feature at a bias of $\sim$ 80 mV, suppressed as T exceeds T_c. This chapter is adapted from a draft in prepare for submission, Panpan Zhou *et al.* "Tunneling spectroscopy of c-axis epitaxial cuprate junctions".

6.1 ALL-MBE technique

Molecular beam epitaxy (MBE) is an ultra-high vacuum technique for the deposition of thin films. With some extra monitoring tools that control the absolute deposition rate of each material, the growth can reach atomic layer accuracy. Atomic-layer-by-layer molecular beam epitaxy (ALL-MBE) technique has enabled synthesis of atomically smooth thin films or superlattices of cuprates and other complex oxides. In the system, the film growth was monitored in real-time by reflection high-energy electron diffraction (RHEED). The diffraction patterns provide information on the surface morphology and crystalline structure. The oscillations of the intensity of the specular reflection with time provide for a digital count of the number of deposited monolayers. Sufficient oxidation under high-vacuum conditions needed for MBE is accomplished using a source of pure ozone. After the growth, different annealing procedures help to ensure the uniformity of the film material to further improve the quality.

With state of the art ALL-MBE system at Brookhaven National Lab (Prof. Ivan Božović's group), it is possible to create copper oxide SIS c-axis junctions having atomically flat interfaces, with minimal disorder limited by the doping levels of the cuprate material [111]. Junctions have been demonstrated using $\mathrm{La}_{2-x}\mathrm{Sr}_x\mathrm{CuO}_4$ as the superconducting top and bottom electrodes, with the intervening tunnel barrier consisting of the undoped Mott insulating parent compound $\mathrm{La}_2\mathrm{CuO}_4$. The high-quality of these tri-layer structures has been demonstrated, showing that as little as one unit cell of LCO barrier is sufficient to inhibit superconducting current between LSCO source and drain. Inelastic tunneling spectroscopy in such junctions has shown signatures of quasiparticle coupling to phonon modes identified through Raman spectroscopy [112].

6.2 Sample fabrication

The LSCO/LCO/LSCO trilayer films were grown using the ALL-MBE system on $LaSrAlO_4$ (LSAO) substrates by our collaborators at Brookhaven National Lab. The tunneling devices were fabricated from the LSCO/LCO/LSCO films using the standard photolithography techniques. The detailed process is shown in Figure 6.1. After photolithography to define mesa locations, the film was milled down to the substrate with argon ions into 20 μm square mesas. A second lithography step defined circular tunnel junctions, with a second controlled ion milling to etch the surrounding material through the top LSCO layer and the middle LCO layer, to expose but not etch through the bottom LSCO layer. A thick layer of Al_2O_3 was evaporated to photolithographically defined areas to help isolate what will become the top and bottom contacts. Finally, Au is evaporated to make contact with top/bottom LSCO layers.

6.3 Device transmission electron microscopy characterization

The TEM characterization of the tri-layer film was performed by our collaborators Prof. Yimei Zhu and Dr. Myung-Geun Han at Brookhaven National Lab. TEM samples were prepared by a Focused Ion Beam (FEI Helios Nanolab) using 2.0 keV Ga^+ ion for final milling. A focused 0.5 kV Ar^+ ion beam (Nanomill, Fischione Instruments, Inc.) was used to remove FIB damaged layers at liquid nitrogen temperature. For HAADF STEM images, a JEOL ARM 200CF equipped with a cold field emission

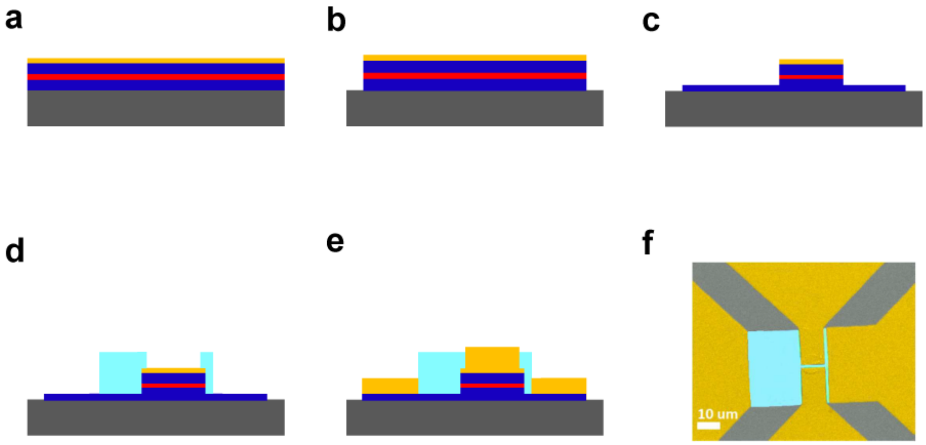

Figure 6.1 : Device fabrication process. **a**. LSCO/LCO/LSCO film is grown on top of LSCO substrate with a thin layer of in situ deposited Au covering the film. **b**. The film is etched into bars defined photolithographically. This is a deep etch all the way into the substrate. **c**. A second dry etch step removes part of the top LSCO and middle LCO layers, and stops in the middle of the bottom LSCO layer which gets exposed in these areas, creating 10-20 μm mesas. **d**. A thick layer of Al_2O_3 (100 nm) is evaporated to isolate the future top Au contact (150 nm) and bottom Au contacts, to avoid parallel conduction paths. **e**. Contacts are defined lithographically and Au is evaporated to make contact with top and bottom LSCO layers. **f**. A false-colored SEM image of the device.

source and two aberration-correctors at the Brookhaven National Laboratory was used with 200 keV electrons and the collection angles in the range of 67 to 275 mrad. For EELS spectrum imaging, La L edges (832 eV) were recorded with 0.1 eV/channel energy dispersion. The EELS acquisition time was 0.05 s/pixel with 0.039 nm pixel size. The convergent and collection semi-angles were 20 and 10.42 mrad, respectively. For Sr elemental mapping, a FEI Talos F200X equipped with a four-quadrant 0.9-sr energy dispersive X-ray spectrometer operated at 200 keV was used. Sr L (1.806 keV) signals were collected with an acquisition time of $\sim$ 3 mins with 0.6 nm pixel size. To enhance signal-to-noise ratio, principal component analysis was performed. Line profiles of La L edges were obtained after background and baseline subtractions. The

1.5 unit cell undoped LCO layer in the SIS architecture was not resolved in HAADF, EELS mapping using Sr L edge (1940 eV) and EDX mapping of the La edge due to low concentration (8 %) difference of Sr, but clearly visible in EDX mapping of Sr edge and EELS mapping of La edge.

The schematic of the fabricated devices and the cross-section of the tri-layer film is shown in Figure 6.2 **a**-**b**. The LCO layer thickness is precisely controlled to be 3 monolayers, 2.0 nm thick. Figure 6.2 **c** shows a cross-section of an actual device imaged using a scanning transmission electron microscope (STEM). Energy dispersive x-ray spectroscopy and atomic-resolution electron-energy-loss spectroscopy were used for La, Sr, and Cu elemental mapping in Figure 6.2 **d**. The micrographs demonstrate remarkable crystalline perfection and atomically sharp interfaces, consistent with previous extensive STEM studies of cuprate films synthesized by ALL-MBE. Atomic-force microscopy also shows that the surfaces are atomically smooth, except for occasional steps due to substrate miscut.

6.4 Transport properties

The device electrical properties were measured with standard lock-in amplifier techniques, with the measurements were performed from room temperature down to 2 K in a variable temperature cryostat, and down to 20 mK in a separate measurement setup on a dilution refrigerator by collaborators at University of Connecticut. For each doping, we performed differential conductance measurements on multiple devices over a broad range of voltage bias and temperatures.

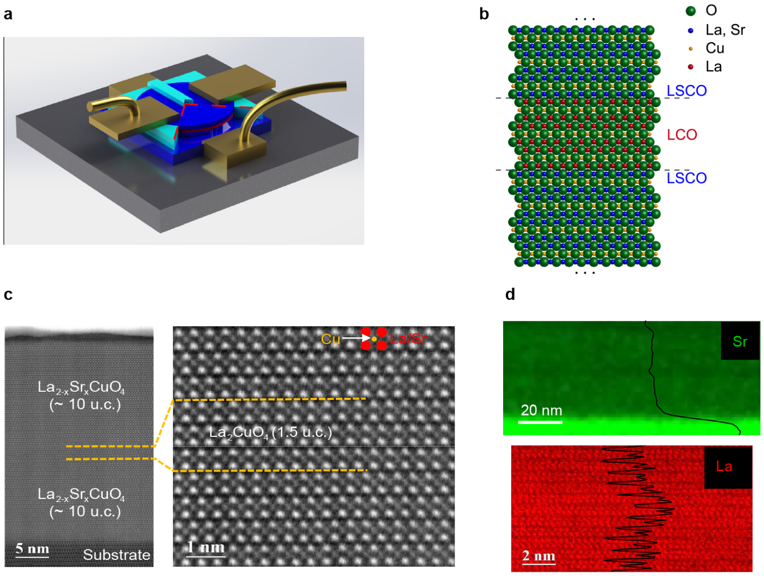

Figure 6.2 : LSCO/LCO/LSCO tunneling structures synthesized by ALL-MBE. **a**, Device schematic: photolithography and etching are used to prepare vertical tunneling devices, 10 or 20 μm in diameter. **b**, Film schematic: a tunneling barrier consisting of three molecular layers (1.5 unit cells (u.c.)) of undoped LCO is sandwiched between the bottom and the top superconducting LSCO electrodes. **c**, A high-resolution cross-section image of the actual device obtained by scanning transmission electron microscope (STEM) and high-angle annular darkfield imaging (HAADF). **d**, Elemental maps of Sr (green) and La (red) obtained by atomic-resolution energy dispersive x-ray spectroscopy (EDS) and electron-energy-loss spectroscopy (HREELS), respectively, with overlaid white lines showing averaged line profiles. Yellow dashed lines indicate the boundaries of the undoped LCO layers.

6.4.1 Temperature dependence

On each chip, multiple Hall bar devices were also fabricated alongside the tunnel junctions. These Hall bar devices were used for measuring T_c of both the bottom and top LSCO layers at each doping. Devices with doping level x =0.10, 0.12, 0.14 and 0.15 (close to optimum doping) were measured over a broad range of bias and temperatures in this letter. The superconducting transition temperatures of the corresponding dopings are 28 K, 34 K, 37 K and 38 K, which is in good agreement with previous reports on ALL-MBE grown LSCO film samples [113]. Figure 6.3**a** shows the R-T measurement of a Hall bar structure in the 0.15 doped film. Mutual inductance measurements on the as-grown multilayer films done by our collaborators showed that the transition temperatures of the bottom and top LSCO layers were identical to within the width of the transition.

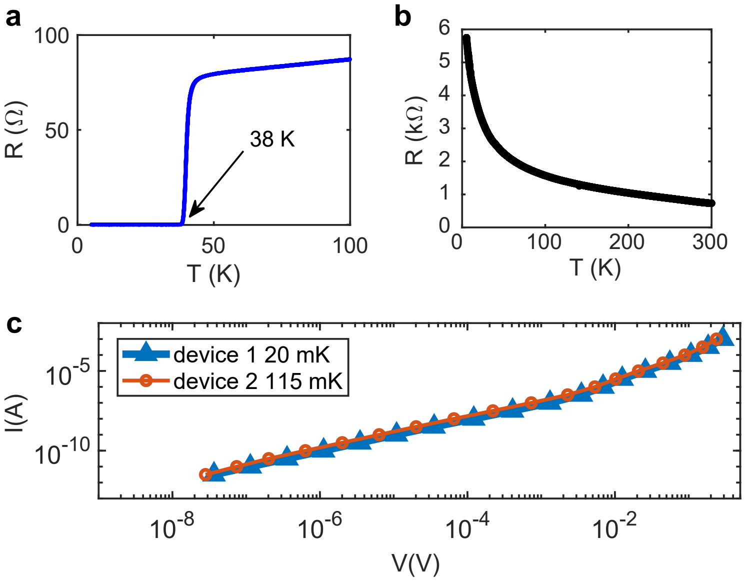

Figure 6.3 : Temperature dependence of the LSCO/LCO/LSCO film and junctions. **a**, R–T measurement on the Hall bar device fabricated in this film shows the superconducting transition temperature Tc = 38 K. **b**, R–T measurement on the tunnel junction shows an insulating temperature dependence. **c**, log–log plot of the I–V characteristics of two x = 0.15 tunnel junction devices, demonstrating device-to-device reproducibility and lack of any supercurrent down to pA levels at dilution refrigerator temperatures. This measurement was done in a dilution refrigerator by our collaborator Prof. Ilya Sochnikov at University of Connecticut.

Prior studies of ALL-MBE grown LSCO/LCO/LSCO heterostructures have focused on this as a primary technical issue [111]. There it was shown that even a 1 UC

(1.3 nm) thick LCO barrier had no pinholes and was insulating. To be on the safe side, the devices for the present work had barriers 50% thicker (1.5 UC = 2 nm). These are likewise insulating, with no sign of pin-holes that would short the junctions. As shown in Figure6.3**b**, the tunnel junctions all have insulating temperature-dependent R-T curve down to the lowest temperature of our measurement range (20 mK), indicating that the device conductance is dominated by the insulating LCO layer. In particular, the lack of any measurable supercurrent down to dilution refrigerator temperatures and picoamp resolution in all devices examined argues that there are no true pinholes, as shown in Figure 6.3**c**. True pinholes would likely support proximity-induced supercurrent.

6.4.2 Differential conductance

For all temperatures, the differential conductance has an overall V-shaped background in the normal state that extends to the superconducting temperature regime. At temperatures above the transition temperature T_c of each film, this pseudogap is readily apparent. There is an overall asymmetry to dI/dV vs. V_{dc}, with the conductance being higher at the polarity such that electrons are driven from the bottom LSCO layer to the top. This broken symmetry is consistent with the variation in epitaxial strain away from the substrate, and the polar nature of the material [114]. At temperatures below T_c, the conductance is very nonlinear and exhibits a suppression at zero bias, as expected for a SIS junction. The zero-bias conductance suppression becomes progressively sharper as the doping is varied from near-optimal $x = 0.15$ to the more underdoped $x = 0.10$. For all devices, the differential conductance at zero bias dI/dV ($V_{dc} = 0$) saturates at low temperatures, rather than approaching zero as T → 0. This saturation implies the presence of a large population of tunneling unpaired quasiparticles in these structures even as T → 0, even with the high degree of structural perfection in these ALL-MBE structures.

Figure 6.4 shows the differential conductance tunneling spectra of representative devices from the four dopings. The suppression of the zero-bias conductance below T_c is readily apparent, as is the residual zero-bias conductance. We consider the functional form of these tunneling spectra in light of the ALL-MBE structures. The naive expectation for a structurally clean, large-area tunnel junction is conservation of crystal momentum in the a-b plane, $\mathbf{k}_{ab}$. A calculation based on a d-wave BCS order parameter and transverse $\mathbf{k}$ conservation, for planar tunneling of perfectly 2D quasiparticles, predicts a negative differential conductance region, as does an analogous calculation for a s-wave BCS [62], because of the constraint of momentum conservation and the $\frac{1}{\sqrt{E^2-\Delta^2}}$ form of the BCS density of states that appears squared in the calculation of the tunneling current as $V_{dc} \to 0$. This is clearly in disagreement with the experimental data. Instead, the measured differential conductance is more consistent with models that ignore conservation of transverse $\mathbf{k}$, and strongly resembles a spatial average of localized non-k-conserving SIS tunneling [115]. Effectively local tunneling could result from averaging over electronic spatial inhomogeneity, or sufficient nonzero antinodal dispersion in k_z.

6.4.3 Normalized conductance

Figure 6.5 shows normalized tunneling spectra for the four dopings, (dI/dV (V,T))/(dI/dV (V,T = 50 K)), a rough attempt to focus on the superconducting gap aspects of SIS

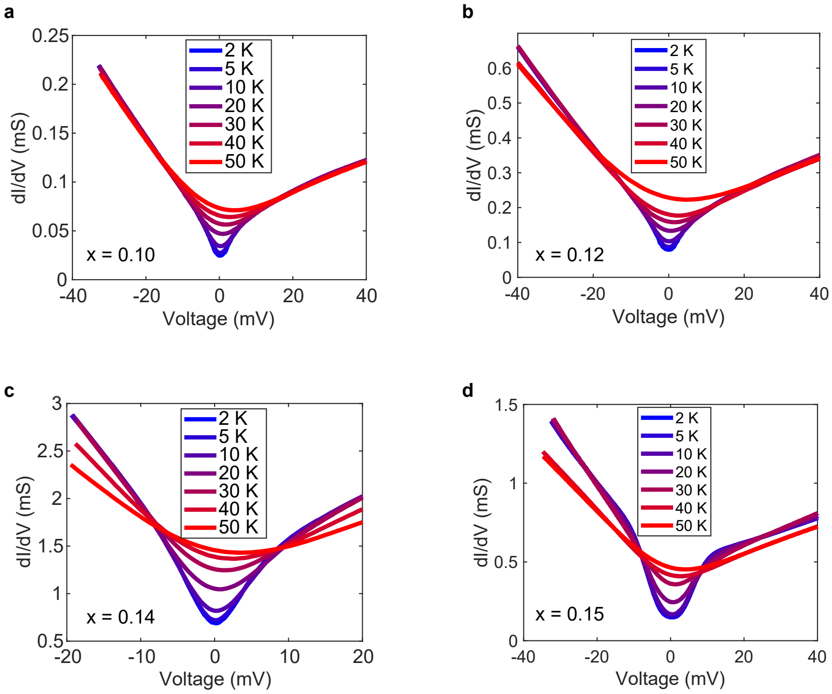

Figure 6.4 : Differential conductance dI/dV as a function of V_{dc} for the dopings x = 0.10, 0.12, 0.14, and 0.15 in panels (**a-d**), respectively. The bias asymmetry correlates with the structure of the junctions, while the broader V-shape is a manifestation of the pseudogap.

tunneling while minimizing the role of the higher energy pseudogap and inherent device asymmetry. Our collaborators T. C. Wu and Prof. Matthew Foster at Rice University have attempted a more phenomenological approach by fitting a Dynes parameter-based d-wave BCS-type [116] density of states for optimal doping:

$$N(\omega) = N_0 Re \left\langle \left[\frac{\omega + i\Gamma(\omega, T)}{\sqrt{(\omega + i\Gamma(\omega, T))^2 - \Delta^2 cos^2(2\theta)}} \right] \right\rangle_\theta \tag{6.1}$$

Here $\Gamma(\omega, T) = \alpha(T)\omega + \beta(T)$ is an effective lifetime broadening, N_0 is an overall normalization, ω is energy, Δ is the magnitude of the d-wave gap, and 2θ describes the angular dependence of the gap within the a-b plane. This empirical form for $\Gamma(\omega, T)$ has been employed in interpreting STM tunneling spectra in Cuprates [117, 118, 119].

Strictly speaking, the addition of $\Gamma(\omega, T)$ is a deviation from standard BCS theory. The expected differential conductance assuming local tunneling is then:

$$\frac{dI}{dV} = A\frac{d}{dV}\int N(\omega+eV)N(\omega)\left[f(\omega)-f(\omega+eV)\right]d\omega \tag{6.2}$$

where V is the dc bias voltage and f is the Fermi-Dirac distribution function. With the above equation, we can try to fit the differential conductance with the fitting parameters $\alpha(T)$, $\beta(T)$ and $\Delta(T)$ and the prefactor $A = 1$ accounts for normalization.

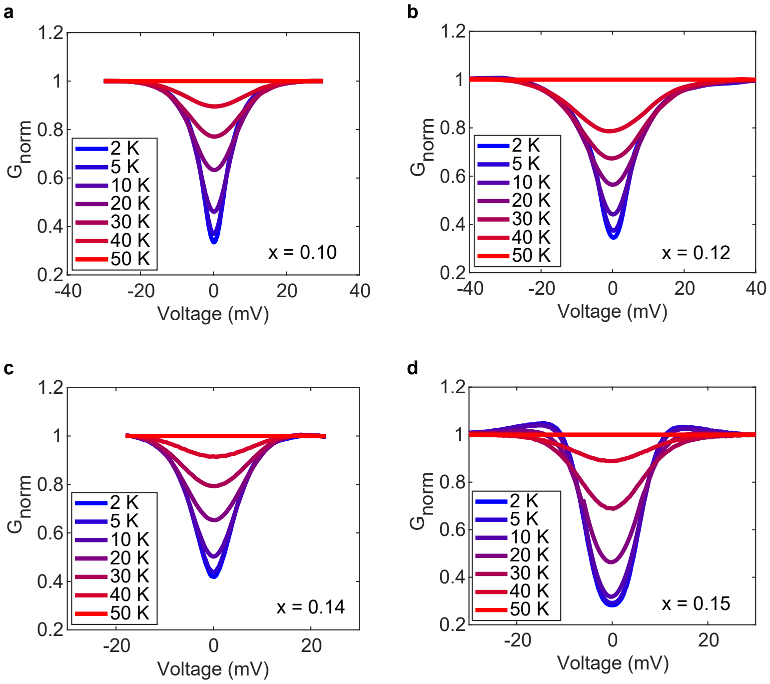

Figure 6.5 : Normalized differential conductance G_{norm} = (dI/dV)/(dI/dV (T = 50 K)), for the dopings x = 0.10, 0.12, 0.14, and 0.15 in panels (**a**-**d**), respectively. The fine solid line is a fit of the lowest temperature data.

The Dynes parameter essentially assumes an effective pair-breaking process. The model works relatively well for the $x = 0.15$ doped sample, as shown in Figure 6.6.

The temperature dependence of the fit parameters $\alpha(T)$, $\beta(T)$ and $\Delta(T)$ show that within this model, these devices act like Dynes superconductors. As T increases toward T_c, the gap seems to fill in due to an increasing Γ, rather closing due to a decreasing of Δ. This is consistent with observations made in photoemission experiments of other cuprates [120, 121]. $\alpha(T)$ has a weak temperature dependence and $\beta(T)$ has a quadratic temperature dependence, as the black dash line in Figure 6.6**b** indicates. The Γ broadening both suppresses coherence peaks and, through β, leads to residual T = 0 conductance, through a contribution to Γ proportional to ω. Fitting with this approach does not succeed in the underdoped samples. The primary difficulty is achieving a proper balance between the suppression of the coherence peaks and residual zero-bias conductivity as $T \to 0$. Also, the fitting is sensitive to the T-normalization procedure, which means that any temperature evolution of the pseudogap could distort the normalized data and affect the fitting results.

6.4.4 Inelastic features

The second derivative of the current signal, d^2I/dV^2, reveals inelastic tunneling features. Figure 6.7 shows inelastic tunneling analysis as a function of temperature for the various LSCO dopings. Numerical differentiation of the differential conductance, dI/dV , is quantitatively consistent with the directly measured lock-in second harmonic signal, d^2I/dV^2. For all the devices, there are broad inelastic features at energies between around 75 meV that become markedly weaker as T is increased above T_c. With increasing doping levels from 0.10 to 0.15, the inelastic features become less prominent. At higher biases exceeding 300 meV (not shown), the devices have instability issues and strong shot noise that affect the measurements, making it

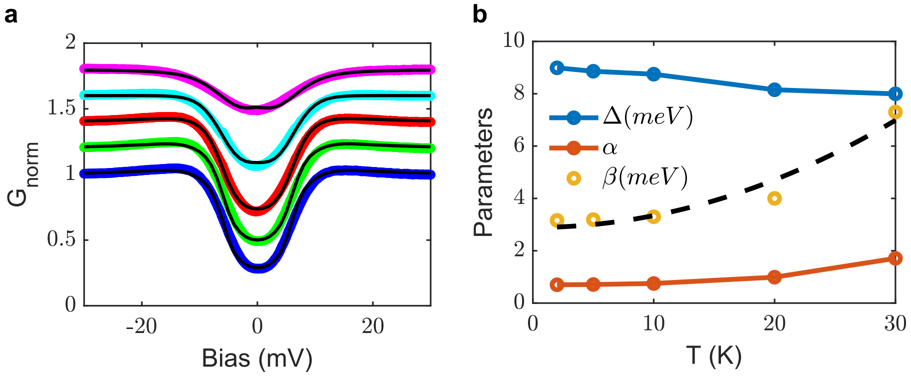

Figure 6.6 : Fitting to the normalized differential conductance and the corresponding fitting parameters at various temperatures below T_c. **a**, Normalized differential conductance for doping x = 0.15 at 2 K (blue), 5 K (green), 10 K (red), 20 K (cyan) and 30 K (magenta). The black lines are the fittings to the conductance at each temperature. Data is shifted by 0.2 vertically between each temperature. **b**, The fitting parameters Δ, α and β as a function of temperature. The fitting and analysis are done by our collaborators T. C. Wu and M. Foster at Rice University.

difficult to assess inelastic features at higher energies.

The present inelastic features are in a similar energy range to ARPES and neutron scattering results that show kinks and other fine features. This energy scale is larger than experimentally observed out-of-plane oxygen vibrations (~55 meV) known to couple strongly to the carriers [118, 122]. Other calculations show that this energy scale is close to that expected for B_{1g} and half-breathing modes in LCO [123]. Magnons are other bosonic modes also present at energy scales large compared to the superconducting gap, and the energy range of the observed inelastic features is compatible with prior studies showing a branch of magnons in LCO dispersing up as high as 400 meV [124]. Specifically, the magnon mode energy in the limit of zero in-plane momentum is close to 80 meV.

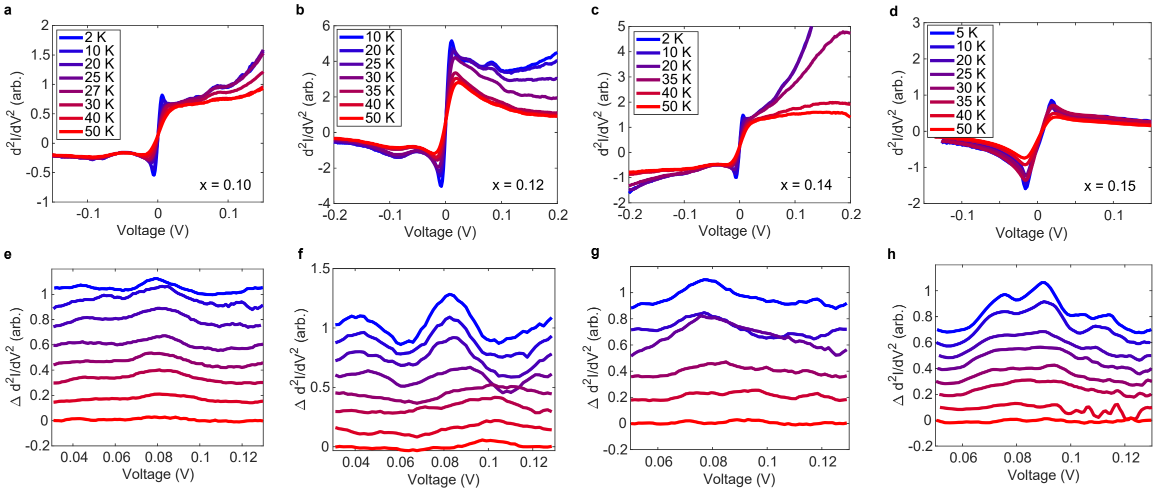

Figure 6.7 : Inelastic tunneling features in LSCO junctions. **a-d**, Inelastic spectra, d^2I/dV^2 as a function of bias for x = 0.10, 0.12, 0.14, and 0.15, respectively. The fine solid line is a fit of the lowest temperature data. **e-h**, Close-up views of the positive polarity part of the inelastic tunneling spectra, with a smooth polynomial background (obtained at 50 K) subtracted.

6.5 Summary

We have performed a systematic tunneling spectroscopy study of LSCO/LCO/LSCO tunneling devices from the underdoped limit to near-optimal doping, revealing several interesting features. Despite the high structural perfection inherent in epitaxially grown structures, the SIS tunneling spectra are best fit by a model of local tunneling rather than a model that includes conservation of transverse crystal momentum. Phenomenological analysis of the tunneling spectra requires a Dynes-modified d-wave BCS-like model to account for strong suppression of coherence peaks and large residual zero-bias conduction at T → 0, indicating a large contribution of unpaired quasiparticles to tunneling even far below T_c. This is coincident with maximal violation of the typical Ambegaokar-Baratoff relationship between I_c and R_N, given the complete suppression of I_c, even when shot noise measurements [100] indicate the presence of a pair contribution to the tunneling transport. The phenomenological model also shows that the spectra imply LSCO acts as a Dynes superconductor, with gap-filling through loss of global coherence rather than gap closure as T warms through T_c. Inelastic tunneling spectra reveal fine features in an energy range near known phonon modes as well as the energy scale of dispersing magnons in the LCO barrier. Further studies of such epitaxial junctions, particularly in the presence of large magnetic fields and different combinations of doping levels and barrier structures, should shed further light on the nature of the tunneling process and the type and role of relevant bosonic modes.

Chapter 7

Shot noise in LSCO/LCO/LSCO junctions

In this chapter, the shot noise in LSCO/LCO/LSCO tunnel junctions is studied. The result directly determines the charge of carriers as a function of temperature and bias and helps to resolve one of the most debated topics in high-temperature superconductivity, the pseudogap. It is found that the pseudogap phase also hosts pairs thus the shot noise is enhanced in this region. Also, at below transition temperature, there is also unexpected noise enhancement at bias level larger than the superconducting gap, which suggests that electron pairing may exist in a much broader range than traditional theoretical limitations. The content of this chapter is mostly adapted from Panpan Zhou *et al*, "Electron pairing in the pseudogap state revealed by shot noise in copper oxide junctions" [100].

7.1 Pseudogap phase in cuprate

The pseudogap has been detected in copper oxides and studied by many experimental probes, most directly by angle-resolved photoemission spectroscopy (ARPES) [125, 126, 127, 120] and tunneling [128, 129]. However, its microscopic origin and its relation to other anomalous normal state properties and to high-temperature superconductivity (HTS) have remained the subject of much speculation.

One candidate idea is that the pseudogap is a high-temperature precursor of the superconducting state. In this scenario, at T_c the global phase coherence is destroyed by thermal fluctuations, while preformed pairs exist well above T_c and up to some higher pairing temperature (which may not be sharply defined) [18, 86]. Indeed, ARPES, [125, 126, 127, 120] tunneling,[128, 129] and terahertz spectroscopy [19] data are consistent with superconducting fluctuations detectable up to 10-20 K above T_c. The range expands with the sensitivity of the probe; thus, the Nernst effect [82] and torque magnetometry [81] detect the signatures of vortices and fluctuating diamagnetism up to even higher temperatures. Note that in all copper oxides, the superfluid density is very low; the phase stiffness temperature is roughly the same as T_c, even at optimal doping, and hence, thermal phase fluctuations must be very large near T_c. Moreover, T_c has been found to scale with the superfluid density and appears to be kinematically controlled, [130] in line with strong-coupling theories of HTS.[131, 132] However, a direct and quantitative signature of hole pairing above T_c has remained elusive.

Another popular scenario is a “two-gap” picture in which the pseudogap is distinct from the superconducting gap and originates from some other instability competing with superconductivity.[18, 132] Candidates include charge-density waves, d-density waves, stripes, electronic nematicity (broken rotational symmetry in the electron fluid), etc. [18] Low-energy excitations out of such a state should be some collective modes, e.g., oscillations of the phase and amplitude of the order parameter (phasons and amplitudons).

Measuring the charge of mobile carriers in the pseudogap state could discriminate between these possibilities. A population of preformed pairs would manifest as an average effective charge q^* larger in magnitude than the electron charge e, while lack of well-defined current-carrying quasiparticles would appear as a suppressed effective charge below e. The most direct experimental probes of charge are the measurements of Aharonov-Bohm oscillations in nano-rings, Coulomb blockade in nanoscale “dots”, and shot noise in nanowires or tunnel junctions. The short inelastic mean-free-path of carriers in the copper oxides, in particular at temperatures above T_c, and the challenge of nanofabrication without damaging material properties, currently make the first three approaches extremely technically challenging. Measurement of shot noise in large-area planar tunnel junctions remains as the most feasible candidate to infer the charge of the carriers in bulk samples in the normal state.

7.2 Cross correlated noise spectrum

In this research, extremely high accuracy is required to obtain reliable effective charge information. Modulated radio frequency power detection method, although is a fast and robust noise detection way, has its problem in calibration. The cross-correlated noise detection scheme that introduced in Chapter 4 is more appropriate for precise noise detection tasks.

Based on the low frequency shot noise measurement method in Chapter 4, after cross-correlation, the measured noise power spectra density has the form:

$$\tilde{S_V}(\omega) = \frac{AS_V}{1 + (R_S C\omega)^2} \tag{7.1}$$

where A is the amplification gain, S_V is the intrinsic white shot noise power spectra density, R_S is the sample differential resistance and C is the system's effective capacitance.

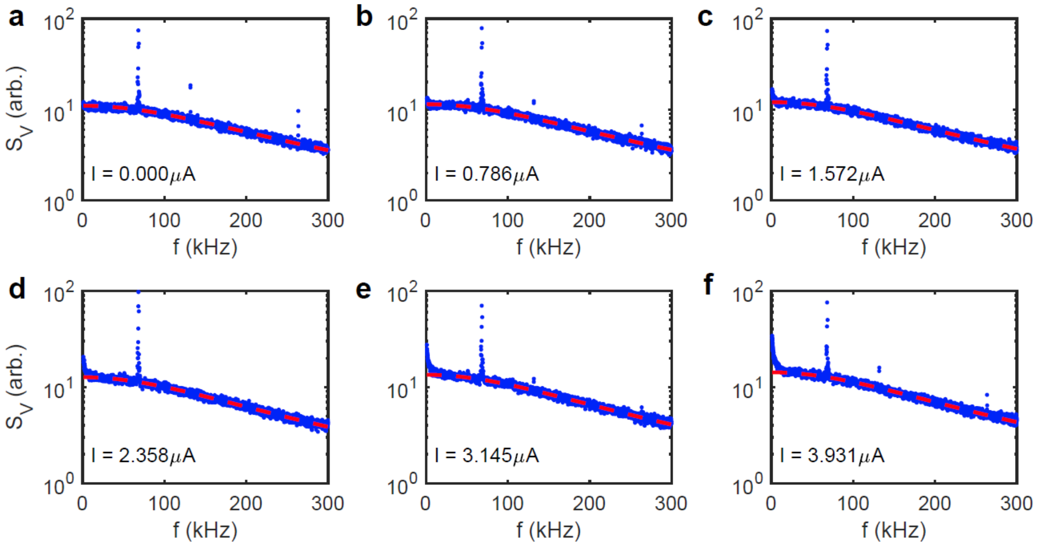

Figure 7.1 : Example spectra of an LSCO tunnel junction for x = 0.15, recorded at T = 50 K. The dc bias current is marked for each panel. The red dash line is fits based on the RC circuit model using the measured differential resistance R_S at each bias. The sharp spikes result from environmental pickup of specific frequencies. The fitting parameters are list in table 7.1.

At each temperature, the dc current bias across the LSCO junction is finely swept in increments of about 700 nA up to ±20 μA. The averaged cross-correlation spectrum is recorded at each bias and fits with the R_SC model equation (the red dashed lines in Fig 7.1.), inserting for R_S the measured differential resistance at a given bias. The spectral density of voltage noise power could be extracted from the fitting parameters, see example fitting parameter in Table 7.1. Together with the dI/dV measurements at the same bias conditions, the voltage noise is translated to the current shot noise by $S_I = S_V/(dV/dI)^2$. At high current or voltage bias, the $1/f$ noise becomes more

Table 7.1 : Example fitting parameters for the noise spectrum in Fig. 7.1.

Basic Current (μA)	S_V **(arb.)**	$2\pi R_S C_p (1/Hz)$	**dI/dV (S)**
0	9.55×10^{-8}	5.16×10^{-6}	4.17×10^{-4}
0.786	9.87×10^{-8}	4.93×10^{-6}	4.10×10^{-4}
1.572	1.06×10^{-7}	5.22×10^{-6}	4.06×10^{-4}
2.358	1.13×10^{-7}	5.07×10^{-6}	4.07×10^{-4}
3.145	1.22×10^{-7}	5.38×10^{-6}	4.12×10^{-4}
3.931	1.32×10^{-7}	5.08×10^{-6}	4.15×10^{-4}

noticeable, as seen in the low-frequency limit in Fig 7.1. Hence, in data analysis the fitting range is restricted to frequencies sufficiently high to mitigate any effects of $1/f$ contributions, as verified through consistency of the $R_S C$ model.

7.3 Comparison between measured noise and single electron tunneling expectation

Within the single-electron Poissonian tunneling approximation, the noise power spectral density at finite temperature T is expected to be $S_{I,e} = 2eIcoth(eV/2k_BT)$. This reduces to the Johnson-Nyquist noise in the zero-bias limit, and accounts for the finite temperature smearing of the Fermi-Dirac distribution. This expression has been used in analyzing other SIS systems, including those exhibiting multiple Andreev reflections. [10, 133]

Fig 7.2a-7.2d shows the measured noise intensity of an $x = 0.14$ device with the red dashed line indicating the dependence expected for single-electron tunneling, $S_{I,e}$ At temperatures far above $T_c = 37$ K, the measured noise value agrees with this expectation very well. As temperature approaches T_c from above, the measured noise noticeably exceeds $S_{I,e}$. When the temperature falls below T_c, the excess noise above $S_{I,e}$ becomes increasingly pronounced. At the lowest temperatures in our system, the noise is nonmonotonic, with peak features at ±6 mV, approximately $\pm\Delta/e$, if the full width of the zero-bias suppression of conductance is interpreted as $4\Delta/e$.

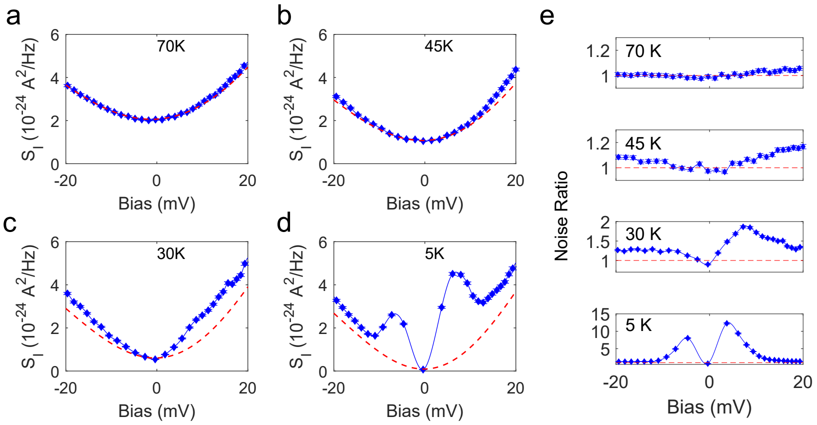

Figure 7.2 : Noise compared with single electron tunneling expectations. **a-d**, For $x = 0.14$ doping, at high temperatures the measured noise (blue points with error bars) agrees well with that expected for single electron tunneling ($S_{I,e}$, red dashed line), with no adjustable parameters. As T approaches T_c, noise is clearly in excess of $S_{I,e}$. When $T \ll T_c = 37K$, noise is nonmonotonic with peaks at approximately the half-width of the zero-bias conductance suppression. **e**, The noise ratio $S_I/S_{I,e}$ at the same temperatures as in **a-d**. The excess noise above $S_{I,e}$ results in a noise ratio larger than 1. The thin blue line is a spline interpolation.

We define the noise ratio as $S_I/S_{I,e}$, the ratio of measured noise to the single-electron tunneling expectation, and plot this in Fig 7.2e. At zero bias, the noise reduces to the Johnson-Nyquist level, and the noise ratio must approach 1, regardless of the charge of the carriers. At temperatures below T_c, the shot noise is enhanced greatly, with large noise ratios well above 1, see Fig 7.2e. The noise ratio is non-monotonic versus bias, increasing quickly with bias initially, reaching a maximum at the bias energy close to Δ, and decreasing again at higher biases. These large noise ratios are qualitatively reminiscent of multiple Andreev reflections (MAR), in which noise is enhanced as charge tunnels through multielectron processes. [134, 133, 15] The noise enhancement is largest at low temperatures and decreases gradually as the temperature approaches T_c. However, the noise ratio stays significantly above 1 even at temperatures well above T_c. Even more telling, both below and above T_c the noise ratio remains larger than 1 up to biases larger by a factor of two or more than $2\Delta_0/e$.

The large noise enhancements observed at low bias and below T_c are reminiscent of multicharge tunneling via higher-order Andreev reflection processes. [134, 133, 15] MAR has been reported in SIS structures, and while coherence is not required for Andreev processes, barrier transparency plays a critical role in the magnitude of the effect. While lacking a detailed theoretical prediction for this particular situation (d-wave order parameter, c-axis tunneling with preservation of transverse momentum), it is possible to compare the enhanced noise peaks with a simple model.

As different multiple Andreev charge transfer processes are kinetically allowed depending on the bias, the expected effective charge is bias-dependent ($q^* = ne$ for $2\Delta/n < eV < 2\Delta/(n-1)$ for n = 2, 3, ...). [15] Figure 7.3 shows a finite temperature expectation for the noise and noise ratio as a function of bias, V, using $S_I = 2q^*(V)I coth(q^*(V)V/2k_BT)$ with this assumption for q^* as the comparator to Poissonian single-charge tunneling, along with the data at 5 K for the sample used in Figure 7.2. The observed enhanced noise peaks differ in detail from the simplified MAR expectations.

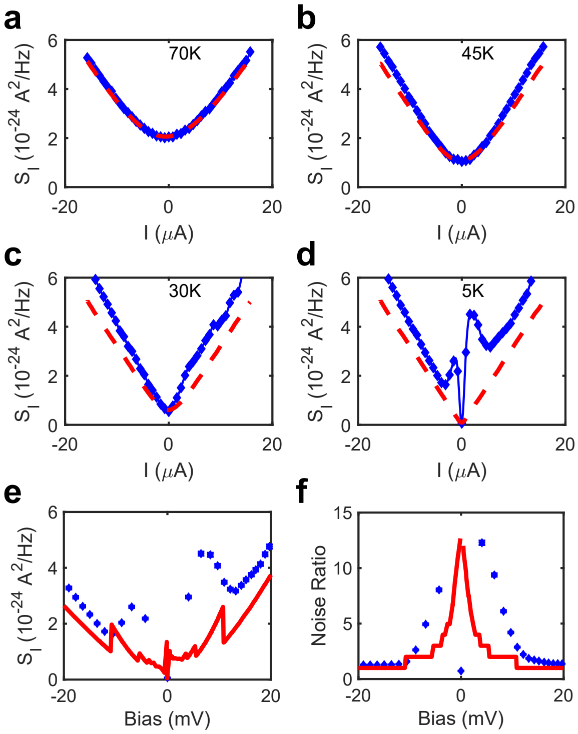

Figure 7.3 : Noise as a function of current, and comparison with Andreev reflection. **a**–**d**, The red dashed line shows the single-charge tunneling Poissonian expectation based on the measured $I(V)$ at each temperature. **e**, **f**, The red traces assume a bias-dependent effective charge based on kinetically allowed Andreev processes for a fixed isotropic gap Δ, combined with a finite temperature expectation for the noise.

7.4 Electron pairing percentage

The most natural explanation of the enhanced noise is a paired-charge contribution to tunneling that starts already in the pseudogap phase, for T well above T_c and/or V well above $2\Delta_0/e$, and evolves into higher-order processes below T_c at biases within

$2\Delta_0/e$. To quantify our results, from the measured S_I we can extract the T- and V-dependent 'effective charge' q^* defined via $S_I = 2qIcoth(q^*V/2k_BT)$. In a standard Bardeen-Cooper-Schrieffer (BCS) superconductor, $q^* = e$ outside the superconducting gap region enclosed by the $2\Delta_0/e$ line that terminates at T_c, while at low bias and temperature, $q^* \approx 2e$ in the absence of higher-order processes and can be even larger if higher-order processes contribute to tunneling. [134, 133, 15]

In our samples, we observe $q^* > e$ well outside the $2\Delta(T)/e$ line. In that region, we make the phenomenological assumption to model a fraction z of tunneling current I as contributed by paired carriers. Within this model [133] the shot noise is expected to be $S_I = (1 - z)2eIcoth(eV/2k_BT) + z4eIcoth(eV/k_BT)$. The experimentally determined function $z(V, T)$ is shown in Fig. 7.4 for the doping levels $x = 0.10$, 0.12, 0.14, and 0.15, respectively. Clearly, at every doping pairs are present far outside the superconducting gap region $2\Delta(T)/e$ that would be expected in a d-wave BCS superconductor with the corresponding value of T_c We note that there is a difference between the fraction of c-axis tunneling current contributed by paired carriers and the fraction of all carriers that are paired. The actual pair density could be larger, since the tunneling probability for incoherent pairs may well be smaller than that for single electrons. Moreover, note that unlike in scanning tunneling microscopy, which is spatially localized, these atomically-flat, large-area tunneling structures favor conservation of the transverse (a-b plane) quasi-momentum in the c-axis tunneling, which is dominated by carriers from the antinode portion of the Fermi surface [135], where the pseudogap is maximal. [18]

Our tunneling conductance data delineate the superconducting-gap region, the

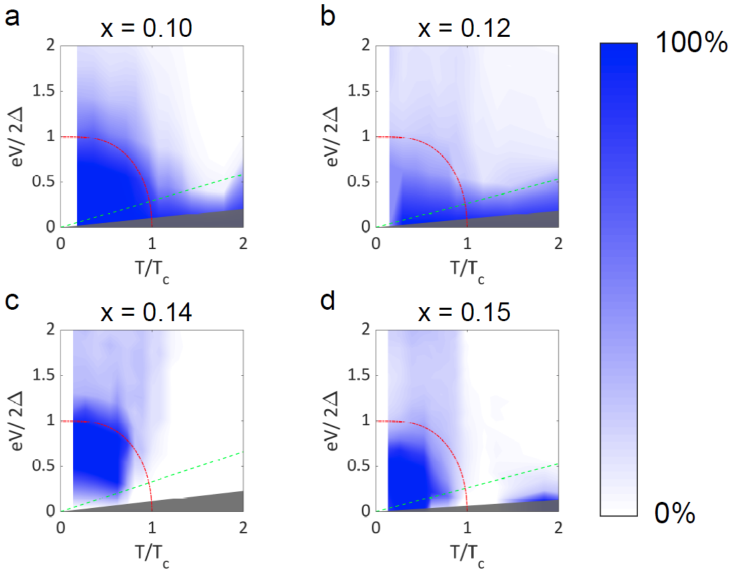

Figure 7.4 : The percentage of tunneling paired charges, z, as a function of doping level x, temperature T and bias V, as inferred from shot-noise measurements on LSCO/LCO/LSCO tunnel junctions. **a-d**, the data for doping levels $x = 0.10$, 0.12, 0.14, and 0.15, respectively. Red dash-dot lines: the superconducting gap region outside which one would expect $z = 0$ from the BCS theory for the measured values of T_c. Green dashed line: $V = k_BT/e$. As $eV/k_BT \to 0$, discrimination of z via noise measurements is not possible. Grey region indicates where uncertainty in z exceeds 0.5. For all doping levels, the contribution of pairs to the tunneling current extends well outside the super-conducting region and into the pseudogap regime.

boundary of which is consistent with previous observations of the phase-fluctuating superconductivity by THz spectroscopy.[19] This superconducting-gap region is clearly distinct from the pseudogap region identified outside of this boundary, suggesting that these are two different phases. On the other hand, the evolution of both the conductance and the enhanced noise between the normal state and the superconducting-gap regions is very smooth, without any kinks at the boundary. The key new finding here is that electron pairing, as detected through super-Poissonian shot noise, persists into the normal state and at bias energy scales large compared to the superconducting gap scale.

7.5 Sample variations

We measured two devices of each doping level from x = 0.15 to x = 0.10. In Fig 7.5 the noise ratio is shown for the eight devices. The shot noise intensity shows an enhancement above single-charge tunneling expectations above T_c for each doping level. At temperatures far above T_c, the noise density is close to the prediction for single-electron tunneling, with the noise ratio close to 1.

We also observed some variance from sample to sample. For the x = 0.15 optimal doping sample, the noise ratio falls below 1 at high temperatures when the bias is larger than $10mV$. This might be related to the charge transfer issue [136, 137, 138] as the doping level increases, which would indicate increased barrier transparency and undermine the constant-barrier tunneling approximation. For the x = 0.14 doping sample in Fig 7.5b, we observe atypically large enhancement of the noise ratio at temperatures below T_c. One possible explanation for enhanced noise response in this device relative to the others is a local variation in the barrier properties, as described above. These observations are strong motivations for future experiments to examine noise response with thinner LCO barriers, as well as to further study in-depth the crystalline, chemical, and electronic structure of the barriers and interfaces using transmission electron microscopy and electron energy loss spectroscopy with atomic-resolution.

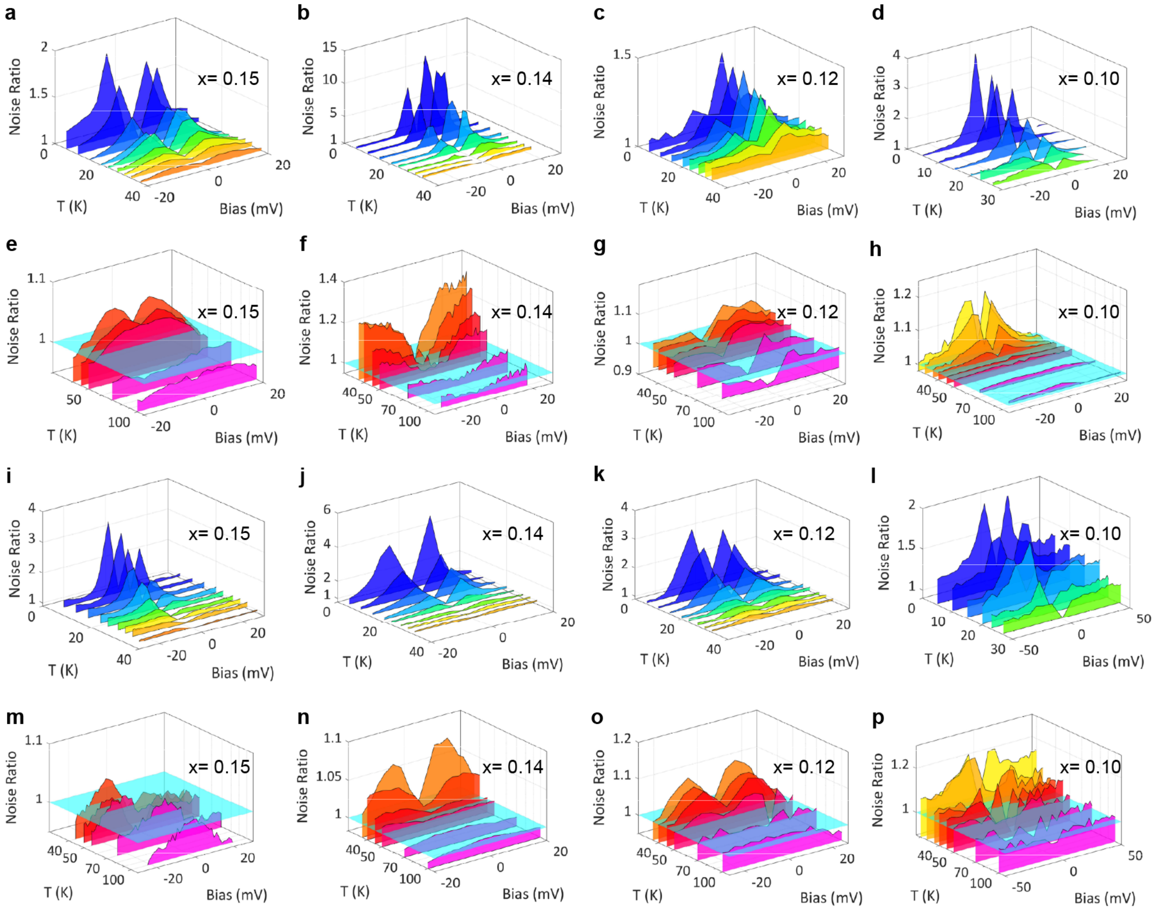

Figure 7.5 : The LSCO tunnel junction sample-to-sample variance from 0.15 doped to 0.10 doped. **a**–**h**, The noise ratio for the four LSCO devices at various doping levels as indicated, measured below T_c (**a**–**d**) and above T_c (**e**–**h**). **i**–**p**, The noise ratio for the other four LSCO devices at various doping levels as indicated, measured below T_c (**i**–**l**) and above T_c (**m**–**p**).

7.6 Shot noise in Nb tunnel junctions

An analogous noise measurements were performed on a $Nb/AlO_x/Nb$ tunnel junction, available commercially from STAR Cryoelectronics. The junction is fabricated on a doped Si substrate, and the critical temperature of the Nb electrodes is approximately 9 K.

The differential conductance and noise of the device are shown in 7.6**a-d**, while 7.6**e** shows the results when z is extracted from the data, following the same procedures as for the cuprate devices. Because of the comparatively low junction resistance, the bias range is restricted by limitations on the measurement current, and contributions of 1/f noise that grow quadratically with bias current. The low junction resistance also corresponds to a higher amplifier noise contour for the first-stage LI-75 amplifiers, compared with the higher resistance LSCO devices. Noise measurements within the gap bias range in the superconducting regime in this structure are obscured by the presence of Josephson current in the device below T_c and resulting enhanced environmental pickup.

7.7 RF shot noise measurement attempt

RF shot noise measurement is also tried in LSCO/LCO/LSCO tunnel junctions, see Figure 7.7. However, as the device is extremely non-linear at low temperatures, see Figure 7.7**a**, the RF measurement scheme does not work well. In the RF measurement, it has been assumed that the conductance does not change versus bias. In the LSCO/LCO/LSCO tunnel junction case, at low temperatures, the conductance has ”V” shape dependence. At a small bias range, the J-N current noise is largest at zeros bias and decays when applied voltage bias. This effect might even overcome the excess shot noise due to the tunneling process and results in a negative value when calculating $S_I(V) - S_I(0)$, see Figure 7.7**b**. Also, the inductance and effective capacitance of the superconducting material change greatly during the transition. Even if $R(V = 0)$ goes smoothly through T_c, the full complex magnitude of the impedance

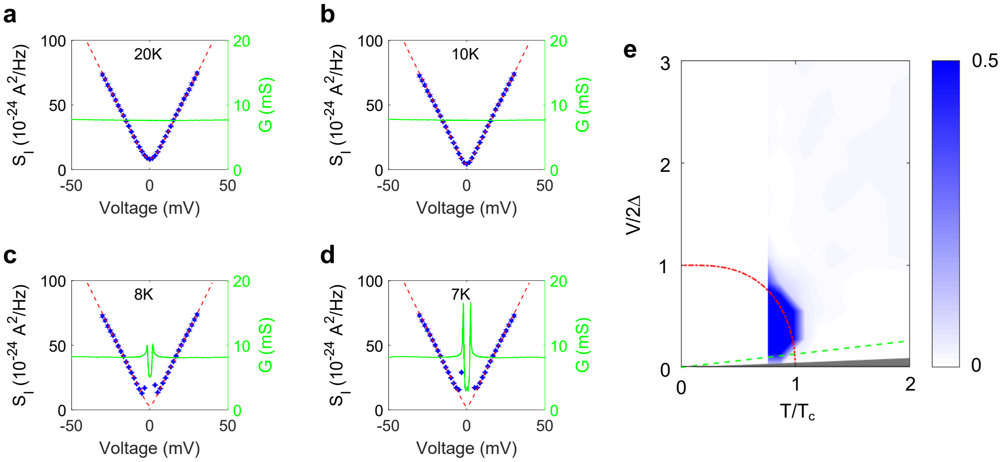

Figure 7.6 : Shot noise in a Nb tunnel junction. **a-d**. Noise measurements (blue points with error bars) and differential conductance (green) as a function of bias and temperature for a commercial $Nb/AlO_x/Nb$ tunnel junction that exhibits Josephson supercurrent below $T_c = 9K$. **e**. Inferred pair fraction z as a function of bias and temperature for this device. Red dash-dot line: the superconducting gap region outside which one would expect z = 0 from the BCS theory for the measured value of T_c. Green dashed line: $V = k_BT/e$. As $eV/k_BT \to 0$, discrimination of z via noise measurements is not possible. Grey region indicates where uncertainty in z exceeds 0.5.

is likely to change dramatically. All these make the interpretation of RF shot noise measurement result very difficult.

7.8 Summary

In this chapter, we went through the shot noise measurement in LSCO/LCO/LSCO tunnel junctions. It is found that the transition between the nomal state and the superconducting gap is a smooth process without any kinks at the boundary. Shot noise measurement on those tunnel junctions reveals that electron pairing persists into the normal state and at bias energy scales large compared to the superconduct-

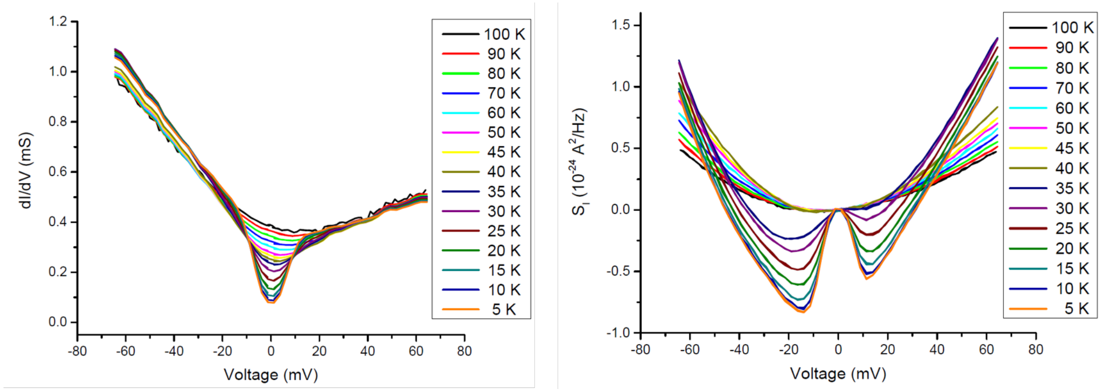

Figure 7.7 : Conductance and RF shot noise measurement in LSCO/LCO/LSCO tunnel junction.

ing gap scale. The presence of pairs above T_c and in a bias regime expected to be dominated by the antinodal portion of the Brillouin zone constrains models of the pseudogap. While fluctuating order above T_c is always a possibility, pairing at energies large compared to the superconducting gap. It remains an open question how the pairs inferred in these tunneling measurements relate to ordered states [87], including possible pair density waves [139], and electronic nematicity [140], the spontaneous breaking of the rotational symmetry in the electronic fluid detected in the pseudogap region in several copper oxides [141].

Bibliography

[1] "Metal Insulator Transition." `http://guava.physics.uiuc.edu/~nigel/courses/563/Essays_2010/PDF/meng1.pdf`. Accessed: 2019-10-30.

[2] C. Renner, B. Revaz, J.-Y. Genoud, K. Kadowaki, and O. Fischer, "Pseudogap Precursor of the Superconducting Gap in Under- and Overdoped $Bi_2Sr_2CaCu_2O_{8+\delta}$," *Phys. Rev. Lett.*, vol. 80, pp. 149–152, Jan 1998.

[3] A. P. Ramirez, "Colossal magnetoresistance," *Journal of Physics: Condensed Matter*, vol. 9, pp. 8171–8199, sep 1997.

[4] J. Custers, P. Gegenwart, H. Wilhelm, K. R. Neumaier, Y. Tokiwa, O. Trovarelli, C. Geibel, F. Steglich, C. Pépin, and P. E. Coleman, "The break-up of heavy electrons at a quantum critical point," *Nature*, vol. 424, pp. 524–527, 2003.

[5] S. W. Stanwyck, P. Gallagher, J. R. Williams, and D. Goldhaber-Gordon, "Universal conductance fluctuations in electrolyte-gated $SrTiO_3$ nanostructures," *Applied Physics Letters*, vol. 103, no. 21, p. 213504, 2013.

[6] "Aharonov-Bohm effect and geometric phase." `http://physics.gu.se/~tfkhj/TOPO/Aharonov-Bohm.pdf`. Accessed: 2019-10-30.

[7] A. van Oudenaarden, M. H. Devoret, Y. V. Nazarov, and J. E. Mooij, "Magneto-electric Aharonov–Bohm effect in metal rings," *Nature*, vol. 391, no. 6669,

pp. 768–770, 1998.

[8] B. J. van Wees, H. van Houten, C. W. J. Beenakker, J. G. Williamson, L. P. Kouwenhoven, D. van der Marel, and C. T. Foxon, "Quantized conductance of point contacts in a two-dimensional electron gas," *Phys. Rev. Lett.*, vol. 60, pp. 848–850, Feb 1988.

[9] K. v. Klitzing, G. Dorda, and M. Pepper, "New Method for High-Accuracy Determination of the Fine-Structure Constant Based on Quantized Hall Resistance," *Phys. Rev. Lett.*, vol. 45, pp. 494–497, Aug 1980.

[10] L. Spietz, K. W. Lehnert, I. Siddiqi, and R. J. Schoelkopf, "Primary Electronic Thermometry Using the Shot Noise of a Tunnel Junction," *Science*, vol. 300, no. 5627, pp. 1929–1932, 2003.

[11] M. Reznikov, M. Heiblum, H. Shtrikman, and D. Mahalu, "Temporal Correlation of Electrons: Suppression of Shot Noise in a Ballistic Quantum Point Contact," *Phys. Rev. Lett.*, vol. 75, pp. 3340–3343, Oct 1995.

[12] L. Saminadayar, D. C. Glattli, Y. Jin, and B. Etienne, "Observation of the $e/3$ Fractionally Charged Laughlin Quasiparticle," *Phys. Rev. Lett.*, vol. 79, pp. 2526–2529, Sep 1997.

[13] X. Jehl, M. Sanquer, R. Calemczuk, and D. Mailly, "Detection of doubled shot noise in short normal-metal/ superconductor junctions," *Nature*, vol. 405, no. 6782, pp. 50–53, 2000.

[14] "Single Particle Tunneling." `http://www.phys.nthu.edu.tw/~spin/course/105S/Ch10-5%20(new).pdf`. Date: 2019-10-29.

[15] Y. Ronen, Y. Cohen, J.-H. Kang, A. Haim, M.-T. Rieder, M. Heiblum, D. Mahalu, and H. Shtrikman, “Charge of a quasiparticle in a superconductor,” *Proceedings of the National Academy of Sciences*, vol. 113, no. 7, pp. 1743–1748, 2016.

[16] Y. Cao, V. Fatemi, S. Fang, K. Watanabe, T. Taniguchi, E. Kaxiras, and P. Jarillo-Herrero, “Unconventional superconductivity in magic-angle graphene superlattices,” *Nature*, vol. 556, p. 43, 2018.

[17] J. Tahir-Kheli and W. A. Goddard, “The chiral plaquette polaron paradigm (CPPP) for high temperature cuprate superconductors,” *Chemical Physics Letters*, vol. 472, no. 4, pp. 153 – 165, 2009.

[18] B. Keimer, S. A. Kivelson, M. R. Norman, S. Uchida, and J. Zaanen, “From quantum matter to high-temperature superconductivity in copper oxides,” *Nature*, vol. 518, p. 179, 2015.

[19] L. S. Bilbro, R. V. Aguilar, G. Logvenov, O. Pelleg, I. Bozǒvić, and N. P. Armitage, “Temporal correlations of superconductivity above the transition temperature in $La_{2-x}Sr_xCuO_4$ probed by terahertz spectroscopy,” *Nature Physics*, vol. 7, no. 4, pp. 298–302, 2011.

[20] J. Serrano, A. Bosak, R. Arenal, M. Krisch, K. Watanabe, T. Taniguchi, H. Kanda, A. Rubio, and L. Wirtz, “Vibrational properties of hexagonal boron nitride: Inelastic x-ray scattering and ab initio calculations,” *Phys. Rev. Lett.*, vol. 98, p. 095503, Mar 2007.

[21] H. J. Schulz, “Fermi liquids and non–Fermi liquids,” 1995.

[22] B. Andraka and A. M. Tsvelik, "Observation of non-Fermi-liquid behavior in $U_{0.2}Y_{0.8}Pd_3$," *Phys. Rev. Lett.*, vol. 67, pp. 2886–2889, Nov 1991.

[23] O. Trovarelli, C. Geibel, S. Mederle, C. Langhammer, F. M. Grosche, P. Gegenwart, M. Lang, G. Sparn, and F. Steglich, "$YbRh_2Si_2$: Pronounced Non-Fermi-Liquid Effects above a Low-Lying Magnetic Phase Transition," *Phys. Rev. Lett.*, vol. 85, pp. 626–629, Jul 2000.

[24] O. Parcollet and A. Georges, "Non-Fermi-liquid regime of a doped Mott insulator," *Phys. Rev. B*, vol. 59, pp. 5341–5360, Feb 1999.

[25] A. Krimmel, A. Günther, W. Kraetschmer, H. Dekinger, N. Büttgen, A. Loidl, S. G. Ebbinghaus, E.-W. Scheidt, and W. Scherer, "Non-Fermi-liquid behavior in $CaCu_3Ru_4O_{12}$," *Phys. Rev. B*, vol. 78, p. 165126, Oct 2008.

[26] C. Kittel, *Introduction to Solid State Physics*. Wiley Series on the Science and Technology of Materials, Wiley, 1953.

[27] P. Kuiper, G. Kruizinga, J. Ghijsen, G. A. Sawatzky, and H. Verweij, "Character of Holes in $Li_xNi_{1-x}O$ and Their Magnetic Behavior," *Phys. Rev. Lett.*, vol. 62, pp. 221–224, Jan 1989.

[28] V. I. Anisimov, M. A. Korotin, and E. Z. Kurmaev, "Band-structure description of mott insulators (NiO, MnO, FeO, CoO)," *Journal of Physics: Condensed Matter*, vol. 2, pp. 3973–3987, apr 1990.

[29] M. M. Qazilbash, M. Brehm, B.-G. Chae, P.-C. Ho, G. O. Andreev, B.-J. Kim, S. J. Yun, A. V. Balatsky, M. B. Maple, F. Keilmann, H.-T. Kim, and D. N. Basov, "Mott transition in vo2 revealed by infrared spectroscopy and nano-imaging," *Science*, vol. 318, no. 5857, pp. 1750–1753, 2007.

[30] J. Hubbard and B. H. Flowers, "Electron correlations in narrow energy bands," *Proceedings of the Royal Society of London. Series A. Mathematical and Physical Sciences*, vol. 276, no. 1365, pp. 238–257, 1963.

[31] J. G. Bednorz and K. A. Müller, "Possible high Tc superconductivity in the Ba−La−Cu−O system," *Zeitschrift für Physik B Condensed Matter*, vol. 64, no. 2, pp. 189–193, 1986.

[32] J. Bardeen, L. N. Cooper, and J. R. Schrieffer, "Microscopic Theory of Superconductivity," *Phys. Rev.*, vol. 106, pp. 162–164, Apr 1957.

[33] K. Andres, J. E. Graebner, and H. R. Ott, "4f-Virtual-Bound-State Formation in $CeAl_3$ at Low Temperatures," *Phys. Rev. Lett.*, vol. 35, pp. 1779–1782, Dec 1975.

[34] Q. Si and F. Steglich, "Heavy Fermions and Quantum Phase Transitions," *Science*, vol. 329, no. 5996, pp. 1161–1166, 2010.

[35] S. S. P. Parkin, K. P. Roche, M. G. Samant, P. M. Rice, R. B. Beyers, R. E. Scheuerlein, E. J. O'Sullivan, S. L. Brown, J. Bucchigano, D. W. Abraham, Y. Lu, M. Rooks, P. L. Trouilloud, R. A. Wanner, and W. J. Gallagher, "Exchange-biased magnetic tunnel junctions and application to nonvolatile magnetic random access memory (invited)," *Journal of Applied Physics*, vol. 85, no. 8, pp. 5828–5833, 1999.

[36] A. Chanthbouala, A. Crassous, V. Garcia, K. Bouzehouane, S. Fusil, X. Moya, J. Allibe, B. Dlubak, J. Grollier, S. Xavier, C. Deranlot, A. Moshar, R. Proksch, N. D. Mathur, M. Bibes, and A. Barthélémy, "Solid-state memories based on

ferroelectric tunnel junctions," *Nature Nanotechnology*, vol. 7, no. 2, pp. 101–104, 2012.

[37] Y. Makhlin, G. Scöhn, and A. Shnirman, "Josephson-junction qubits with controlled couplings," *Nature*, vol. 398, no. 6725, pp. 305–307, 1999.

[38] J. Q. You, J. S. Tsai, and F. Nori, "Scalable Quantum Computing with Josephson Charge Qubits," *Phys. Rev. Lett.*, vol. 89, p. 197902, Oct 2002.

[39] C. Prasittichai, J. R. Avila, O. K. Farha, and J. T. Hupp, "Systematic Modulation of Quantum (Electron) Tunneling Behavior by Atomic Layer Deposition on Nanoparticulate SnO_2 and TiO_2 Photoanodes," *Journal of the American Chemical Society*, vol. 135, no. 44, pp. 16328–16331, 2013.

[40] N. Tezuka, N. Ikeda, F. Mitsuhashi, and S. Sugimoto, "Improved tunnel magnetoresistance of magnetic tunnel junctions with heusler $Co_2FeAl_{0.5}Si_{0.5}$ electrodes fabricated by molecular beam epitaxy," *Applied Physics Letters*, vol. 94, no. 16, p. 162504, 2009.

[41] V. E. Calado, S. Goswami, G. Nanda, M. Diez, A. R. Akhmerov, K. Watanabe, T. Taniguchi, T. M. Klapwijk, and L. M. K. Vandersypen, "Ballistic Josephson junctions in edge-contacted graphene," *Nature Nanotechnology*, vol. 10, p. 761, 2015.

[42] W. Wang, A. Narayan, L. Tang, K. Dolui, Y. Liu, X. Yuan, Y. Jin, Y. Wu, I. Rungger, S. Sanvito, and F. Xiu, "Spin-Valve Effect in NiFe/MoS_2/NiFe Junctions," *Nano Letters*, vol. 15, no. 8, pp. 5261–5267, 2015.

[43] S. A. Cybart, E. Y. Cho, T. J. Wong, B. H. Wehlin, M. K. Ma, C. Huynh, and R. C. Dynes, "Nano Josephson superconducting tunnel junctions in

$YBa_2Cu_3O_{7-\delta}$ directly patterned with a focused helium ion beam," *Nature Nanotechnology*, vol. 10, p. 598, 2015.

[44] W. Schottky, "Über spontane Stromschwankungen in verschiedenen Elektrizitätsleitern," *Annalen der Physik*, vol. 362, no. 23, pp. 541–567, 1918.

[45] T. G. Griffiths, E. Comforti, M. Heiblum, A. Stern, and V. Umansky, "Evolution of Quasiparticle Charge in the Fractional Quantum Hall Regime," *Phys. Rev. Lett.*, vol. 85, pp. 3918–3921, Oct 2000.

[46] "There's Plenty of Room at the Bottom." `http://metamodern.com/2009/12/29/theres-plenty-of-room-at-the-bottom"-feynman-1959/`. Date: 1959-12-29.

[47] R. Landauer, "Spatial Variation of Currents and Fields Due to Localized Scatterers in Metallic Conduction," *IBM Journal of Research and Development*, vol. 1, pp. 223–231, July 1957.

[48] P. A. Lee and A. D. Stone, "Universal Conductance Fluctuations in Metals," *Phys. Rev. Lett.*, vol. 55, pp. 1622–1625, Oct 1985.

[49] Y. Aharonov and D. Bohm, "Significance of Electromagnetic Potentials in the Quantum Theory," *Phys. Rev.*, vol. 115, pp. 485–491, Aug 1959.

[50] Y. V. Sharvin, "A Possible Method for Studying Fermi Surfaces," *JETP*, vol. 48, no. 3, p. 984, 1964.

[51] T. J. Thornton, M. Pepper, H. Ahmed, D. Andrews, and G. J. Davies, "One-Dimensional Conduction in the 2D Electron Gas of a GaAs-AlGaAs Heterojunction," *Phys. Rev. Lett.*, vol. 56, pp. 1198–1201, Mar 1986.

[52] H. Nyquist, “Thermal Agitation of Electric Charge in Conductors,” *Phys. Rev.*, vol. 32, pp. 110–113, Jul 1928.

[53] Y. Blanter and M. Büttiker, “Shot noise in mesoscopic conductors,” *Physics Reports*, vol. 336, no. 1, pp. 1 – 166, 2000.

[54] H. Reittu, “Fermi's golden rule and Bardeen's tunneling theory,” *American Journal of Physics - AMER J PHYS*, vol. 63, 10 1995.

[55] M. Büttiker, “Scattering theory of current and intensity noise correlations in conductors and wave guides,” *Phys. Rev. B*, vol. 46, pp. 12485–12507, Nov 1992.

[56] C. W. J. Beenakker and M. Büttiker, “Suppression of shot noise in metallic diffusive conductors,” *Phys. Rev. B*, vol. 46, pp. 1889–1892, Jul 1992.

[57] D. van Delft and P. Kes, “The discovery of superconductivity,” *Physics Today*, vol. 63, no. 9, pp. 38–43, 2010.

[58] W. Meissner and R. Ochsenfeld, “Ein neuer Effekt bei Eintritt der Supraleitfähigkeit,” *Naturwissenschaften*, vol. 21, pp. 787–788, Nov 1933.

[59] F. London, H. London, and F. A. Lindemann, “The electromagnetic equations of the supraconductor,” *Proceedings of the Royal Society of London. Series A - Mathematical and Physical Sciences*, vol. 149, no. 866, pp. 71–88, 1935.

[60] I. Giaever, “Energy Gap in Superconductors Measured by Electron Tunneling,” *Phys. Rev. Lett.*, vol. 5, pp. 147–148, Aug 1960.

[61] B. Josephson, “Possible new effects in superconductive tunnelling,” *Physics Letters*, vol. 1, no. 7, pp. 251 – 253, 1962.

[62] M. Tinkham, *Introduction to Superconductivity.* Dover Publications, 2 ed., June 2004.

[63] Jérome, D., Mazaud, A., Ribault, M., and Bechgaard, K., "Superconductivity in a synthetic organic conductor $(TMTSF)_2PF_6$," *J. Physique Lett.*, vol. 41, no. 4, pp. 95–98, 1980.

[64] J. Singleton and C. Mielke, "Quasi-two-dimensional organic superconductors: A review," *Contemporary Physics*, vol. 43, no. 2, pp. 63–96, 2002.

[65] W. A. Little, "Possibility of Synthesizing an Organic Superconductor," *Phys. Rev.*, vol. 134, pp. A1416–A1424, Jun 1964.

[66] F. Steglich, J. Aarts, C. D. Bredl, W. Lieke, D. Meschede, W. Franz, and H. Schäfer, "Superconductivity in the Presence of Strong Pauli Paramagnetism: $CeCu_2Si_2$," *Phys. Rev. Lett.*, vol. 43, pp. 1892–1896, Dec 1979.

[67] M. K. Wu, J. R. Ashburn, C. J. Torng, P. H. Hor, R. L. Meng, L. Gao, Z. J. Huang, Y. Q. Wang, and C. W. Chu, "Superconductivity at 93 k in a new mixed-phase Y–Ba–Cu–O compound system at ambient pressure," *Phys. Rev. Lett.*, vol. 58, pp. 908–910, Mar 1987.

[68] "Superconductivity above 130 k in the Hg–Ba–Ca–Cu–O system," *Nature*, vol. 363, no. 6424, pp. 56–58, 1993.

[69] Y. Kamihara, H. Hiramatsu, M. Hirano, R. Kawamura, H. Yanagi, T. Kamiya, and H. Hosono, "Iron-Based Layered Superconductor: LaOFeP," *Journal of the American Chemical Society*, vol. 128, no. 31, pp. 10012–10013, 2006.

[70] T. C. Ozawa and S. M. Kauzlarich, “Chemistry of layered d-metal pnictide oxides and their potential as candidates for new superconductors,” *Science and Technology of Advanced Materials*, vol. 9, no. 3, p. 033003, 2008.

[71] J. J. Hamlin, R. E. Baumbach, D. A. Zocco, T. A. Sayles, and M. B. Maple, “Superconductivity in single crystals of LaFePO,” *Journal of Physics: Condensed Matter*, vol. 20, p. 365220, aug 2008.

[72] D. Möckli and E. de Mello, “The $Ba_{0.6}K_{0.4}Fe_2As_2$ superconducting four-gap temperature evolution: A multi-band Chebyshev–BdG approach,” *Physics Letters A*, vol. 380, no. 33, pp. 2565–2569, 2016.

[73] Z. Deng, X. C. Wang, Q. Q. Liu, S. J. Zhang, Y. X. Lv, J. L. Zhu, R. C. Yu, and C. Q. Jin, “A new “111” type iron pnictide superconductor LiFeP,” *EPL (Europhysics Letters)*, vol. 87, p. 37004, aug 2009.

[74] Y. Mizuguchi, F. Tomioka, S. Tsuda, T. Yamaguchi, and Y. Takano, “Substitution Effects on FeSe Superconductor,” *Journal of the Physical Society of Japan*, vol. 78, no. 7, p. 074712, 2009.

[75] W. L. McMillan, “Transition Temperature of Strong-Coupled Superconductors,” *Phys. Rev.*, vol. 167, pp. 331–344, Mar 1968.

[76] P. Prelovšek and A. Ramšak, “Spin-fluctuation mechanism of superconductivity in cuprates,” *Phys. Rev. B*, vol. 72, p. 012510, Jul 2005.

[77] S. A. Kivelson, I. P. Bindloss, E. Fradkin, V. Oganesyan, J. M. Tranquada, A. Kapitulnik, and C. Howald, “How to detect fluctuating stripes in the high-temperature superconductors,” *Rev. Mod. Phys.*, vol. 75, pp. 1201–1241, Oct 2003.

[78] R. Zhong, B. L. Winn, G. Gu, D. Reznik, and J. M. Tranquada, “Evidence for a Nematic Phase in $La_{1.75}Sr_{0.25}NiO_4$,” *Phys. Rev. Lett.*, vol. 118, p. 177601, Apr 2017.

[79] W. W. Warren, R. E. Walstedt, G. F. Brennert, R. J. Cava, R. Tycko, R. F. Bell, and G. Dabbagh, “Cu spin dynamics and superconducting precursor effects in planes above T_c in $YBa_2Cu_3O_{6.7}$,” *Phys. Rev. Lett.*, vol. 62, pp. 1193–1196, Mar 1989.

[80] T. Valla, A. V. Fedorov, J. Lee, J. C. Davis, and G. D. Gu, “The ground state of the pseudogap in cuprate superconductors,” *Science*, vol. 314, no. 5807, pp. 1914–1916, 2006.

[81] L. Li, Y. Wang, S. Komiya, S. Ono, Y. Ando, G. D. Gu, and N. P. Ong, “Diamagnetism and Cooper pairing above T_c in cuprates,” *Phys. Rev. B*, vol. 81, p. 054510, Feb 2010.

[82] Y. Wang, L. Li, and N. P. Ong, “Nernst effect in high-T_c superconductors,” *Phys. Rev. B*, vol. 73, p. 024510, Jan 2006.

[83] J. Stajic, A. Iyengar, K. Levin, B. R. Boyce, and T. R. Lemberger, “Cuprate pseudogap: Competing order parameters or precursor superconductivity,” *Phys. Rev. B*, vol. 68, p. 024520, Jul 2003.

[84] P. A. Lee and X.-G. Wen, “Unusual Superconducting State of Underdoped Cuprates,” *Phys. Rev. Lett.*, vol. 78, pp. 4111–4114, May 1997.

[85] Q. Chen, I. Kosztin, B. Jankó, and K. Levin, “Pairing Fluctuation Theory of Superconducting Properties in Underdoped to Overdoped Cuprates,” *Phys. Rev. Lett.*, vol. 81, pp. 4708–4711, Nov 1998.

[86] V. J. Emery and S. A. Kivelson, "Importance of phase fluctuations in superconductors with small superfluid density," *Nature*, vol. 374, no. 6521, pp. 434–437, 1995.

[87] E. Berg, E. Fradkin, S. A. Kivelson, and J. M. Tranquada, "Striped superconductors: how spin, charge and superconducting orders intertwine in the cuprates," *New Journal of Physics*, vol. 11, p. 115004, Nov 2009.

[88] V. J. Emery, E. Fradkin, S. A. Kivelson, and T. C. Lubensky, "Quantum theory of the smectic metal state in stripe phases," *Phys. Rev. Lett.*, vol. 85, pp. 2160–2163, Sep 2000.

[89] P. Bourges and Y. Sidis, "Novel magnetic order in the pseudogap state of high-Tc copper oxides superconductors," *Comptes Rendus Physique*, vol. 12, no. 5, pp. 461 – 479, 2011. Superconductivity of strongly correlated systems.

[90] S. Chakravarty, R. B. Laughlin, D. K. Morr, and C. Nayak, "Hidden order in the cuprates," *Phys. Rev. B*, vol. 63, p. 094503, Jan 2001.

[91] C. M. Varma, "Pseudogap Phase and the Quantum-Critical Point in Copper-Oxide Metals," *Phys. Rev. Lett.*, vol. 83, pp. 3538–3541, Oct 1999.

[92] C. D. C. L. Benfatto, S. Caprara, "Gap and pseudogap evolution within the charge-ordering scenario for superconducting cuprates," *The European Physical Journal B*, vol. 17, no. 1, pp. 95 – 102, 2000.

[93] V. B. Geshkenbein, L. B. Ioffe, and A. I. Larkin, "Superconductivity in a system with preformed pairs," *Phys. Rev. B*, vol. 55, pp. 3173–3180, Feb 1997.

[94] J. F. ALLEN, "Prof. Frank Allen," *Nature*, vol. 209, no. 5019, pp. 133–133, 1966.

[95] P. J. Wheeler, J. N. Russom, K. Evans, N. S. King, and D. Natelson, "Shot Noise Suppression at Room Temperature in Atomic-Scale Au Junctions," *Nano Letters*, vol. 10, pp. 1287–1292, 04 2010.

[96] R. Chen, P. J. Wheeler, and D. Natelson, "Excess noise in STM-style break junctions at room temperature," *Phys. Rev. B*, vol. 85, p. 235455, Jun 2012.

[97] B. I. Ivanov, M. Trgala, M. Grajcar, E. Il'ichev, and H.-G. Meyer, "Cryogenic ultra-low-noise SiGe transistor amplifier," *Review of Scientific Instruments*, vol. 82, no. 10, p. 104705, 2011.

[98] L. DiCarlo, Y. Zhang, D. T. McClure, C. M. Marcus, L. N. Pfeiffer, and K. W. West, "System for measuring auto- and cross correlation of current noise at low temperatures," *Review of Scientific Instruments*, vol. 77, no. 7, p. 073906, 2006.

[99] B. G. M. Vandeginste, "Robust regression and outlier detection. p. j. rousseeuw and a. m. leroy, john wiley & sons, new york, 1987. no. of pages: 329. price: £31.95. isbn:0 471 85233 3," *Journal of Chemometrics*, vol. 2, no. 4, pp. 299–300, 1988.

[100] P. Zhou, L. Chen, Y. Liu, I. Sochnikov, A. T. Bollinger, M.-G. Han, Y. Zhu, X. He, I. Bozǒvić, and D. Natelson, "Electron pairing in the pseudogap state revealed by shot noise in copper oxide junctions," *Nature*, vol. 572, no. 7770, pp. 493–496, 2019.

[101] P. Zhou, W. J. Hardy, K. Watanabe, T. Taniguchi, and D. Natelson, "Shot noise

detection in hBN-based tunnel junctions," *Applied Physics Letters*, vol. 110, no. 13, p. 133106, 2017.

[102] R. Geick, C. H. Perry, and G. Rupprecht, "Normal modes in hexagonal boron nitride," *Phys. Rev.*, vol. 146, pp. 543–547, Jun 1966.

[103] A. K. Geim and K. S. Novoselov, "The rise of graphene," *Nature Materials*, vol. 6, no. 3, pp. 183–191, 2007.

[104] S. Manzeli, D. Ovchinnikov, D. Pasquier, O. V. Yazyev, and A. Kis, "2D transition metal dichalcogenides," *Nature Reviews Materials*, vol. 2, p. 17033, 2017.

[105] X. Ling, H. Wang, S. Huang, F. Xia, and M. S. Dresselhaus, "The renaissance of black phosphorus," *Proceedings of the National Academy of Sciences*, vol. 112, no. 15, pp. 4523–4530, 2015.

[106] Y. Zhang, J. J. Lee, R. G. Moore, W. Li, M. Yi, M. Hashimoto, D. H. Lu, T. P. Devereaux, D.-H. Lee, and Z.-X. Shen, "Superconducting Gap Anisotropy in Monolayer FeSe Thin Film," *Phys. Rev. Lett.*, vol. 117, p. 117001, Sep 2016.

[107] V. Shautsova, A. M. Gilbertson, N. C. G. Black, S. A. Maier, and L. F. Cohen, "Hexagonal Boron Nitride assisted transfer and encapsulation of large area CVD graphene," *Scientific Reports*, vol. 6, p. 30210, 2016.

[108] L. Wang, I. Meric, P. Y. Huang, Q. Gao, Y. Gao, H. Tran, T. Taniguchi, K. Watanabe, L. M. Campos, D. A. Muller, J. Guo, P. Kim, J. Hone, K. L. Shepard, and C. R. Dean, "One-Dimensional Electrical Contact to a Two-Dimensional Material," *Science*, vol. 342, no. 6158, pp. 614–617, 2013.

[109] U. Chandni, K. Watanabe, T. Taniguchi, and J. P. Eisenstein, "Signatures of Phonon and Defect-Assisted Tunneling in Planar Metal–Hexagonal Boron Nitride–Graphene Junctions," *Nano Letters*, vol. 16, no. 12, pp. 7982–7987, 2016.

[110] U. Chandni, K. Watanabe, T. Taniguchi, and J. P. Eisenstein, "Evidence for Defect-Mediated Tunneling in Hexagonal Boron Nitride-Based Junctions," *Nano Letters*, vol. 15, no. 11, pp. 7329–7333, 2015.

[111] I. Bozovic, "Atomic-layer engineering of superconducting oxides: yesterday, today, tomorrow," *IEEE Transactions on Applied Superconductivity*, vol. 11, pp. 2686–2695, March 2001.

[112] H. Shim, P. Chaudhari, G. Logvenov, and I. Bozovic, "Electron-Phonon Interactions in Superconducting $La_{1.84}Sr_{0.16}CuO_4$ Films," *Phys. Rev. Lett.*, vol. 101, p. 247004, Dec 2008.

[113] I. Bozovic, G. Logvenov, M. A. J. Verhoeven, P. Caputo, E. Goldobin, and T. H. Geballe, "No mixing of superconductivity and antiferromagnetism in a high-temperature superconductor," *Nature*, vol. 422, p. 873, 2003.

[114] Y. Yacoby, H. Zhou, R. Pindak, and I. Božović, "Atomic-layer synthesis and imaging uncover broken inversion symmetry in $La_{2-x}Sr_xCuO_4$ films," *Phys. Rev. B*, vol. 87, p. 014108, Jan 2013.

[115] J. Lee, K. Fujita, A. R. Schmidt, C. K. Kim, H. Eisaki, S. Uchida, and J. C. Davis, "Spectroscopic fingerprint of phase-incoherent superconductivity in the underdoped $Bi_2Sr_2CaCu_2O_{8+\delta}$," *Science*, vol. 325, no. 5944, pp. 1099–1103, 2009.

[116] R. C. Dynes, V. Narayanamurti, and J. P. Garno, "Direct Measurement of Quasiparticle-Lifetime Broadening in a Strong-Coupled Superconductor," *Phys. Rev. Lett.*, vol. 41, pp. 1509–1512, Nov 1978.

[117] J. W. Alldredge, J. Lee, K. McElroy, M. Wang, K. Fujita, Y. Kohsaka, C. Taylor, H. Eisaki, S. Uchida, P. J. Hirschfeld, and J. C. Davis, "Evolution of the electronic excitation spectrum with strongly diminishing hole density in superconducting $Bi_2Sr_2CaCu_2O_{8+\delta}$," *Nature Physics*, vol. 4, no. 4, pp. 319–326, 2008.

[118] S. Graser, P. J. Hirschfeld, and D. J. Scalapino, "Local quasiparticle lifetimes in a *d*-wave superconductor," *Phys. Rev. B*, vol. 77, p. 184504, May 2008.

[119] J. K. Ren, X. B. Zhu, H. F. Yu, Y. Tian, H. F. Yang, C. Z. Gu, N. L. Wang, Y. F. Ren, and S. P. Zhao, "Energy gaps in $Bi_2Sr_2CaCu_2O_{8+\delta}$ Cuprate superconductors," *Scientific Reports*, vol. 2, pp. 248 EP –, 02 2012.

[120] T. J. Reber, N. C. Plumb, Y. Cao, Z. Sun, Q. Wang, K. McElroy, H. Iwasawa, M. Arita, J. S. Wen, Z. J. Xu, G. Gu, Y. Yoshida, H. Eisaki, Y. Aiura, and D. S. Dessau, "Prepairing and the "filling" gap in the cuprates from the tomographic density of states," *Phys. Rev. B*, vol. 87, p. 060506, Feb 2013.

[121] M. Hashimoto, I. M. Vishik, R.-H. He, T. P. Devereaux, and Z.-X. Shen, "Energy gaps in high-transition-temperature cuprate superconductors," *Nature Physics*, vol. 10, p. 483, 2014.

[122] J. K. Ren, X. B. Zhu, H. F. Yu, Y. Tian, H. F. Yang, C. Z. Gu, N. L. Wang, Y. F. Ren, and S. P. Zhao, "Energy gaps in $Bi_2Sr_2CaCu_2O_{8+\delta}$ cuprate superconductors," *Scientific Reports*, vol. 2, p. 248, 2012.

[123] N. Gedik, D.-S. Yang, G. Logvenov, I. Bozovic, and A. H. Zewail, "Nonequilibrium phase transitions in cuprates observed by ultrafast electron crystallography," *Science*, vol. 316, no. 5823, pp. 425–429, 2007.

[124] L. Braicovich, J. van den Brink, V. Bisogni, M. M. Sala, L. J. P. Ament, N. B. Brookes, G. M. De Luca, M. Salluzzo, T. Schmitt, V. N. Strocov, and G. Ghiringhelli, "Magnetic Excitations and Phase Separation in the Underdoped $La_{2-x}Sr_xCuO_4$ Superconductor Measured by Resonant Inelastic X-Ray Scattering," *Phys. Rev. Lett.*, vol. 104, p. 077002, Feb 2010.

[125] A. G. Loeser, Z.-X. Shen, D. S. Dessau, D. S. Marshall, C. H. Park, P. Fournier, and A. Kapitulnik, "Excitation gap in the normal state of underdoped $Bi_2Sr_2CaCu_2O_{8+\delta}$," *Science*, vol. 273, no. 5273, pp. 325–329, 1996.

[126] H. Ding, T. Yokoya, J. C. Campuzano, T. Takahashi, M. Randeria, M. R. Norman, T. Mochiku, K. Kadowaki, and J. Giapintzakis, "Spectroscopic evidence for a pseudogap in the normal state of underdoped high-Tc superconductors," *Nature*, vol. 382, no. 6586, pp. 51–54, 1996.

[127] T. Kondo, Y. Hamaya, A. D. Palczewski, T. Takeuchi, J. S. Wen, Z. J. Xu, G. Gu, J. Schmalian, and A. Kaminski, "Disentangling Cooper-pair formation above the transition temperature from the pseudogap state in the cuprates," *Nature Physics*, vol. 7, p. 21, 2010.

[128] K. K. Gomes, A. N. Pasupathy, A. Pushp, S. Ono, Y. Ando, and A. Yazdani, "Visualizing pair formation on the atomic scale in the high-Tc superconductor $Bi_2Sr_2CaCu_2O_{8+\delta}$," *Nature*, vol. 447, no. 7144, pp. 569–572, 2007.

[129] Y. Kohsaka, T. Hanaguri, M. Azuma, M. Takano, J. C. Davis, and H. Takagi,

"Visualization of the emergence of the pseudogap state and the evolution to superconductivity in a lightly hole-doped Mott insulator," *Nature Physics*, vol. 8, no. 7, pp. 534–538, 2012.

[130] I. Božović, X. He, J. Wu, and A. T. Bollinger, "Dependence of the critical temperature in overdoped copper oxides on superfluid density," *Nature*, vol. 536, p. 309, 2016.

[131] P. A. Lee, N. Nagaosa, and X.-G. Wen, "Doping a Mott insulator: Physics of high-temperature superconductivity," *Rev. Mod. Phys.*, vol. 78, pp. 17–85, Jan 2006.

[132] S. Uchida, "Forefront in the Elucidation of the Mechanism of High-Temperature Superconductivity," *Japanese Journal of Applied Physics*, vol. 51, p. 010002, Dec 2011.

[133] P. Dieleman, H. G. Bukkems, T. M. Klapwijk, M. Schicke, and K. H. Gundlach, "Observation of Andreev Reflection Enhanced Shot Noise," *Phys. Rev. Lett.*, vol. 79, pp. 3486–3489, Nov 1997.

[134] J. C. Cuevas and M. Fogelström, "Shot Noise and Multiple Andreev Reflections in d-Wave Superconductors," *Phys. Rev. Lett.*, vol. 89, p. 227003, Nov 2002.

[135] O. Andersen, A. Liechtenstein, O. Jepsen, and F. Paulsen, "LDA energy bands, low-energy hamiltonians, t', t", $t_\perp(k)$, and $J_\perp$," *Journal of Physics and Chemistry of Solids*, vol. 56, no. 12, pp. 1573 – 1591, 1995. Proceedings of the Conference on Spectroscopies in Novel Superconductors.

[136] A. Gozar, G. Logvenov, L. F. Kourkoutis, A. T. Bollinger, L. A. Giannuzzi, D. A. Muller, and I. Božović, "High-temperature interface superconductivity

between metallic and insulating copper oxides," *Nature*, vol. 455, no. 7214, pp. 782–785, 2008.

[137] G. Logvenov, A. Gozar, and I. Božović, "High-temperature superconductivity in a single copper-oxygen plane," *Science*, vol. 326, no. 5953, pp. 699–702, 2009.

[138] A. T. Bollinger, G. Dubuis, J. Yoon, D. Pavuna, J. Misewich, and I. Božović, "Superconductor–insulator transition in $La_{2-x}Sr_xCuO_4$ at the pair quantum resistance," *Nature*, vol. 472, no. 7344, pp. 458–460, 2011.

[139] M. H. Hamidian, S. D. Edkins, S. H. Joo, A. Kostin, H. Eisaki, S. Uchida, M. J. Lawler, E.-A. Kim, A. P. Mackenzie, K. Fujita, J. Lee, and J. C. S. Davis, "Detection of a Cooper-pair density wave in $Bi_2Sr_2CaCu_2O_{8+x}$," *Nature*, vol. 532, p. 343, 2016.

[140] Y. Sato, S. Kasahara, H. Murayama, Y. Kasahara, E.-G. Moon, T. Nishizaki, T. Loew, J. Porras, B. Keimer, T. Shibauchi, and Y. Matsuda, "Thermodynamic evidence for a nematic phase transition at the onset of the pseudogap in $YBa_2Cu_3O_y$," *Nature Physics*, vol. 13, p. 1074, 2017.

[141] J. Wu, A. T. Bollinger, X. He, and I. Božović, "Spontaneous breaking of rotational symmetry in copper oxide superconductors," *Nature*, vol. 547, p. 432, 2017.

Appendix A

Low frequency cross-correlation measurement code

Here we use the Python win32com package to control the Labview VI programs to communicate with the instruments such as lock-in amplifier and digitizer to set the parameters and take the data. This wrapping method helps to modulate each function and is more memory efficient.

The basic flow of the shot noise measurement process is:

1. Using PPMS script to sweep the PPMS chamber temperature and stay at each desired temperature for certain time so we can finish measurement at each temperature.
2. The digitizer reads the temperature of the PPMS chamber. Once the temperature gets stabilized at the set temperatures, start the noise measurement processes.
3. Sweep the d.c. voltage that applied to the sample. At each voltage, we wait some time for the system to be stable and then use a high frequency digitizer to read and calculate the power spectral density.

The detailed Python code for the measurement is attached here.

```
import win32com.client
```

```
from tqdm import tqdm
from time import sleep
import numpy as np

def read_temp(T_addr):
    """
    Read temperature
    :param T_addr: Address of the temperature reading labview file
    :return:
    """
    Labview = win32com.client.Dispatch('Labview.Application')
    VI = Labview.getvireference(T_addr)
    VI._FlagAsMethod("Call")  # Flag "Call" as Method
    VI.Call()
    result=VI.getcontrolvalue('T')
    print(result)
    return result
    del VI

def add_volt(vi_addr, volt = 0):
    """
    Apply voltage to device
    :param vi_addr: Address for the voltage output labview file
    :param volt: output voltage value
    :return:
```

```
    """
    Labview = win32com.client.Dispatch('Labview.Application')
    VI = Labview.getvireference(vi_addr)
    VI._FlagAsMethod("Call")  # Flag "Call" as Method
    call_name, call_para = ['CH0_Vout'], [volt]
    VI.Call(call_name, call_para)
    del VI

def Xmeasurement(T, V, VIaddress, savefolder, AVE_NUM = 1000):
    """
    Cross-correlation measurement
    :param T: temperature of the system
    :param V: output dc voltage
    :param VIaddress: Address for the X-spectrum labview file
    :param savefolder: Address to save the file
    :param AVE_NUM: Number of spectrum average
    :return:
    """
    Labview = win32com.client.Dispatch('Labview.Application')
    VI = Labview.getvireference(VIaddress)
    VI._FlagAsMethod("Call")  # Flag "Call" as Method
    call_name, call_para = ['folder', 'T', 'V', 'AVE_NUM'], \
                           [savefolder, T, V, AVE_NUM]
    VI.Call(call_name, call_para)
    del VI
```

```
def T_stable(t, T_addr):
    ”””
    Decide if the temperature is stable or not
    :param t:
    :param T_addr: address of the temperature reading labview file
    :return:
    ”””
    Tlist=[]
    for _ in range(10):
        Tlist.append(read_temp(T_addr))
        sleep(10)

    Sd=np.std(Tlist)
    if Sd<0.1:
        return True
    else:
        return False



def run_volt_spec(V_max, V_step, T, spec_vi_addr, volt_vi_addr,
                  savefolder, AVE_NUM):
    ”””
    Sweep the DC voltage and take spectrum at each voltage
    :param V_max: maximum DC voltage
```

```
:param V_step: step of the voltage sweeping
:param T: temperature of system
:param spec_vi_addr: address of spectrum taking labview file
:param volt_vi_addr: address of voltage control labview file
:param savefolder: address for save files
:param AVE_NUM: number of spectrum average
:return:
"""
for v in tqdm(np.arange(0, V_max + V_step, V_step)):
    v = float(v)
    add_volt(volt_vi_addr, v)
    sleep(30)
    Xmeasurement(T, v, spec_vi_addr, savefolder, AVE_NUM)

# sweep voltage back down to 0
for v in tqdm(np.arange(V_max, -1, -1)):
    v = float(v)
    add_volt(volt_vi_addr, v)
    sleep(3)

# Taking spectrum while sweep to -V_max
for v in tqdm(np.arange(-V_step, -V_max - V_step, -V_step)):
    v = float(v)
    add_volt(volt_vi_addr, v)
    sleep(30)
```

```
        Xmeasurement(T, v, spec_vi_addr, savefolder, AVE_NUM)

    # sweep volt back to 0
    for v in tqdm(np.arange(-V_max, 1, 1)):
        v = float(v)
        add_volt(volt_vi_addr, v)
        sleep(3)

    print('Measurement done')

# For example, this is the code for running spectrum measurement
# at 100K, 50K and 10K
T_addr='read T from dac.vi'
spec_vi_addr = 'niScope EX Measurement_PZ0701.vi'
volt_vi_addr = 'DAQ6251_vout.vi'
savefolder = 'target_folder'
V_max = 9
V_step = 0.5
AVE_NUM = 2000
targetT= [100, 50, 10]
for t in targetT:
    while True:
        T=read_temp(T_addr)
        if T<t+0.2 and T>t-0.2:
            sleep(200)
```

```
    if T_stable(t, T_addr):
        print('Temperature␣stable␣at␣%d␣K' %(t))
        run_volt_spec(V_max, V_step, t, spec_vi_addr,
                      volt_vi_addr, savefolder, AVE_NUM)
        print('Finished␣spectrum␣at␣%d␣K' %(t))
        break
sleep(10)
```

Appendix B

Low frequency shot noise data analysis

The shot noise analysis is done with Matlab. The noise power spectral density data has two columns, with column one as the frequency, and column two as the noise intensity. Firstly, the noise power spectral density is fitted using a robust fit algorithm. After taking the calibration factor into consideration, one get $S_V(V^2/Hz)$ as a function of applied current I. The differential conductance data have 5 columns, with column 1 as the d.c. current I, column 2 as the d.c. voltage, column 3 as the a.c. current dI, column 4 as the a.c. voltage dV, and column 5 as the differential conductance dI/dV. Through interpolating, one can obtain the differential conductance and d.c. voltage at each applied current in the noise measurement. The current noise can be calculated by $S_I = S_V/(dV/dI)^2$ and one can plot it as a function versus either d.c. voltage or d.c. current.

```
clear
clc
T= 10;                    % PPMS reading temperatue
%Voltage range
e = 1.602e-19;
kb = 1.38e-23;
R_large = 381.6e3;        % current limiting resistance 341.6 kOhm
```

```
V = -6:0.3:6;            % Voltage sweep from -2V to 2V
T2 = T;              % Real temperature after calibration
dvdi=load([num2str(T) 'K_conductance.dat']);  % load the dvdi data

gain = 10000;            % amplifier gain
figure;
Svfit=[];
SIfit=[];
RCfit=[];
for v=V
    [SV, RC] = spec_robust_fit([num2str(T, '%.2f') 'K_' ...
        num2str(-v,'%.2f') 'V.dat'], 10000, 200000);
    Sv = SV/(2.518e-10) * 4 * kb * 300;
    Svfit = [Svfit, Sv];    % fitted voltage noise
    RCfit = [RCfit, RC];

end



L = length(dvdi(:,1));               % length of the dvdi file
[maxV,maxId] = max(dvdi(:,1));
[minV,minId] = min(dvdi(:,1));
newdvdi = dvdi(maxId:minId,:);      % select only one single sweep
I = newdvdi(:,1);                   % dc current of dvdi measurement
```

```
R = 1./newdvdi(:,5);                    % differential resistance
Vdc = newdvdi(:,2);                  % dc voltage of dvdi measurement

positionVector1 = [0.05, 0.15, 0.25, 0.75];
subplot('Position',positionVector1)
plot(Vdc*1e3,1e3./R,'.', 'MarkerSize', 10, ...
    'MarkerEdgeColor', 'black', 'MarkerFaceColor', 'k')
xlabel('V (mV)')
ylabel('G (mS)')
title('dI/dV')
xlim([-40 40]);
ylim([0 2]);
text(5,12, ['T = ', num2str(T),' K'],'fontsize',18);
set(gca,'fontsize',12)

%Rdc = newdvdi(:,6);                    % V/I resistance

SIfit = Svfit./(interp1(I,R,V/R_large)).^2;     % current noise
SIfit = 1.0 * SIfit;
R_inter = interp1(I,R,V/R_large);
SI_0 = 4*kb*T2/ (R_inter((1+end)/2));

Vsample = interp1(I,Vdc,V/R_large);  % dc voltage from interplation

x = [-20:0.1:20]*1e-6;
```

```
R_inter = interp1(I,R,V/R_large);  % differntial resistance



positionVector2 = [0.375, 0.15, 0.25, 0.75];
subplot('Position',positionVector2)

plot(Vsample*1e3,SIfit,'.', 'MarkerSize', 10, ...
    'MarkerEdgeColor', 'black', 'MarkerFaceColor', 'k') % plot V, SI
x=[-6:0.011:6];
hold on;

I = I - I((1+end)/2);
Vdc = Vdc - Vdc((1+end)/2);

xsample =interp1(I,Vdc,x/R_large);
y1 = 2*e*x/R_large.*coth(e*xsample/2/kb./T2);
range = find(x > -6 & x < 6);
P1 = polyfit(xsample(range), y1(range), 6);
y1(range) = polyval(P1, xsample(range));

plot(xsample*1e3,y1,'r--', 'LineWidth', 2);%hold on;

xlabel('Voltage (mV)')
```

```
ylabel('S_I␣(A^2/Hz)')
title('S_I␣-␣V')
legend({'Measurement','␣␣␣␣e*␣=␣e'},'FontSize',16,'Location','North')
xlim([-40 40]);
ylim([0 1e-23]);
set(gca,'XTick',(-40:10:40));
set(gca,'YTick',(0:0.2:1)*1e-23);
%ylim([0 8e-24]);
set(gca,'fontsize',12)

set(gcf, 'Units', 'Normalized', 'OuterPosition', [0, 0, 0.8, 0.6]);




positionVector3 = [0.7, 0.15, 0.25, 0.75];
subplot('Position',positionVector3)
SI_pred = interp1(xsample(2:end), y1(2:end), ...
    Vsample, 'spline', 'extrap');

plot(Vsample*1e3, SIfit./SI_pred,'.', 'MarkerSize', ...
    10, 'MarkerEdgeColor', 'black', 'MarkerFaceColor', 'k')
noise_ratio = SIfit./SI_pred;
v_ratio = [Vsample', noise_ratio'];
colNames = {'Voltage', 'Noise_ratio'};
v_ratio_tab = array2table(v_ratio, 'VariableNames', colNames);
```

```
xlim([-40, 40])
%ylim([0.8, 2])
set(gca,'XTick',(-40:10:40));
xlabel('Voltage␣(mV)');
ylabel('Noise␣Ratio');
title('Noise␣Ratio␣-␣V')
set(gca,'fontsize',12)
```

Appendix C

Ar ion etch process flow

The Ar ion etch was done at Prof. Ivan Božović's group at Brookhaven National Lab. The reactive ion miller was built together with an e-beam evaporator and mainly used for milling cuprate film samples with Ar plasma. Below are the steps for the ion milling processes.

Step 1: **Prepare the sample**

Glue the sample onto a sample carrier using "GE varnish";

Open the cooling water valve (not fully open to prevent leakage).

Step 2: **Vent the chamber**

Turn off the 2 ion gauges;

Turn off the 2 rough pump switches;

Turn the two pump controllers into vent mode 1 (speed down but not vent gas), wait a while and turn the small pump controller into vent mode 0 (vent gas at 40% setting speed). When both pumps speed go to 0, turn them into vent mode 2 (keep venting gas).

Release the screws for the main chamber and wait for the inside pressure to reach room pressure.

Step 3: **Load sample**

Open the sample shutter and move the stage to a higher position using the remote controller; Loose the 3 holding screws using 5/64 Allen ranch;

Insert the sample carrier plate and tighten the screws;

Move the stage to 1 inch (2.54 cm) position and close the sample shutter;

Close the chamber and start pumping. Turn both turbopumps into vent mode 1 (not venting gas); turn on the rough pump valve; When the inside pressure is less than 10 mBar, turn on both turbopump; Wait for ∼2 h for the pressure to reach 10^{-6} mBar range.

Step 4: **Ion milling**

Turn on gas channel 2 and 3 (both Ar gas). The flow is relative large (not specified) and the pressure if not in the ion vacuum gauges' measurement range;

Turn off the sample shutter;

Turn on the beam (beam current 50 mA, voltage 500 V), wait a while for it to stabilize, and then turn on the source to start milling for 30s;

Turn off the source for 2 mins to cool down the sample from overheating;

The above 2 steps is one etching cycle. The etching rate for LSCO is about 30 nm/12 cycles (6 min etching time in total). After finish all the cycles, turn off the beam and wait a while (at least 10 min) for the gun to cool down, then turn off the gas.

Step 5: **Take the sample**

Basically follow the sample steps with 2 to vent the chamber. Close the shutter, increase the height of the stage. Loose the clamp screws and take the sample carrier out.

Move the sample using a plastic tweezer, and soak into ethanol. Sonicate the sample at power 5 for 3 min and power 9 for 1 min. Transfer the sample into PG remove, soak for 3 min and sonicate at power 1 for 1 min.

Take the sample out while keep flushing it with ethanol. Blow dry the sample to finish.

Appendix D

Low frequency noise probe

In order to use the cross correlation noise measurement method, we constructed a dedicated low frequency (0 - 300 kHz) noise probe specially designed for the PPMS, see Figure D.1. We use vacuum adapter to adapt the NW-25 vacuum connector on PPMS to an ISO-200 vacuum connector in order to have larger area to host more connectors. The top ISO-200 flange was customized at the Rice machine shop, with holes left for Fischer connectors and SMA connectors, see Figure D.1**c**. A 3-feet long stainless steel rod from McMaster-Carr is used to connect the top flange to the bottom part. The bottom part consists a copper cold head and a PPMS puck. The PPMS puck acts as the thermal anchor and the copper is cooled through thermal coupling. As the PPMS wiring and ground have relatively large electrical noise, a thin sapphire piece is used to electrically isolate the PPMS puck and the copper head. The PPMS puck, sapphire and copper piece are assembled together by cryogenic compatible stycast epoxy.

The noise measurement setup is extremely sensitive to environmental electrical and magnetic signals. At the same time, it is desirable to minimize the wiring capacitance to ground. Here we use twisted wires plus some braided stainless steel sleeves to shielding the noise from the PPMS environment. By twisting the wire, the magnetic field's pickup can be canceled by forming many small loops in different directions. The metal sleeves can help shield the electrical field's effect. For some wires at the interconnect positions directly exposed to the environment, we use Aluminum foils

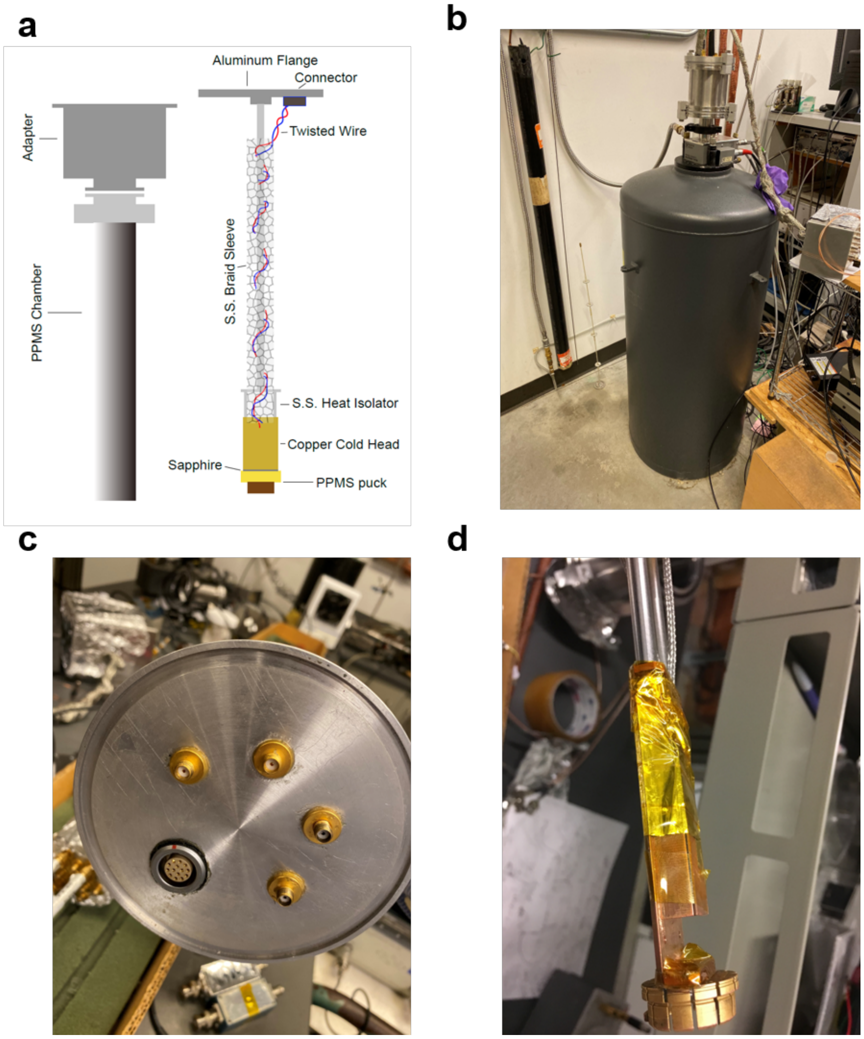

Figure D.1 : Low frequency noise measurement probe designed for PPMS. **a**, Schematic design for the insertion probe compatible with PPMS. **b**, Picture of noise measurement probe together with PPMS. **c**, Top view of the noise measurement probe. There is a 14-pin Fischer connector and 4 SMA connectors available on the top flange. **d**, Bottom part of the probe together with a sample box. Aluminum foil is used for shielding purposes.

to cover the wires and connectors to further improve the shielding, see Figure D.1**d**.

There are two main limitation factors of the noise measurement probe: 1. We do not have a cryogenic low noise amplifier that is directly mounted next to the sample. Such a cryogenic amplifier can effectively reduce the noise background level, minimize capacitive effects from the wiring and avoid standing waves along the transmission line. The tricky point for applying a cryogenic amplifier in our setup is that we want to measure the noise properties over a very broad temperature range. There is no currently available cryostat designed for our purpose with an extra thermal anchor at fixed low temperature to place the cryogenic amplifier. 2. The twisted wires still have relatively large effective capacitance. For our present wiring length ($\sim$3 ft), the effective capacitance is estimated to be around 200 pF. The capacitance effect is more obvious when the sample's resistance is large (above 10 kΩ), that the noise power spectra density decays very rapidly versus frequency at frequencies larger than tens of kHz due to the capacitance. To improve this, we may change to some thinner wires and leave more distance between the wires when twisting them.

The sample box for the noise measurement probe is home made from commercial available pure copper, see Figure D.2. A standard 16-pin chip carrier from Mouser Electronics is used to hold the chip sample and the sample can be connected to the carrier through Au wires. The legs of the carrier are soldered to pin connectors that compatible with connectors on the twisted pairs.

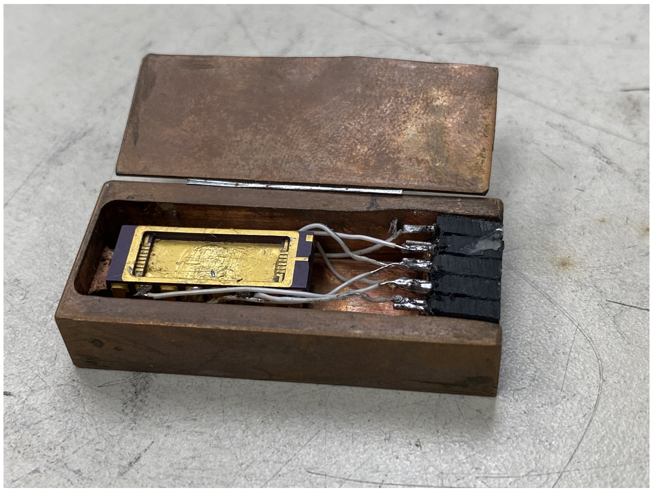

Figure D.2 : Home-made sample box for noise measurement.

Appendix E

Wirebond specifications

We use a K&S 4526 semi-automatic ultrasonic wedge bonder (see Figure E.1) to connect our device's Au pads to the chip carrier's Au pads. As the instrument has aged, some functions may not work well. Special attention is needed when using the wirebonder.

At the starting phase, when turning on the On/Off button, sometimes we need to hold the test button to skip the internal self-test. Otherwise the instrument may get stuck due to some mechanical issues. Before we put our sample holder onto the stage, the height of the stage should be adjusted to proper positions so that the sample holder will not crash the tip, and the tip is able to reach the sample. Before we do the bonding, we need to check all the parameters on the control panel, see Figure E.1**b-c**. Usually, we begin with tail setting around 3, search position around 9, power setting around 5, time setting around 5 and force setting around 2-3. We keep using small bonding forces to avoid penetrating the oxide layers on the chip.

The Au pads on the chip may be very challenging to bond if there is no adhesion layer or the adhesion layer is weak. In those cases, some special tricks might be useful.

1. Increase the bonding time. The bonding time means the time that the tip stays in contact with the Au pad during the bonding. With more bonding time, the

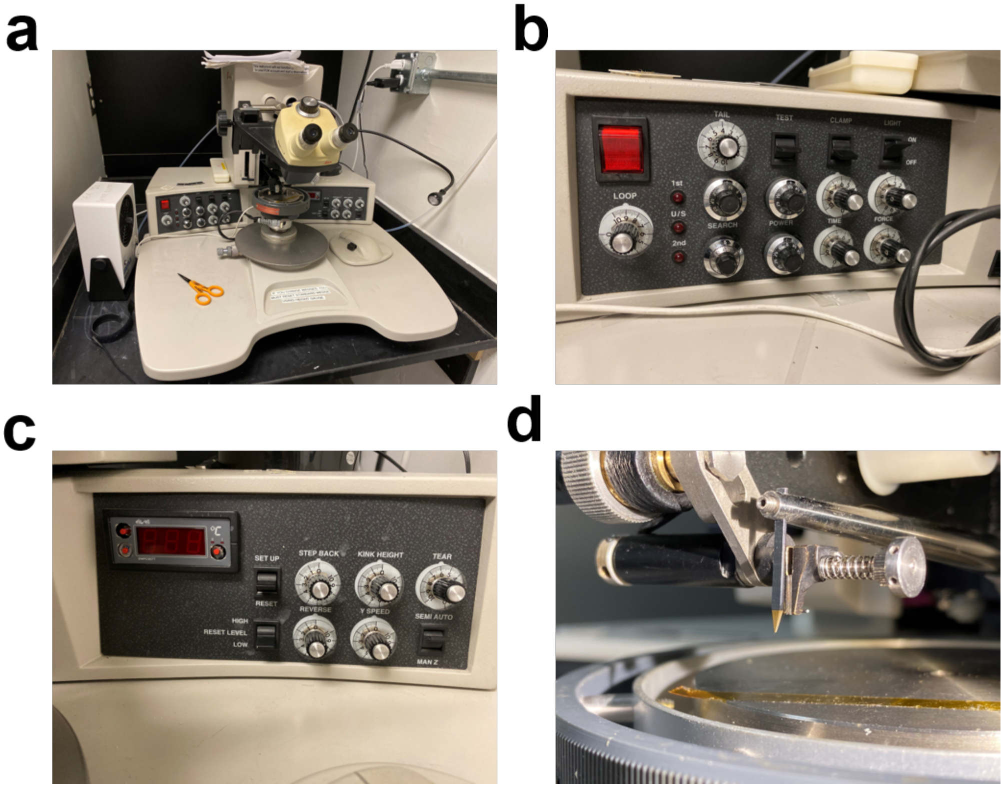

Figure E.1 : Photos of K&S 4526 semi-automatic ultrasonic wedge bonder. **a**, Overall instrument. An anti-static fan on the left side may be helpful for bonding electric sensitive devices. **b**, Control panel on the left side of the wirebonder, mainly used to control the bonding height, force and time. **c**, Control panel on the right side of the wirebonder, mainly used to control some adjustable parameters like the kink height and tearing force. **d**, Tip of the wirebonder. Au wire is feed through a hole on the tip-end with a short tail outside the tip.

ultrasonic power may help to Au wire to contact the Au pad better and improve the chance of making a solid bond. This effect is more obvious for the manually controlled wirebonder West Bond 7KE in the clean room.

2. Slide the tip during the bonding. This small trick was found by some previous lab colleagues. The basic idea is through sliding the tip during the bonding, we can increase the contact area and make better bonds.

3. Increase the temperature. This is suggested when bonding to some metals other than Au, such as aluminum or copper. At higher temperatures, the metal, especially Au might be softer and easier to connect to other metal surfaces.

4. Use some silver epoxy as an auxiliary for bonding. For some pads that are extremely fragile and almost impossible to make any direct bonding, we can apply a tiny amount of silver epoxy on top of the pads and bond to the silver epoxy instead. The epoxy we used is CW2400 Conductive epoxy. With a micromanipulator and a thin wire, we can precisely paste the epoxy to the pads.